USING STRAIN FIELD MINING TO REVEAL THE SPATIAL DISTRIBUTIONS OF TENSILE, FATIGUE, AND FRACTURE DAMAGE ACCUMULATION IN PAPER

A Dissertation
Presented to
The Academic Faculty

By

Yoon Joo Na

In Partial Fulfillment
of the Requirements for the Degree
Doctor of Philosophy in the
School of Materials Science and Engineering

Georgia Institute of Technology

August 2019

USING STRAIN FIELD MINING TO REVEAL THE SPATIAL DISTRIBUTIONS OF TENSILE, FATIGUE, AND FRACTURE DAMAGE ACCUMULATION IN PAPER

Approved by:

Dr. Christopher Muhlstein, Advisor
School of Materials Science and Engineering
Georgia Institute of Technology

Dr. Arun Gokhale
School of Materials Science and Engineering
Georgia Institute of Technology

Dr. Surya Kalidindi
School of Mechanical Engineering
Georgia Institute of Technology

Dr. Meisha Shofner
School of Materials Science and Engineering
Georgia Institute of Technology

Dr. Preet Singh
School of Materials Science and Engineering
Georgia Institute of Technology

Date Approved: July 18, 2019

Dedicated to my parents.

ACKNOWLEDGEMENTS

Many individuals helped me grow and accomplish during the last five years at Georgia Tech...

First, I want to thank my research advisor, Chris Muhlstein, for his guidance, input, and kind support. I am also grateful to former and current group members, Wade Lanning, Saad Javaid, Sarah Paluskiewicz, James Collins, and Vincent Wu, for their companionship and support in the lab and office. I want to give special thanks to Wade, who always went out of his way to provide suggestions and help especially during my first years.

I feel fortunate to have met my best friends at Georgia Tech: Yeon Hye Kwon, Sujin Lee, and Su-Yeon Choi. Without their presence, my life at Tech would not have been the same. I want to express many thanks to them for filling the last five years with so many precious memories and their positive energy. I also would like to thank a group of fellow MSE students who joined the program the same year: Kasey Hanson, Kevin Chan, and Brandon Piercy. They were great friends in and out of school, studying together for exams and taking me to numerous fun activities on many weekends. Furthermore, I want to thank my best friends from high school, Jung Min Kim and Suna Jo, for always being there for me and supporting me over countless texts and calls from miles and miles away.

Most importantly, I would like to thank my family. My brother, for always thinking too greatly of me and filling up my missing presence in the family. Podo, my puppy, for giving me so much joy in my life. My parents, for providing unconditional love and support throughout my long academic journey in the states. Without them, I would not be where I am right now.

This work was sponsored by the Renewable Bioproducts Institute at the Georgia Institute of Technology. The sponsor had no direct role in the design, collection, analysis, and interpretation of data.

TABLE OF CONTENTS

LIST OF TABLES

LIST OF FIGURES

SUMMARY

The most common nonwoven fiber composite material, paper, has a porous, heterogeneous fiber network structure and complicated mechanical properties. The mechanical properties of machine made papers are orthotropic and are sensitive to loading rate, moisture content, and temperature. Thus, defining the constitutive relationship of paper has remained as a challenge due to the stochastic nature of the structure and countless variables that affect the mechanics of paper. Moreover, the technology to non-destructively characterize the three-dimensional network topography at the fiber length scale is not readily available. This presents a critical barrier to establishing the structure-property relationships of paper. Here, I approached the problem with a fundamentally different strategy and used the structure of the strain fields as a proxy for the network topography. The strain fields of paper from tensile, fatigue, tearing experiments revealed new information about each damage mechanisms. During the tensile deformation, the interplay between the axial and the transverse motions in the fiber network resulted in specimen-orientation-dependent (MD and CD) parameters such as Poisson's ratio, hot spot length scales, and the degree of nonaffinity, D. These metrics were direct manifestation of the anisotropic fiber network in paper. Next, I used strain field mining to track the fatigue crack lengths and quantified crack growth rates during cyclic and constant loading conditions. The fracture profiles and the crack growth rates revealed that there was a unique fatigue damage mechanism in paper which induced the fiber fracture rather than the fiber pull-out. Moreover, I found that the pre-applied creep damage in paper can significantly reduce the fatigue crack growth rate and extend paper's high cycle fatigue life. Lastly, from the strain fields of tearing specimens, I was able to characterize paper's crack tip process zone whose shape depended on the orientation of the fiber network. Although paper has a completely different structure and failure mechanism from metals, I found that tearing of paper also followed a steady-state process, which was previously observed in thin sheet aluminum foils.

CHAPTER 1
INTRODUCTION

1.1 Background and Motivation

Paper is one of the oldest engineered composite materials, and its importance in our society has evolved over millennia. In recent decades the need for paper in printed media has been eclipsed by its dominance in product packaging and shipping box applications. This dominance is, in part, because paper is manufactured from a renewable resource (cellulose-based wood fibers), can be readily recycled, and is biodegradable and surprisingly strong [1, 2]. Moreover, one of paper industry's most recent technology objectives was enabling new products to meet the demands for more sustainable, energy efficient, recycling, and economic products [3]. Engineering the new products requires more in depth research on understanding of paper's processing-structure-property relationship.

Paper is a nonwoven fiber composite material where cellulose fibers are held together by inter-fiber hydrogen bonds [2, 4, 5]. During the manufacturing processes of commercial papers, the fibers are placed on a moving web, water is removed from the fiber slurry, and the fibers bond to each other via hydrogen bonding [1]. A heterogeneous network of cellulose fibers are formed where the majority of the fibers are aligned with the machine direction (MD), the direction that the paper web travels. This preferential fiber alignment in MD results not only structural anisotropy but also mechanical orthotropy [6–8]. The elastic modulus and the yield and ultimate strengths are typically 2–3 folds larger in the machine direction than the cross machine direction (CD) of the paper. Paper has stress-strain (constitutive) behavior that is qualitatively similar to structural metals— linear, elastic (i.e., reversible) deformation is followed by permanent (plastic), nonlinear deformation that ends with catastrophic failure (Fig. 1.1).

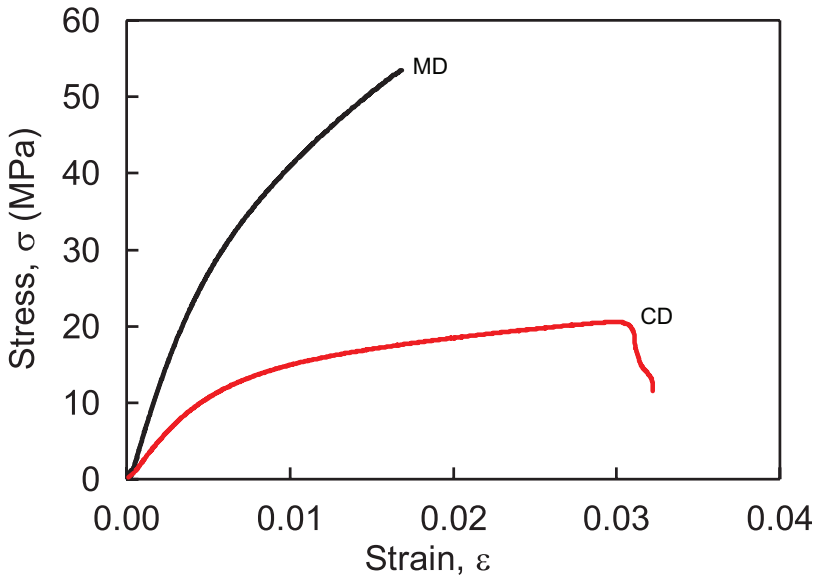

Figure 1.1: Typical stress-strain curve of machine made papers in MD and CD orientations

Despite the familiar macroscopic tensile behavior, paper's mechanical properties are very complex; The hydrogen-bonded, cellulosic fiber network of paper is porous and the fibers are heterogeneously distributed in the sheet [9, 10]. As a result, the mechanical properties of machine made papers are anisotropic and sensitive to moisture content, temperature, and loading rate [9]. Moreover, the constitutive relationship of paper is governed by not only microstructural variables such as fiber length, fiber modulus, fiber density, bond strength, but also macroscopic, architectural network, and processing variables such as bond density, fiber flocculation, and fiber orientation [1, 6, 11]. Both the properties of the fibers (e.g., geometry, modulus, density, and orientation) and their arrangement in the network contribute to the physical properties of paper [12–16]. Therefore, establishing the structure–property relationships for paper still remains as a challenge due to its complicated structure and stochastic nature [2]. It is extremely challenging to incorporate all the conceivable variables in a constitutive model and relate the structural properties to the macroscopic tensile response. Existing constitutive models are often limited to several structural parameters to describe the deformation behavior of paper. Different models are derived at different levels of scales in paper, from a hydrogen bond to a continuum fiber

network [6, 7, 13, 17, 18].

Understanding the structure of the fibrous network is, thus, important for linking macroscale properties such as strength, stiffness, and permeability with the structure. And only when the structure is fully understood, we can verify many network models [11, 12, 18–20] that describe the constitutive relationship of paper. Because spatial distribution of fibers and other constituents strongly influence many physical properties (e.g., mechanical, transport, optical) of paper, knowing the relationship between structure and properties is important to be able to predict the properties of the material [1, 2, 9, 10]. Due to the growing demands for better performance (mechanically robust) paper for packaging and shipping applications, there has been a widespread interest to fully characterize the structure of paper at the length scale of the fibers (micrometer scale). Therefore, visual and quantitative descriptions of the 3D structure of paper has long been a goal for the paper industry [21, 22]. Various methods such as scanning electron microscopy (SEM), microtomy [23–25], resin block grinding [26, 27], confocal laser scanning microscopy (CLSM) [28–30], X-ray computed tomography [22, 31, 32], have been developed to characterize 2D cross sections of paper and 3D reconstructed structure of the fiber network.

Despite the progress in various techniques that can characterize the structure of paper at the fiber level, there still remains challenges and limitations. Microtomy has been used to evaluate paper cross sections embedded in epoxy resin and to extract relevant parameters for the mechanical properties such as number of contacts per fiber, contact area and curvature of fibers [23–25]. However, the sliced sections of paper are not an accurate representation because the sample structure can get distorted during mechanical sectioning [29]. Williams et al. [26, 33] developed an alternative method where the embedded block surface rather than thin sliced sections are imaged after manually grinding and polishing the resin block surface and exposing the top layer of the embedded paper by resin removal process. This method allowed minimal disturbance of the structure and reliable exposure of fine microstructure and its examination and elevated magnification. This grinding–resin

removal–imaging process can be repeated and get the same result as the serial microtome sectioning. However, 3D reconstruction of the paper structure using the sectional images requires extensive steps of post-processing analysis and is very time consuming, yet only small volume of paper can be constructed [23–25]. A nondestructive methods such as CLSM and X-ray CT are more recently developed. CLSM technique is dying the paper sample with fluorescent dyes that reacts with lignin part of the cellulose fibers and fluorescence imaging under the confocal microscope. It has an optical sectioning capabilities and has been used as a nondestructive way to visualize the 3D structure of paper; however, its limitations are the low contrast between fibers and voids and the rapid signal intensity attenuation with the sample depth, which limits the depth below the surface that can be successfully imaged to about 50 μm [28–30, 34]. The X-ray computed tomography technique has now been received as the most promising way of imaging the 3D structure of paper at the spatial resolution of fibers. Many studies have shown that X-ray microtomography can successfully depict the 3D structure of paper at relatively high resolution [21, 22, 28, 31, 32, 35]. The resolution and the quality of the reconstruct images, however, vary by the voxel resolution, volume sizes, and imaging conditions that change according to the type of X-ray sources used. Therefore, the high resolution x-ray microtomography which can only be achieved with advanced synchroton sources is not readily available and extremely costly and time consuming.

The fundamental challenge of characterizing the 3D structure of paper comes from the fact that paper is both very long and extremely thin. This means that we must be able to characterize a relatively large area and volume of paper at the micrometer resolution to see the whole heterogeneous network and identify individual fibers [24]. While individual and small groups of fibers can be characterized at small length scales, the larger scales that capture the whole network are harder to be characterized. Many fracture mechanics related problems of paper arise when the paper is in the web which means that large area of the structure needs to be analyzed. Another challenge of characterization of paper is that

wood fibers are predominantly carbon. The atomic number of carbon is very low (Z=12), so it is difficult to use energetic particles and/or waves to distinguish between open (free) space in the fibers and the fibers. Similarly, it is difficult to distinguish between the fibers and the interfiber regions- regardless of the tomographic approach that is used. While the characterization strategies will continue to improve, with the current techniques and limitations mentioned above, characterizing a small volume of the material is not helpful for identifying the structure–property relationship of paper. Thus, we need a scheme to identify which parts of the fiber network are important to the deformation, degradation, and failure of the material.

A more indirect yet more approachable alternative way to map the structure-mechanical property relationship is using the strain fields obtained with Digital Image Correlation (DIC). In fact, non-contact, optical strain measurements have been used for over 40 years to study the relationships between fiber network structure and deformation of paper. Early work by Lyne and Hazell [37] used the fringes in interference holograms of tensile specimens to demonstrate that nonuniform strain fields just before fracture were more pronounced in papers with flocs (fiber agglomerates). DIC techniques pioneered by Sutton et al. offered improved spatial resolution of optical strain fields and its first application to paper; Chao [38] and Sutton [39] examined deformation fields of paper and concluded that the method could be used to interrogate the strain field on various length scales by selecting appropriate analysis regions. Similarly, Ting [40] used confocal laser scanning microscope imaging to study individual fiber and network movement of notched handsheet specimens at limited field of view. Wong [36] correlated the mesostructure (millimeter length scale) to tensile strain and stress field of unbleached kraft handsheets few seconds before the fracture (Fig.1.2). Wong et al. found that the local tensile strain is inversely proportional to the local grammage, a way of measuring weight per unit area of paper materials, and that the fracture initiated from one of the (many) high strain zones. Considine [41], using DIC, showed that the variation in strain increased as the global tensile stress

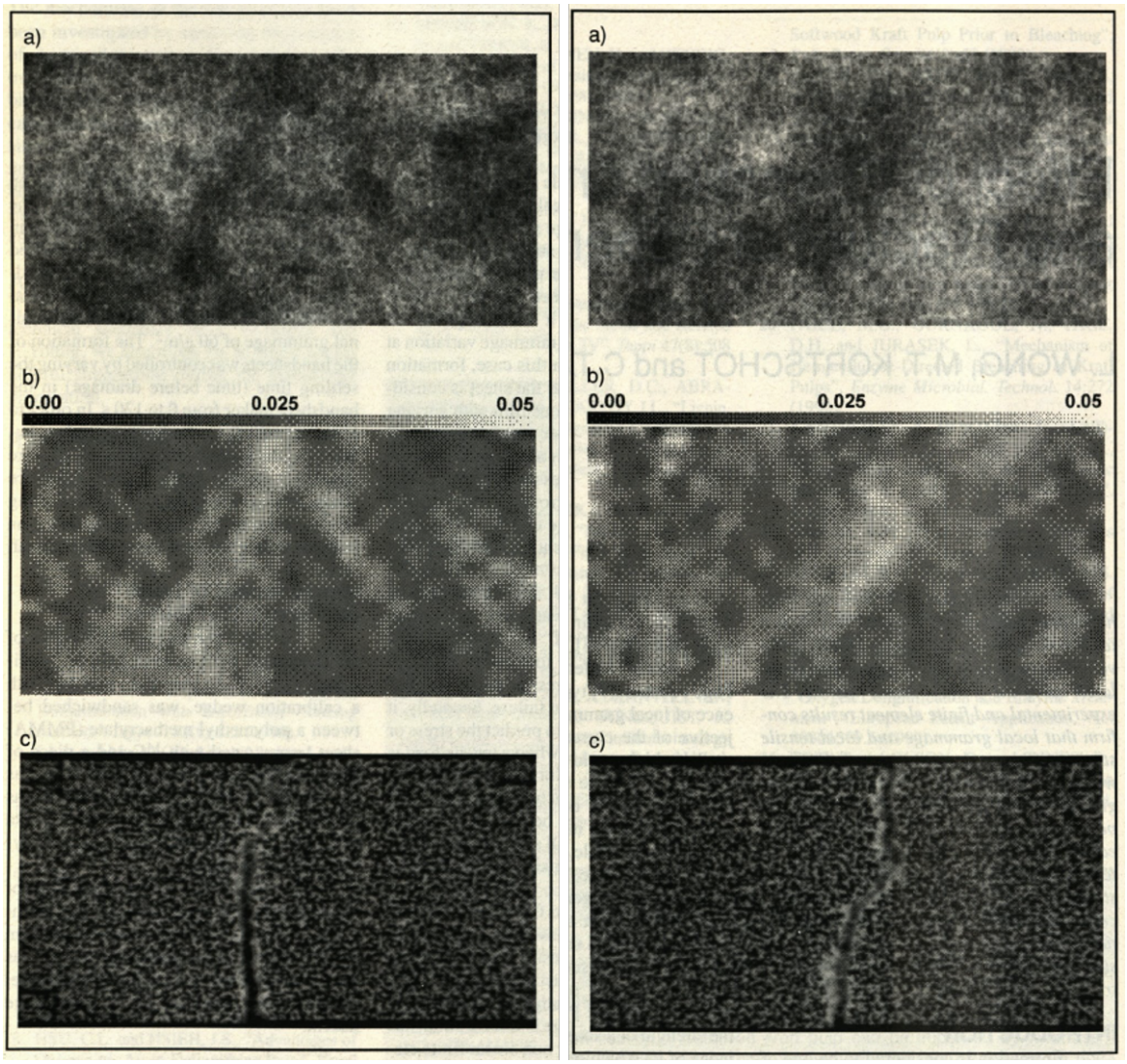

Figure 1.2: Comparisons of (a)grammage map, (b)strain map, (c)fracture line of 20 mm × 50 mm handsheet specimen near fracture. [36]

increased (Fig.1.3). Borodulina [42] observed millimeter-scale damage localization in the random fiber networks of handsheets and concluded that the local strains are precursors of bond failures using a simulated 3D network model (Fig.1.4). These DIC studies showed the spatial heterogeneity in tensile straining of paper and potential correlations to the local fiber densities. However, the light transmission images used to identify fiber density are not an accurate representation of local fiber density due to light reflection and scattering [9, 43], and identifying which of the many high strain regions would initiate fracture still remains to be solved. Moreover, these studies were done on isotropic handsheets instead of the anisotropic, machine made papers relevant to industrial applications.

In this work, instead of directly characterizing the fiber network structure, high fidelity axial and transverse strain fields analyzed with various strain field mining approaches will be used to reveal new insights about deformation, fracture, and subcritical crack growth mechanisms during tensile, fatigue, and fracture processes of machine-made papers. It is impractical and difficult to blindly characterize a large volume of paper structure, so strain field mining can be used to identify strain field microstructures that are relevant to the mechanical behavior and deformation process. Once strain field microstructures are distinguished, the length scales that control damage accumulation can also be found. The important strain microstructure and mesostructure of the strain fields identified in this dissertation are strain hot spots, crack extent, and crack tip process zones of machine-made papers in two orthogonal specimen orientations. The orientation-dependent characteristic shapes, sizes, and length scales of these strain structures obtained with the strain field mining will contribute to the fundamental understanding of how paper and packaging products deform and how to extend the methodology for product development and process control.

1.2 Structure of Dissertation

The main goal of this dissertation was revealing the relevant features in the strain fields and correlating them to deformation mechanism. First, in chapter 3, I will detail existing

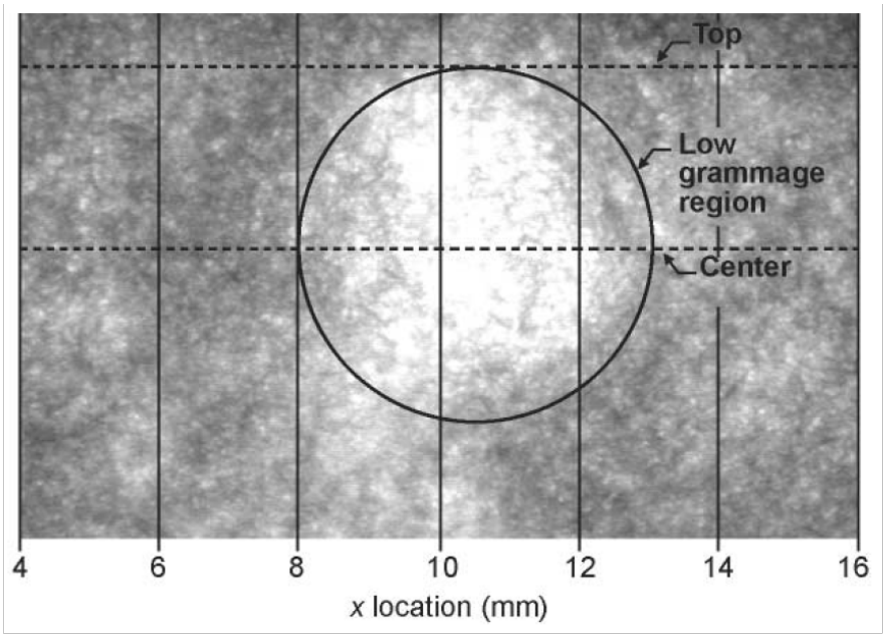

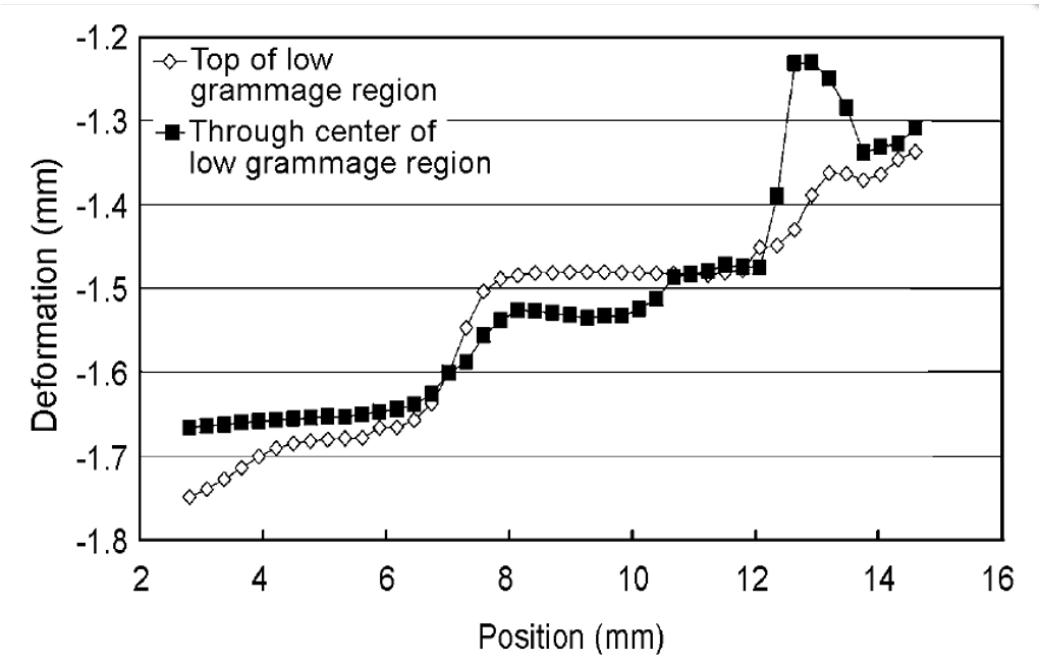

Figure 1.3: Grey-scale image of a low-grammage region of a 100 mm $\times$ 15 mm tensile handsheet specimen. Two lines of deformation across length of specimen near failure. [41]

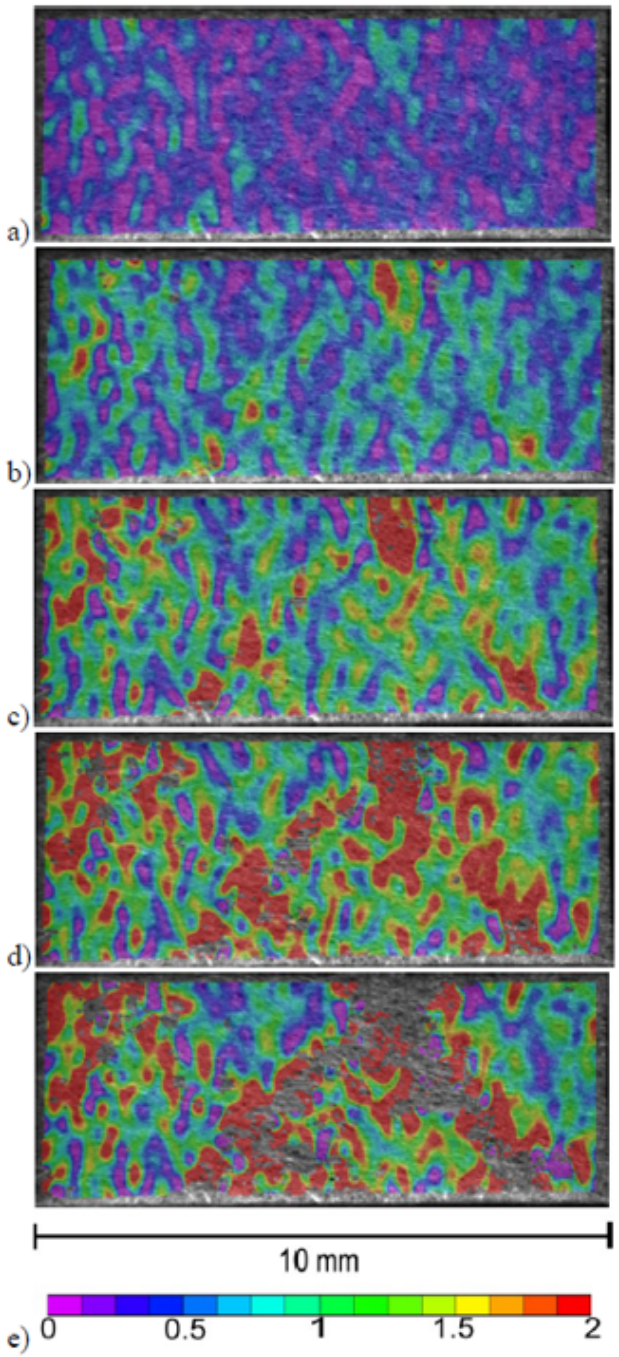

Figure 1.4: Strain maps of $10\,\text{mm} \times 4\,\text{mm}$, $27\,\text{g}/\text{m}^2$ handsheet specimen. [42]

structural characterization methods for paper structure and the challenges and limitations associated with each technique. Then, in chapters 4, 5, 6, I will present how strain field mining was used to understand tensile deformation, fatigue damage accumulation, and subcritical crack growth mechanisms in the heterogeneous fiber network of paper.

In chapter 2, I will detail materials, experimental setup, and analysis methods used in this study. The chapter will start with details about materials and specimen preparation, including specimen cutting, speckling, and conditioning. Then, mechanical testing set up and testing parameters used in tensile, fatigue, creep, and tearing experiments will be detailed. Following this section, I will explain the set ups related to DIC such as imaging settings and feature tracking and correlation methods. Next, different analysis methodologies, both numerical and strain field mining techniques will be discussed. Finally, structure characterization techniques including imaging tools and cross sectioning techniques will be detailed.

In chapter 3, the results of different structural characterization techniques used to image paper samples used in this study will be presented. I will start the chapter with the formation analysis of paper using the transmission light optical images and move onto discussing more direct characterization methods such as microtome sectioning, grinding, CLSM, and X-ray tomography. Each section will show the limitations of destructive or nondestructive methods and difficulties of reconstructing the three dimensional structure of paper sample in large volume at high resolution.

In chapter 4, I will focus on the nonaffine deformation characteristics of paper during uniaxial tensile loading. This chapter will begin by going over the macroscopic tensile properties of copy paper in two orthogonal orientations and the Weibull analysis on the strength distribution of paper. Then, representative strain fields as well as evolving Poisson's ratio will be presented. The hot spots of the strain maps will be analyzed using the lineal path correlation method. In the later part of the chapter, axial and transverse displacement maps and the nonaffine characteristics of them will be discussed with the degree

of nonaffine deformation metric, D.

In chapter 5, I will discuss paper's cyclic deformation mechanism that was different from tensile or creep. Here, I used a strain field mining technique to track and measure the extent of fatigue damage (crack) and the crack growth rates of specimens subjected to different loading conditions (cyclic and constant loading). I will also present fracture profiles of tearing, fatigue, and creep specimens and show that there is a distinct cyclic damage accumulation mechanism in paper.

In chapter 6, I will detail a study on the tearing of single edge notched tensile (SENT) specimens in two orientations. The relationship between the applied nominal stresses and normalized crack lengths as well as experimentally measured crack tip strain fields will be presented. I will first qualitatively discuss how strain maps changed over the course of a tearing experiment. Then, I will show that a quantitative analysis on the zone of active plasticity prove that tearing in paper is a steady-state process.

In chapter 7, I will first discuss the summary of the overall goal and motivations of this study. Then, I will wrap up the dissertation by summarizing the results and conclusions from key experiments. I will end the chapter with a recommendation for future studies.

CHAPTER 2
MATERIALS AND METHODS

This chapter will detail materials and testing and analysis methods used to evaluate tensile, fatigue, fracture, and structural characteristics of paper. The first part of the chapter will describe what materials were used and how specimens were prepared. Then, the set up for mechanical tests and the parameters used for tensile, fatigue, creep, and fracture experiments will be detailed. The following section will describe imaging conditions and feature tracking and correlation methods for Digital Image Correlation (DIC) used for most parts of this study. Next, different quantitative analysis methods and strain field mining techniques used to interpret experimental and strain data will be explained. The chapter will conclude with characterization tools and techniques used to characterize the structure of paper.

2.1 Materials and Specimen Preparation

Three types of machine made papers were used in this study: copy paper, filter paper, and linerboard. Copy paper (135855-WH) with grammage of $75\,\mathrm{g/m^2}$ was purchased from Staples (Framingham, MA). It was found that mean length and width of the fibers that compose the paper were 0.704 mm and 21.6 µm, according to the fiber quality analyzer (FQA) analysis per TAPPI standard T401[44] (see Appendix A). A roll of 15 cm wide and 100 m long filter paper (Whatman 3001-681 cellulose chromatography paper, grade 1) was purchased from Data Support Company (Panorama City, CA). The manufacturer specified thickness and grammage were 0.18 mm and $87\,\mathrm{g/m^2}$. A series of proprietary, commercial linerboards were also evaluated. All of the experiments in this dissertation were conducted on the copy paper unless stated otherwise. For comparison, some experiments were repeated on the linerboard and the filter paper since raw materials and specimen thicknesses

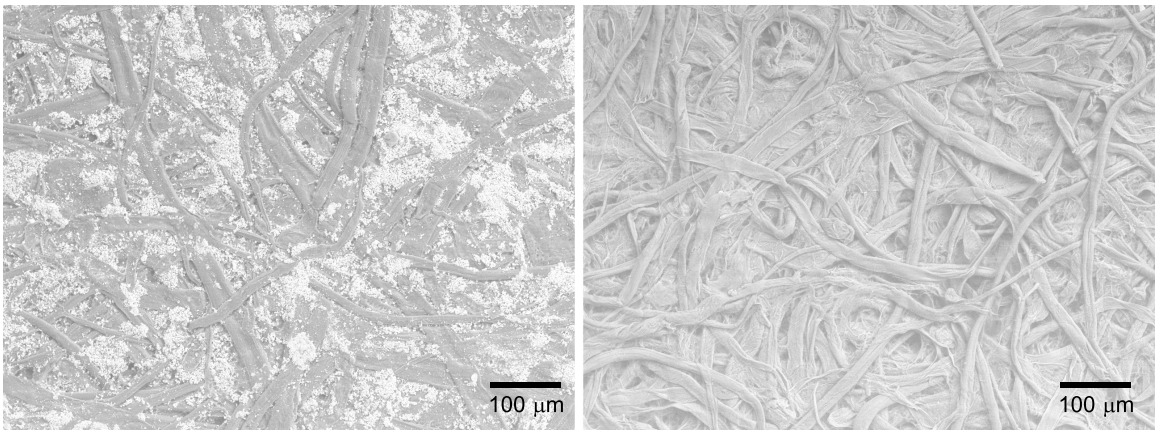

Figure 2.1: SEM images of surface of copy paper (left) and filter paper (right) show that copy paper contains a lot of inorganic fillers (bright spots) and filter paper is made of cellulose fibers only.

of three types of paper were different. For example, the copy paper contains a lot of inorganic fillers (e.g. TiO_2, $CaCO_3$) where the filter paper is only composed of cellulose (Fig. 2.1).

Specimens were cut into 12.5 mm wide (w) and 88 mm long (l) strips in two orthogonal orientations (machine and cross-machine directions) using the Sizzix Eclipse 2 paper cutting machine (Sizzix, Lake Forest, CA). The actual gauge length of a specimen was 50 mm because each grip end was 19 mm long. The specimen dimensions were modified from TAPPI standard, T494 [45], to gain a full field view of the gauge section when capturing images for DIC. For notched specimens, a pre-cut notch was additionally cut on one side of the specimen during the specimen cutting process. For fatigue and creep experiments (results in Chapter 5), single edge notched CD specimens with a crack size of 27 % of the width ($a = 0.27w$) were used. For fracture experiments (results in Chapter 6), single edge notched MD and CD specimens with crack sizes of 20, 25, and 30 % of the sample width ($a = 0.2, 0.25, 0.3w$) were used.

Since paper is not a material with distinguishable surface features, artificial features were created on the surface of the specimens for DIC feature tracking purpose. For the earlier work in this dissertation (results in Chapter 4), a grid array of 0.1 mm dots 1 mm

(40 pixels) apart from each other were printed using a Xerox Phaser 5550 laser printer (Xerox, Norwalk, CT) on the copy paper sheets. For later experiments in this study (results in Chapters 5 and 6), instead of printing small dotted features, a random speckle pattern was airbrush painted (Iwata, Portland, Oregon) on the specimens. Note that these artificial features did not have a significant effect on the mechanical performance of the paper specimens used in the study. Specimens with and without the features resulted indistinguishable stress-strain curves under the same uniaxial tensile testing condition.

As specified by TAPPI standard T402 [46], all copy paper specimens after specimen preparation (cutting and speckle patterning) were preconditioned at $23 \pm 0.3\,^{\circ}\mathrm{C}$ and $35 \pm 3\,\%$ RH for an hour and conditioned at $23 \pm 0.3\,^{\circ}\mathrm{C}$ and $50 \pm 3\,\%$ RH for at least four hours prior to testing in a SH-241 (ESPEC Corp., Osaka, Japan) bench top temperature and humidity chamber. The preconditioning and conditioning times to reach equilibrium with the atmosphere for other paper types are longer as specified in the TAPPI standard T402.

2.2 Mechanical Testing

All mechanical tests were conducted with a 100 N ($\pm 0.5\,\%$) Instron 2530-427 static load cell and the Instron 5848 (Instron, Norwood, MA) load frame equipped with a magnetic linear encoder with a 20 nm resolution (Heidenhain, Shaumburg, IL) placed on a bench top vibration isolated platform (BM-4, Minus K Technology, Inglewood, CA). This load frame, a dedicated low force, small displacement system, was routinely used to conduct closed loop, force and displacement controlled tests on small, flexible specimens in the research group. The specimens were gripped with the Instron 2716-16 serrated mini wedge grips. The load frame, grips, and specimens were precisely aligned every time experiments were conducted. A small preload (<3 N) was applied to remove any slack in the specimen and to obtain focused images for the experiments. LabView 7.1 (National Instruments, Austin, TX) software was used to control the actuator and to collect the tensile data from the load cell.

For chapter 4, tensile tests were conducted in displacement control mode at a rate of 3 mm/min. 60 specimens were tested for each of the two principal orientations, machine direction (MD) and cross-machine direction (CD). All tensile tests were conducted in a controlled atmosphere of 23 °C and 50 % RH. Tensile properties obtained from the tensile tests will be detailed in section 2.4.1. For chapter 5, fatigue tests in tension were conducted in load control mode at 1 Hz with a minimum to maximum load ratio ($\sigma_{min}/\sigma_{max}$) of 0.1 where σ_{min} is the minimum stress and σ_{max} is the maximum stress during each sinusoidal cycle. Unnotched CD specimens were loaded at various maximum stresses, ranging from 10.8 MPa to 18.72 MPa until fracture. Notched CD specimens ($a/w = 0.27$) were also loaded at various maximum stresses ($\sigma_{max} = \frac{P_{max}}{wB}$), ranging from 5.6 MPa to 10.8 MPa. These chosen maximum stresses fall between specimens' yield and tensile strengths. Creep tests were also conducted in load control at a constant stress of 6.8 MPa. For chapter 6, fracture tests were conducted in displacement control mode. For results in section 6.2.1, 12 MD specimens were loaded at 0.1 mm/min and 12 CD specimens were loaded at 0.3 mm/min. For results shown in section 6.2.2, three MD and three CD specimens ($a/w = 0.3$) were loaded at 0.1 mm/min.

2.3 Digital Image Correlation

Digital Image Correlation (DIC) is a non-contact strain measurement technique that captures motion, shape, and deformation of solid objects [47]. This technique relies on tracking the positions of surface features (speckle pattern) from a series of images taken during motion or deformation of specimens and calculating displacements and strains from the tracked information. For this work, images of the specimens during mechanical tests were captured, where the camera triggering times were synchronized with the Instron load frame. Therefore, the images of the specimens were captured from the start to the end of the experiments, and each image was time-stamped so that stress values at the time of image capture were available.

2.3.1 Imaging System

For the early experiments in this study (results shown in Chapter 4), a 3.1 megapixel PL-B776 digital camera (Pixelink, Ottawa, Canada) with Toyo optics TV 12.5-75 mm F1.8 zoom lens (Toyo Optical Glass LTD, Hong Kong, China) was used to image the gauge sections of the specimens during the tensile tests. A 33120A function generator (Agilent, USA) was used to trigger the camera and to collect images at a rate of 2 Hz that were synchronized with the crosshead displacement and load cell data.

For later experiments (Chapters 5 and 6), the imaging setup was upgraded so that images with higher pixel count can be used for DIC. A 24 megapixel (6000 x 4000) Nikon D3300 DSLR camera with a Nikon macro lens was used to capture images of specimens before and during experiments. An Arduino Mega microcontroller with custom firmware was used to trigger the camera and to collect images at a rate of 1 Hz that were synchronized with the crosshead displacement and load cell data. For fatigue tests, the camera was triggered every 1 minute (60 cycles), and at each triggering point a total of 9 phase lagged images were taken every 1.125 seconds to reconstruct the sine wave cycle. For every experiment, the camera was aligned such that it was parallel to the plane of the specimen being imaged, and the specimen was centered in the field of view.

For specimen illumination during experiments, a Dolan-Jenner Fiber-Lite light source with a Dolan-Jenner FLD light diffuser box was used to uniformly illuminate specimens from the front, and it was positioned between the camera and the specimen. The DSLR camera settings were set to ISO of 100, aperture of F3.3, and shutter speed of $1/80$ s.

2.3.2 Feature Tracking and Correlation

For results in chapters 4 and 5, the spatial distribution of deformation and strains were evaluated by an in-house DIC program developed by Collins et al. [48], which is based on conventional correlation algorithms [49]. Each tracked feature was about 12 pixels long and wide and was composed of pixels that varied in grayscale levels so that each feature

is distinguishable from others. The grids were 16 pixels apart, and the subset size was 16 pixels by 16 pixels. For the strain and deformation maps, a random subset of 25 specimens each in MD and CD orientations were analyzed, and representative results among them are presented. For results in chapter 6, a regular grid spacing of 32 pixels by 32 pixels was generated on the first image and then these grid points were tracked through the image sequence using a Python (Anaconda 2.7) code, developed by Wade Lanning, using the OpenCV sparse optical flow feature tracking algorithm calcOpticalFlowPyrLK. For both tracking methods, strain maps based on the motion of tracked positions were plotted using a linearly interpolation Voronoi tesselation scheme, which eliminated numerical artifacts found in some cubic spline and other nonlinear interpolation methods.

The magnitude and noise levels in the tracked displacement and strain values were experimentally determined using a series of rigid body motion tests, and have also been verified with synthetic digital images. Before each experiment, a stationary sample in the grips was imaged where the camera mounted on a motor controlled precision three axis stage (ET-50-12, Newmark Systems, CA) was moved. The distance that the stage and camera moved was recorded by an encoder (optical encoder resolution better than 1 μm). Then, features on these set of rigid body motion images were tracked using DIC, and displacement and strain values were calculated. As shown in Table 2.1, the measured displacement error was up to approximately 0.1 pixel, which corresponded to a strain noise floor of 10^{-6}. The color bars used to represent the strains were then selected to insure that apparent differences in color were associated with significant differences in strain. The line width resolution of the images was determined with a 1951 USAF microscope resolution target and was better than 20 μm.

Table 2.1: Actual and tracked horizontal (x) and vertical (y) movements during the rigid body motion test. Displacement error is the difference between the actual and tracked movements. The full field strains (ε_{xx} and ε_{yy}) were obtained from the tracked displacements using DIC.

Actual Movement, (x, y) (pixel)	Tracked Movement, (x^*, y^*) (pixel)	Displacement Error, $(x^* - x, y^* - y)$ (pixel)	Calculated Strain, $(\varepsilon_{xx}, \varepsilon_{yy})$
(0.306, 0)	(0.384, 0.048)	(0.078, 0.048)	$(1.3 \times 10^{-5}, 4.3 \times 10^{-6})$
(1.258, 0)	(1.43, 0.019)	(0.172, 0.019)	$(2.4 \times 10^{-6}, 2.5 \times 10^{-6})$
(1.96, 0)	(1.796, 0.031)	(0.164, 0.031)	$(2.6 \times 10^{-5}, 6.5 \times 10^{-6})$
(2.47, 0)	(2.857, 0.1)	(0.387, 0.1)	$(1.5 \times 10^{-5}, 5.5 \times 10^{-5})$
(0, 3.47)	(0.06, 3.553)	(0.06, 0.083)	$(2.6 \times 10^{-5}, 2.0 \times 10^{-5})$

2.4 Analysis Methods

2.4.1 Tensile Properties

For tensile experiments, 60 specimens were tested for each of the two principal orientations, MD and CD. For each specimen, elastic modulus, yield strength, yield strain, tensile stress, tensile strain, and tensile energy absorption (TEA) were calculated as specified in T494 [45]. It is a common practice to disregard a thickness value and report stress in terms of force per unit width [1] because paper is easily compressible and it is difficult to measure the actual thickness. In this study, a conventional stress unit, force per unit area, was used with the nominal thickness of 0.1 mm, which was confirmed using scanning electron microscopy images (Fig. 2.2).

Elastic modulus was calculated from the linear portion of a stress strain curve consistent with the methods detailed in ASTM E1111 [51]. The linear elastic part of the curve was determined by fitting a linear regression line from the first data point to the data point where the coefficient of determination, R^2, was 0.999. The last data point of the linear portion was recorded as the yield point (yield stress and strain reported in Table 4.1). The tensile energy absorption, the energy per unit area of the specimen, was defined as the area under load-displacement curve up to the failure point and was calculated from the experimental

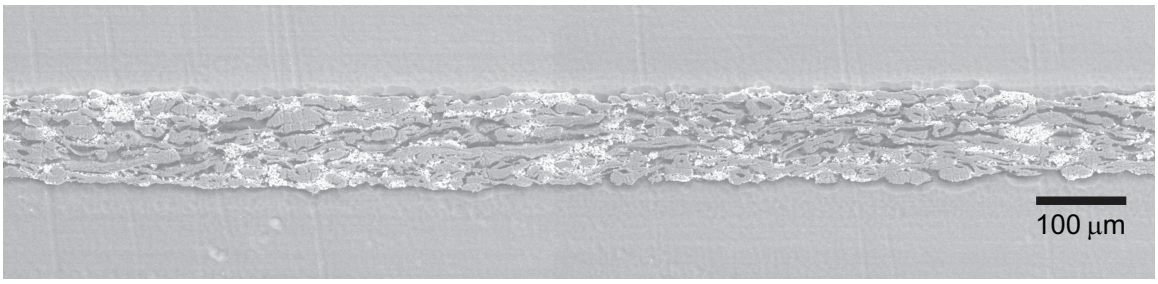

Figure 2.2: A cross sectional image of copy paper was taken using SEM. In this figure, a copy paper sample was embedded in Spurr's resin [50] where the direction going in and out of the page is MD. Bright lumps of particles are ceramic fillers and darker regions in between fibers are pores, which explains why paper is very compressible and thus hard to measure thickness using conventional caliper. The nominal thickness of the sample is 100 μm.

data by numerically integrating using the trapezoidal rule.

2.4.2 Machine Compliance Correction

Correction for machine compliance is an important step for accurately analyzing the mechanical testing data. While compliance correction is not included in current paper testing standards [45] it is routinely used in single fiber tensile test methods [52]. The machine compliance was determined by testing two of each 30, 40 and 60 millimeter long specimens in each orientation (i.e., MD and CD) at the same loading rate (3 mm/min) and finding their compliance (inverse of stiffness). Compliance of these six specimens versus their gauge lengths are shown in Figure 2.3. A linear regression was fit through these six points, and the system compliance, C_s, which is y-intercept of the fitted line was determined.

The compliance corrected strain values were calculated by using equation 2.1 where C_a is the compliance of a specimen whose strain values are being adjusted.

$$\varepsilon_{corrected} = \varepsilon_{uncorrected}(1 - \frac{C_s}{C_a}) \tag{2.1}$$

Three different stress-strain curves plotted using uncorrected crosshead displacement, compliance corrected strain, and DIC calculated full field average strain of a representative MD

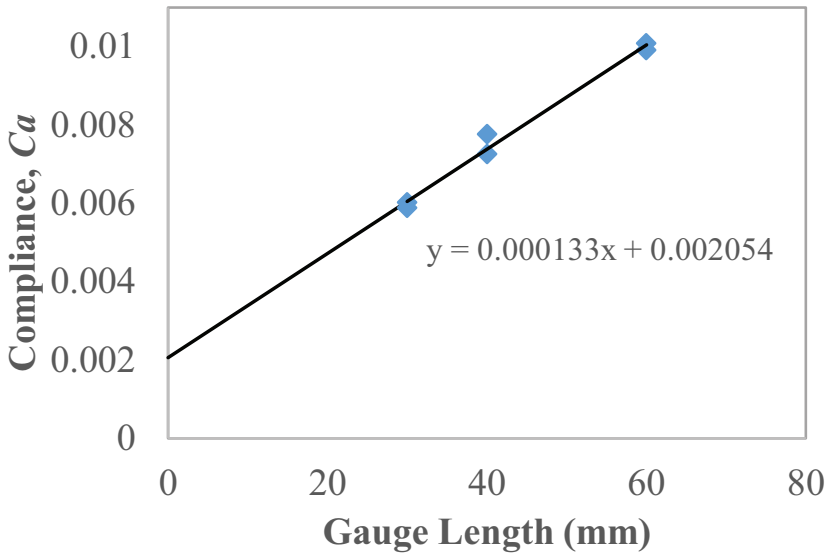

Figure 2.3: Compliance of specimens at different lengths. The machine compliance, C_s, is the y-intercept of the fitted linear regression curve.

specimen are shown in Figure 2.4. Here, compliance corrected and DIC calculated stress-strain curves match very well. Therefore, in this dissertation, compliance corrected and DIC calculated full field average (of all data points) strains were treated indistinguishably.

2.4.3 Weibull Analysis

The Weibull distribution function is commonly used to examine the relationship between flaw populations and strength in materials [53, 54]. Equation 2.2 describes the strength distribution of a material and is also valid for materials that encounter non-homogeneous stress distribution [53]. In this equation, $F(\sigma_c)$ is the strength distribution function, (σ_c) is the inert strength of material, and m and (σ_0) are the two Weibull parameters. m is a measure of scatter of the strengths, where smaller m represents a wider distribution [54]. Equation 2.3 is the logarithmic form of equation 2.2. Two Weibull parameters, m and (σ_0), were obtained by linear fit method and the maximum-likelihood estimator (MLE) method using Numpy and Scipy packages in Python 2.7.8. The Weibull modulus, m, is the slope of the fitted line, and the characteristic strength, (σ_0), is the strength value at

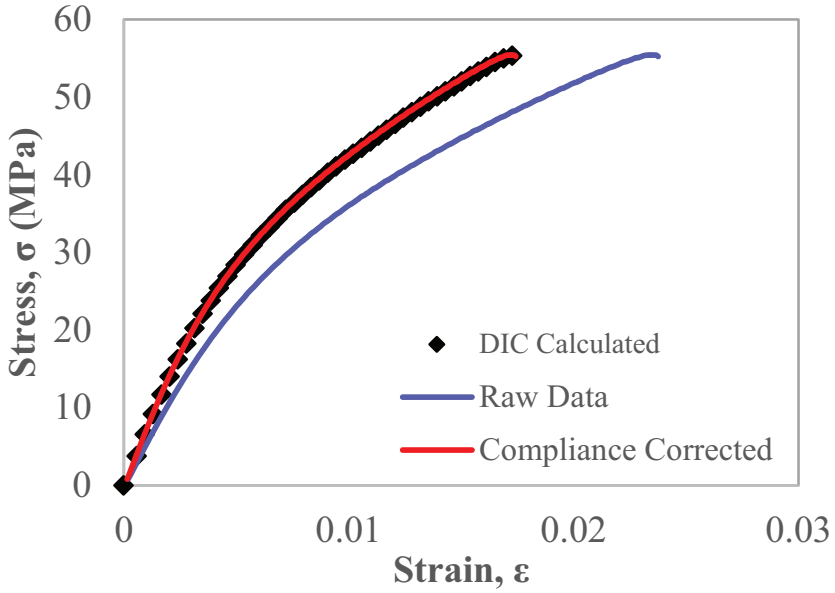

Figure 2.4: Three different stress-strain curves of a representative MD specimen obtained using uncorrected crosshead displacement data (blue line), compliance corrected strain (red line), and DIC calculated full field average strain (black marker).

$lnln(1/(1-F)) = 0.$

$$F(\sigma_c) = 1 - \exp\left(-\frac{\sigma_c}{\sigma_0}\right)^m \tag{2.2}$$

$$\ln\ln\frac{1}{1-F} = m\ln\sigma_c - m\ln\sigma_0 \tag{2.3}$$

For the Weibull analysis in chapter 4, two other sets of specimens (long and narrow) having different specimen dimensions were prepared. The length of the long specimens were changed from 50 mm to 90 mm and the width of narrow specimens were changed from 12.5 mm to 6.25 mm. Both long and narrow specimens were pulled in tension at (3 mm/min) until fracture, and their tensile strengths were recorded.

2.4.4 Lineal Path Correlation

A number of statistical descriptor functions such as n-point correlation, nearest neighbor distribution, lineal path distribution, and radial distribution are often used to quantitatively

describe spatial characteristics of isotropic and anisotropic microstructures [55, 56]. In this work, lineal path correlation, a direction-dependent statistical descriptor, was used to interpret spatial distributions of hot spots in the thresholded strain maps and flocs in optical images. The algorithm of lineal path probability distribution was developed by Singh et al., and a detailed description can be found in their previous publication [55]. Simply, it is calculating the probability that a test line of a specific length, R, and orientation, θ, is completely contained in the area of interest. This statistical descriptor can clearly distinguish isotropic random and anisotropic components in a binary field and provide information about size, shape, and orientation distributions. For anisotropic components, lineal path probability distributions are radically different depending on orientation of the test line. The characteristic length scale of the component in the direction of a test line is defined to be the line length, R, where the probability approaches zero.

$L00$ and $L11$ are the probabilities that a test line is completely inside the background (0) or hot spot (1) areas respectively. $L01$ is the probability that a test line segment of a specific length, R, crosses both components. In the probability curves, where the $L00$ and $L11$ probabilities approached 0.01 was recorded as the characteristic length scale of the region of interest (hot spots or background) in the direction of the test line.

2.4.5 Crack Length and Growth Rate Measurements

As shown in Figure 2.5, unlike in metal specimens, it is difficult to optically define the extent of damage or crack tip in paper because paper is a heterogeneous, fibrous material and the material does not fully separate even with the crack advancement unlike in metallic specimens. Therefore, an alternative strain field mining method was developed to identify the extent of the crack growth. A strain map of a representative copy paper specimen with a growing crack is shown in Figure 2.6(b). From the strain field, the extent of the damage or the location of the crack tip was determined from the continuous region with strains above a chosen threshold strain level, ε_{th} as shown in Figure 2.6(c). The crack length is determined

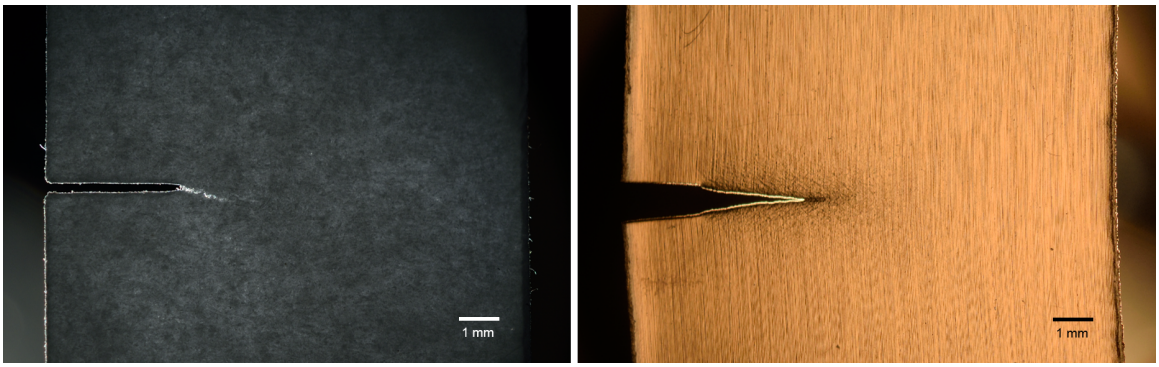

Figure 2.5: Cropped optical images of 100 µm thick copy paper (left) and 127 µm thick Aluminum [57] (right) specimens in the region of cracks. Unlike the full material separation during crack growth in metals, it is very difficult to determine the extent of crack growth in paper.

as the horizontal distance from the left edge of the specimen to the farthest right position of the thresholded region.

A series of threshold levels ($\varepsilon_{th} = 0.05, 0.07, 0.1$) was applied to determine the influence of threshold strain on crack growth measure: as shown in Figure 2.7, changes in the threshold strain level did not change the overall trend of the crack growth, and the average of differences in the crack lengths were 0.36 mm. Thus, for this study, the threshold strain value of 0.05, which is 1.5 times greater than the failure strain of unnotched CD specimens in uniaxial tension (See Table 4.1), was used to define crack the material (significant damage or failure). This criteria guaranteed that the material had separated in the area of strain higher than 0.05. Crack length versus number of cycles (a vs. N) curves for all the fatigue and creep tests shown in this paper (Figs. 5.7, 5.11) were obtained using this unique crack length measurement method.

The crack growth rate was determined by calculating slopes of the a vs. N curve. Figure 2.8 shows a representative a vs. N plot of a specimen cyclically loaded with an alternating stress range of 6.12 MPa. Per ASTM standard E647 [58], the crack growth rate, da/dN, was calculated from the slope of a linear regression of five consecutive data points (highlighted in the figure), and the crack growth rate was attributed to the mid (third) data point of the group. The analysis window was then advanced by one data point, and the

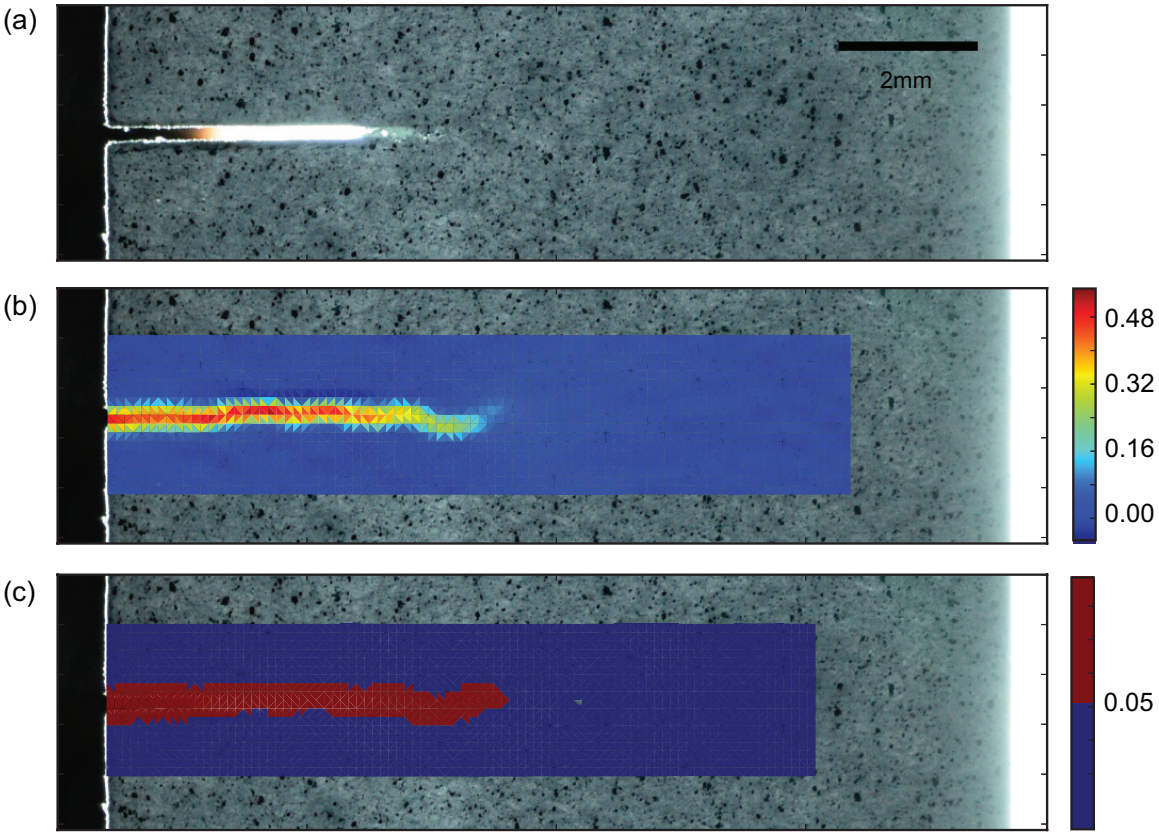

Figure 2.6: (a)A cropped optical image of copy paper specimen having a fatigue crack (b)Overlay of stain distribution near the crack (c)Strain distribution was thresholded so that any region having a greater strain than 0.05 was considered as a crack

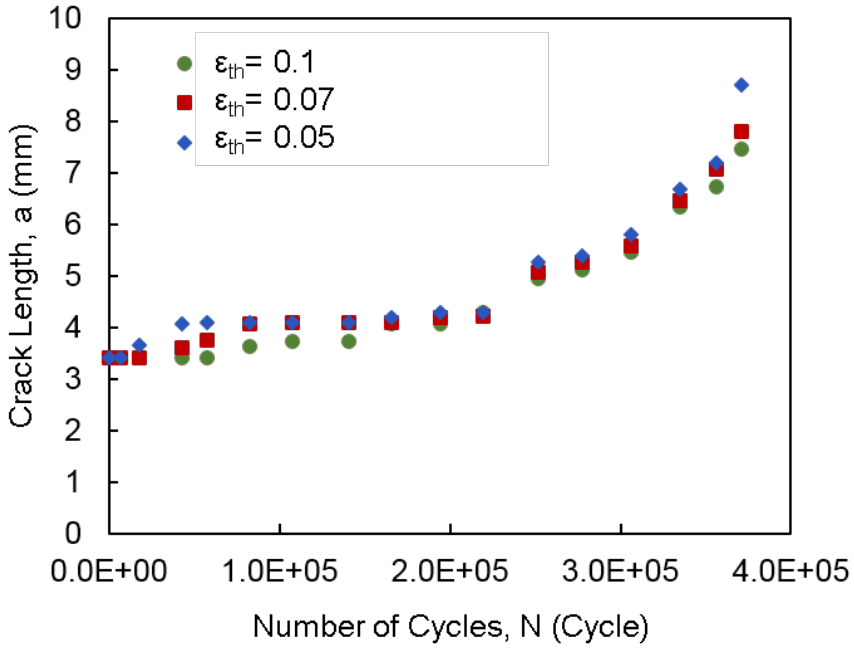

Figure 2.7: Three different threshold strain values of 0.05, 0.07, 0.1 were used to determine crack lengths of a fatigue specimen, and they all resulted similar crack sizes.

analysis repeated.

2.5 Characteristic Length Scale of Formation in Paper

The characteristic length scales of the in-plane floc (fiber agglomerates) and the interfloc regions were determined by performing the lineal correlation analysis (see section 2.4.4) on the post processed light transmitted optical images. This image analysis method has been used to isolate and quantify characteristic length scales of paper formation [59–61]. Light transmission images of copy paper samples were captured using a Nikon D3300 DSLR camera. Using ImageJ [62] software, the following steps were taken to determine local density variations in paper and obtain the formation maps (See [59, 61] for more detailed method): (1) light transmission images were converted to grayscale (Fig. 2.9a). (2) Fast Fourier transformation (FFT) operation was taken on 2048 px by 2048 px areas. (3) Circular filtering was applied on Fourier transformed image to only pass low frequency signals. (4) inverse FFT processing was performed from the filtered FFT power spectrum

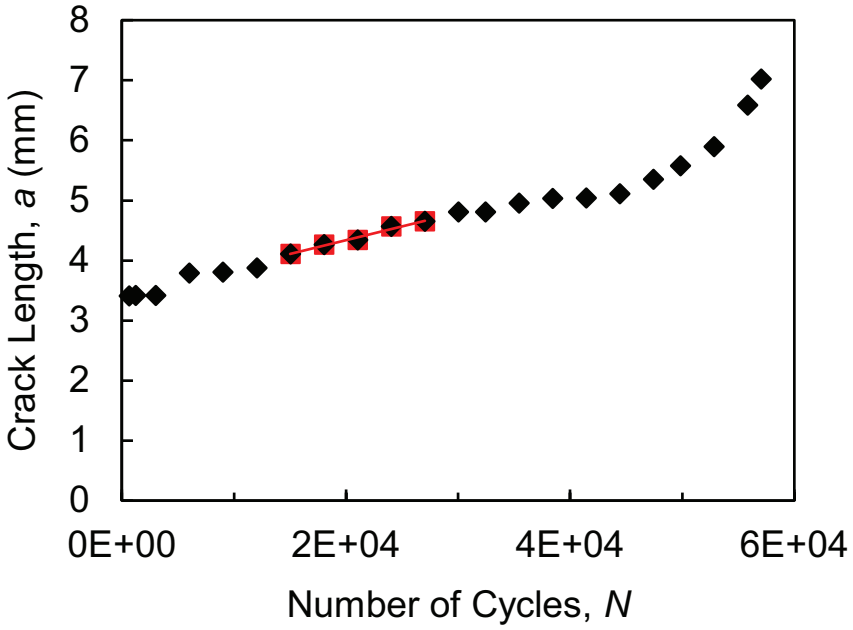

Figure 2.8: Example a vs. N plot of a fatigue specimen ($\Delta\sigma$=6.12 MPa). Groups of five consecutive data points (highlighted) were fitted with a linear regression line, and the slope of this line was taken as the crack growth rate (da/dN) of the mid-data point among the five.

(Fig. 2.9b). After the formation map was obtained, it was converted into a binary image (Fig. 2.9c) using the default automatic thresholding function in the ImageJ. The lineal path correlation analysis [55, 56] was performed on this binary image to find the characteristic length scale of flocs. From this statistical analysis on ten separate samples, it was found that the average size of flocs (high density areas) was 2.99 mm in MD and 2.65 mm in CD. Moreover, the average size of inter-flocs (low density areas) was 2.83 mm in MD and 2.84 mm in CD. From this analysis, it was found that flocs and inter-flocs in the copy paper sample used in this study are approximately 3 mm and nearly isotropic.

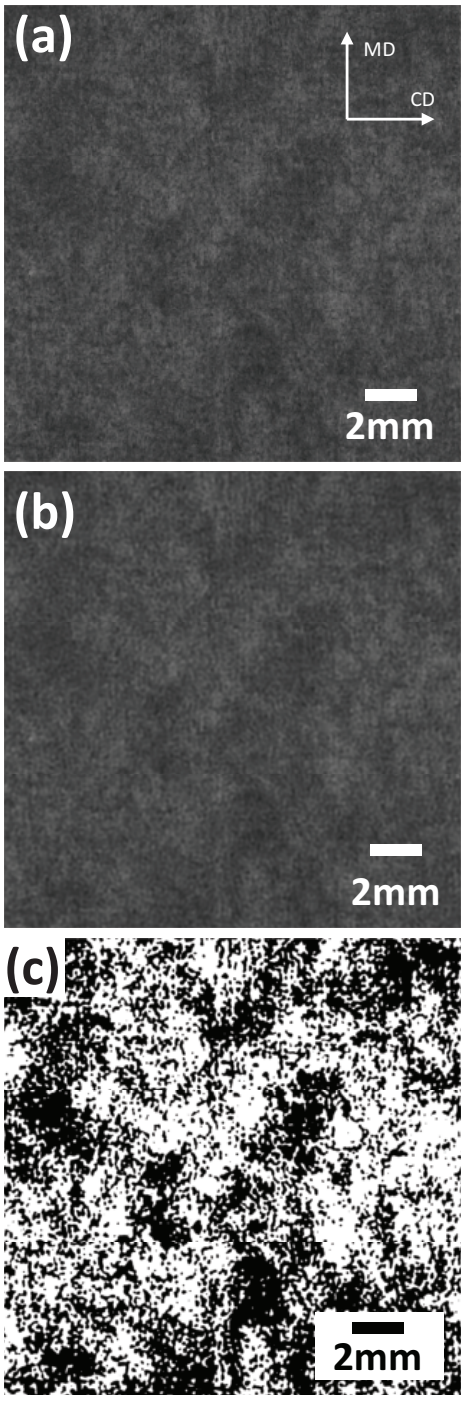

Figure 2.9: (a)Light transmission image of a representative copy paper sample. (b)Formation image obtained with inverse FFT treatment on the frequency-filtered FFT power spectrum. (c)Binary version of the inverse FFT treated formation image shown in (b).

2.6 Structural Characterization

2.6.1 Imaging Tools

In this study, various characterization tools were used to determine the structure of paper. For all scanning electron microscope (SEM) images shown in this work, Hitachi TM3030 bench-top SEM in "COMPO" backscatter imaging mode and "EDX" observation condition. For confocal fluorescent imaging, Zeiss 700 confocal microscope system with Zeiss Zen 2012 software was used. Paper samples were immersed in fluorecent dye solutions (0.0013 M Acridine Orange in ethanol and 0.0028 M Safranine O in DI water) for 3 minutes, washed, and dried. 405 nm laser was used to excite Acridine Orange dyes, 555 nm laser was used to excite Acridine Orange dyes. The paper samples were observed using 10X (dry), 20X (dry), and 40X (oil) objective lenses. For micro-computed tomography (micro-CT), Scanco microCT50 at 2 µm and 900 nm voxel sizes and 200 µA current was used. A small strip of sample was cut and positioned vertically in a cylindrical sample holder and scanned at an orientation where axial cross-sectional images are through the thickness of paper sample. Micro-CT test scans were performed by Angela Lin at Petit Institute Microcomputed Tomography Core facility.

2.6.2 Resin Embedding and Sectioning of Paper

To characterize the planar cross sections of paper, copy paper and filter paper specimens were embedded in Spurrs resin [50], which is a mixture having the weight proportion of 10.0 g cycloaliphatic epoxide resin (ERL 4211), 6.0 g diglycidyl ether of polypropylene glycol (D.E.R 736), 26.0 g nonenyl succinic anhydride (NSA), and 0.4 g dimethylaminoethanol (DMAE). Spurr's resin is often used as an embedding medium for biological materials and is ideal for mounting papers because it fully impregnates through cellulose fibers and is hard and tough [63]. The first three components were mixed in a beaker with a stirring bar. DMAE was added at the end, and the solution was stirred gently to mini-

mize air entrapment. The paper specimen was placed on a mounting cup with a plastic coil sample holding clip to hold specimen straight and perpendicular to the surface. De-gassed Spurr's resin was then poured in the mold, and the block was cured in an oven at 70 °C for at least 8 hours.

Two different methods, microtomy and hand grinding, were performed on the cured resin block to reveal the cross section of paper. The first tool used to section the sample block was rotary microtome. Waldorf HM355S Microm rotary microtome with a Tungsten carbide blade was used to section the block. The feed thickness of 15 µm to 20 µm was achieved. The second method was hand grinding the resin block and removing a thin top layer of resin to expose the paper cross section [26, 34]. The sequence of grinding consisted of grinding the cured resin face on abrasive paper of 180, 400, 600, 1200 grit. The grinding was done dry with a light pressure, and the block was hand-held and moved in a single direction for 30 s to 2 min, rotating 90 degrees every time grit size was changed. The block face was cleaned with Methanol and dried between the changes in the grit size. After the grinding stage, the block face was polished with 1 µm diamond lapping films. For the resin removal, a mixture of 3 g of KOH pellets and 15 mL of 99.8 % Methanol was mixed. It was stirred until all KOH pellets were dissolved. The polished resin block was then dipped slightly in the solution so that only the surface was wet for 30 s. After dissolving, the block face was rinsed with fresh methanol and dried in the hood before examination in the SEM.

CHAPTER 3
STRUCTURAL CHARACTERIZATION OF PAPER

The structure of the copy paper used for all the mechanical tests in this dissertation was evaluated using various characterization techniques such as microtomy, grinding, CLSM, and micro-CT. These techniques have been used to characterize the 2D and 3D structures of paper (introduced in Section 1.1). The surface of paper can be easily imaged with the scanning electron microscope (SEM); however, characterizing the inner structure is more difficult (but essential) because paper is made of multiple layers of cellulose fiber network. Along with the characterization results, the challenges of obtaining the structure of paper using each technique will also be discussed.

3.1 Introduction

Characterizing the structure is important for determining the influence of structure on the mechanical properties of paper. Depending on the observation length scale and details to be characterized, paper structure can be characterized using different methods. The mesostructure (milli-meter length scale) of paper can be represented by flocs, which are regions where fibers are more concentrated than the rest of network. Previous research has shown that formation in paper affects strain localization and that low grammage zones localize strains and eventually lead to fracture [36, 41, 42]. The grammage variation in paper can be accurately measured using beta radiation as beta rays get attenuated and absorbed in proportion to the mass passed through without scattering [64]. For a quicker analysis, diffuse light transmission measurement can be used to approximate the local grammage. Figure 3.1 shows a binarized optical image of formation of paper through transmitted lighting (methods shown in section 2.5). For the copy paper used in this work, it was found that the average size of flocs was 2.99 mm, more than hundred times larger than the average

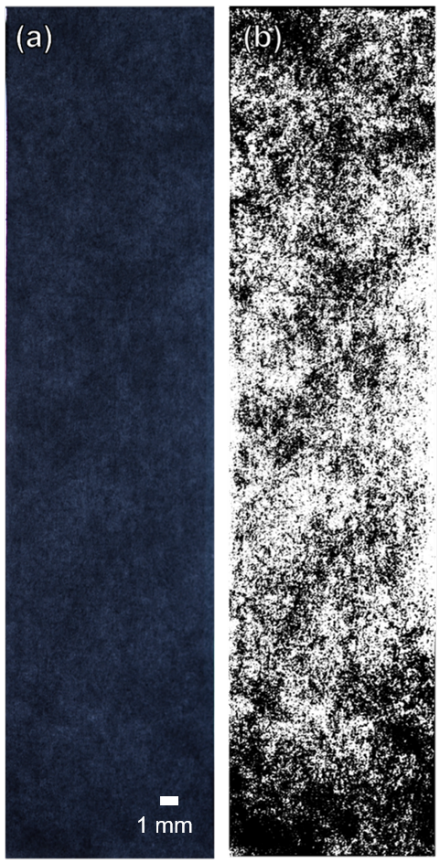

Figure 3.1: Mass distribution (formation) of a copy paper tensile specimen

fiber width (21.6 µm). However, the mesostructure characterization is not enough for modelling the fiber network at the fiber length scale. In order to gain information about the 3D inner structure of paper, the paper sample must be characterized at least at the micrometer length scale.

3.2 Cross Sectioning of Paper

The 2D cross sections of paper can be easily imaged using SEM, and the serial cross sectioned images can be potentially reconstructed to a 3D structure. Figure 3.2 shows SEM images of copy paper cross sections that were cut using a scissor blade and an IR laser beam. The scissor cut cross section shows that fibers on the outer surface layer were crushed towards the direction of the moving blade. Thus, the fibers on the top surface

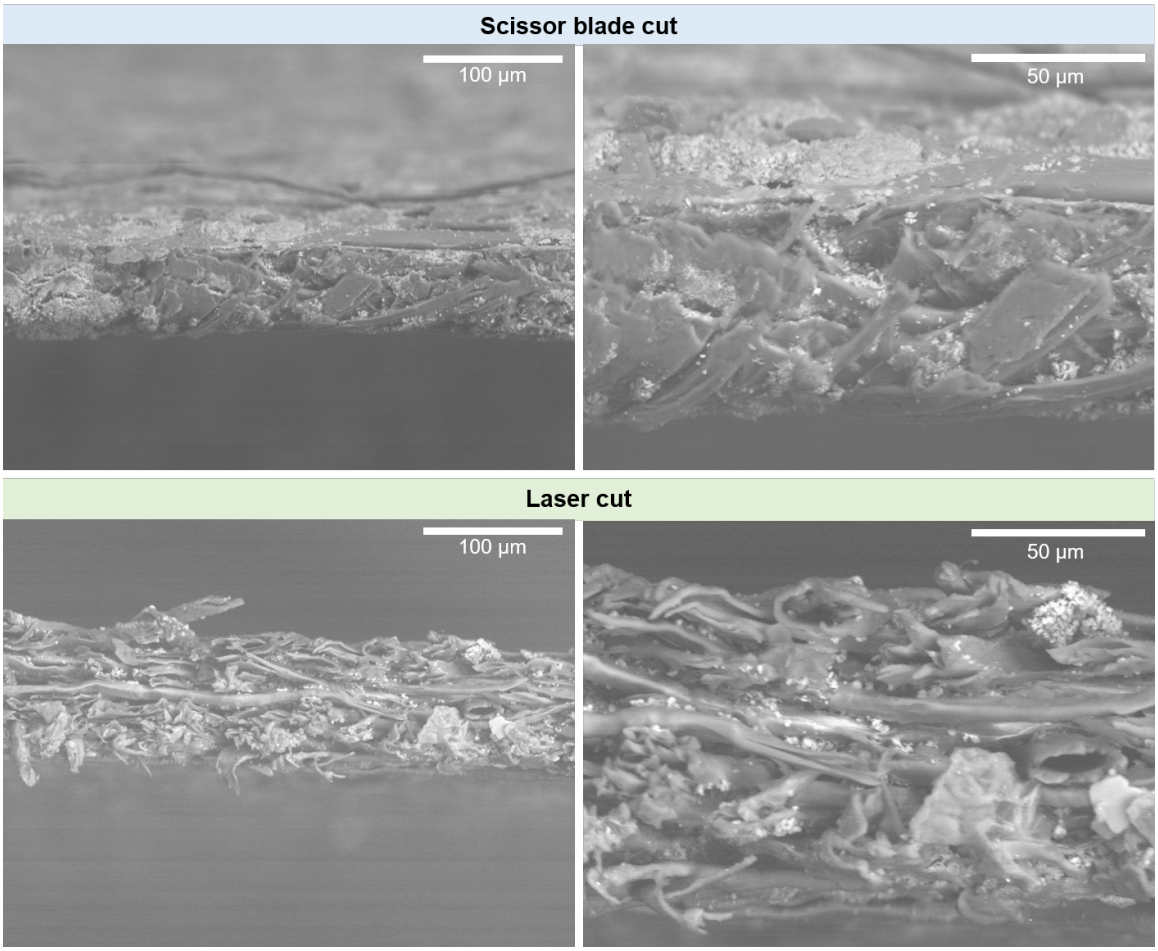

Figure 3.2: Cross sections of copy paper sample cut using a scissor blade and an IR laser beam.

layer hid the inner network structure. The laser cut cross section did not have the crushing problem, but the cut was not clean enough to clearly obtain a planar image of the cross section. Therefore, the paper samples were embedded in epoxy resin and sectioned using mircotome sectioning and hand grinding techniques.

3.2.1 Microtome Sectioning

Figure 3.3 shows SEM images of a 20 µm slice of copy paper embedded in the CD orientation (direction going in and out of page is the CD). The paper sample was distinguishable from the surrounding embedding resin; however the contrast of the individual fibers was not great due to the penetrated resin filling the pores within the network. Moreover, parts

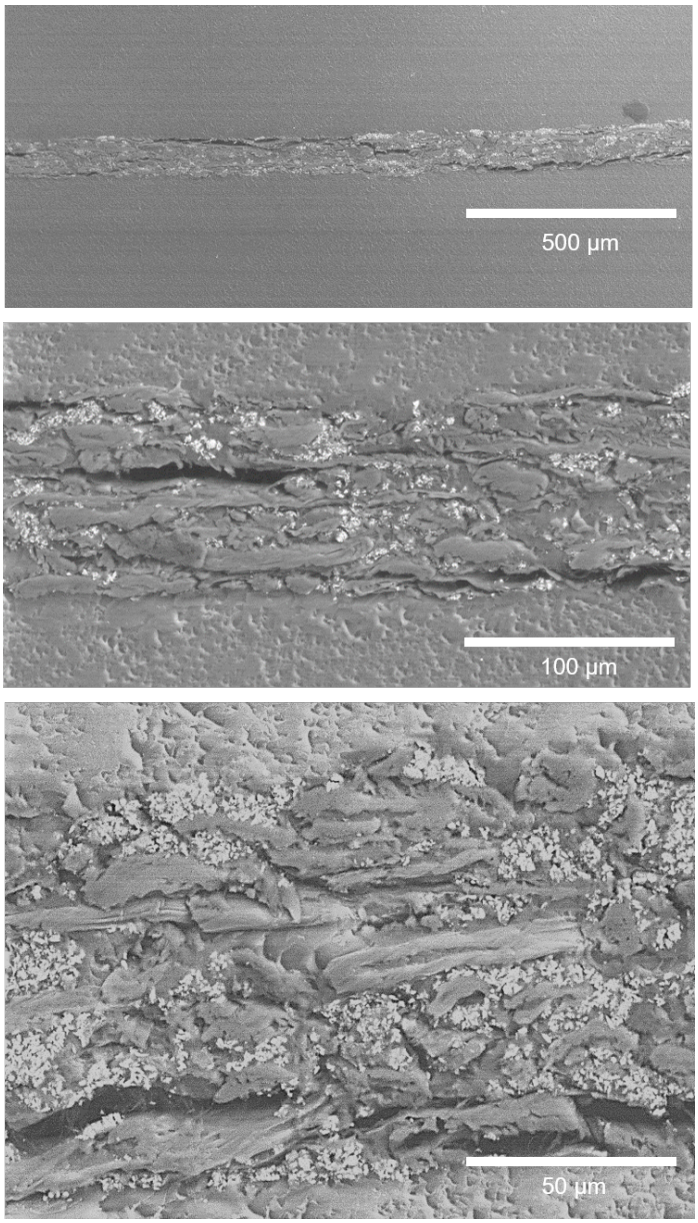

Figure 3.3: SEM images of a 20 µm microtome slice of copy paper embedded in CD orientation.

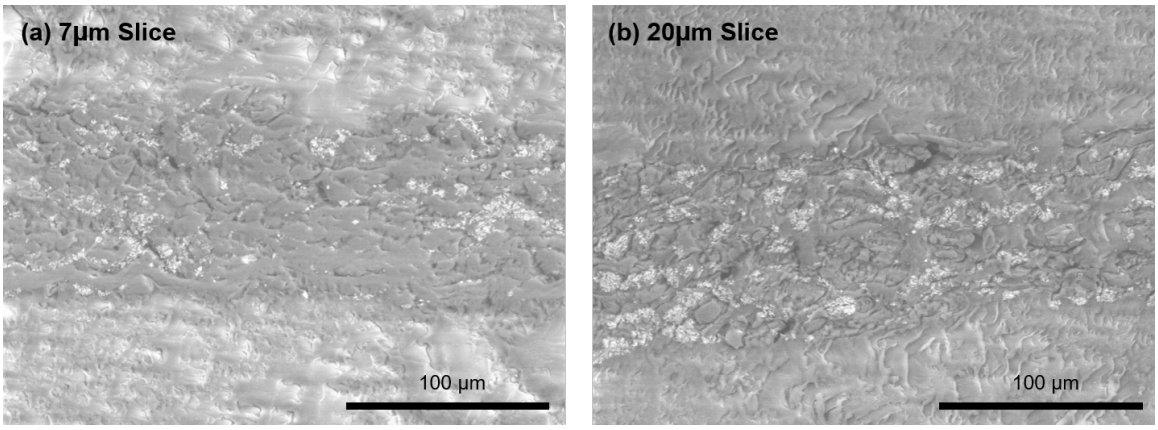

Figure 3.4: SEM images of (a)7 µm and (b)20 µm microtome slices of copy paper sample embedded in MD orientation.

of the fiber layers were cracked from the embedding resin, possibly during sectioning or handling stages. Figure 3.4 shows cross sectional images of 7 µm and 20 µm microtome slices embedded in the MD orientation. Changing the thickness of the microtome slices did not improve imaging quality, although thicker samples were easier to handle after they were sectioned. The limitations to microtome sectioning were obtaining clean sectional surface and strong contrast between penetrated resins and fibers. With these conditions, it was not possible to successfully stack sections and reconstruct them into a 3D image.

3.2.2 Hand Grinding and Resin Removal

The limitations of microtome sectioning was overcome with the hand-grinding and resin removal method [26]. Figure 3.5 shows the hand-grinded and resin removed cross sectional image of copy paper sample embedded in MD orientation. Unlike the cross section obtained with microtome sectioning (Fig. 3.3), the hand-grinded and surface-resin removed cross section showed the structure of fibers and pores clearly. The contrast between fibers, ceramic fillers, pores, and the resin was high. The improvement in the contrast was due to the resin removal step as shown in Figure 3.6. Before the resin removal, the cross sectional image of hand-grinded filter paper surface resembled that of the microtome one where the contrast between individual fibers and pores were poor. After the resin removal step,

the structure of fibers and pores were revealed, and even lumen inside the cellulose fibers were able to be discerned. Note the filter paper did not contain any ceramic fillers, and the thickness of the paper was nominally 160 µm. Because the individual fibers were distinguishable, it was possible to threshold the image to isolate fibers from the rest of the structure (Fig. 3.6(c)). The outcome was promising, but depending on the depth of resin removal layer, fibers exposed in lower depth could lead to misinterpretation of fiber shape and orientation. Therefore, obtaining the optimal resin removal depth and contrast for the binary image is necessary.

Although the cross-sections of hand-grinded and resin removed samples resulted better image quality in showing the cross-sectional structure of paper, there still remains challenges for fully characterizing the paper structure. The width of the images in Figure 3.6 is approximately 320 µm. The width of the specimen tested in this study was 12.5 mm and the height was 50 mm. To characterize the cross-section of the full specimen width (12.5 mm), at least 20 images had to be manually stitched as shown in Figure 3.7. The difficulty in analyzing such structure comes from the planar nature, meaning the thickness to width or length ratio is very large. Moreover, hundreds cycles of "grinding and polishing – resin removing – imaging – stitching and thresholding" steps need to be taken to be able to reconstruct the 3D structure of paper. If each grinding step removed 50 µm of the sample, 200 cycles of grinding should be done and 20 images should be taken and stitched for each cycle in order to characterize a 1 cm^2 sample, which require approximately 600 hours of work excluding the reconstruction. Therefore, the manual sectioning method is very time consuming and nonideal for characterizing a large volume of paper structure.

3.3 Confocal Microscopy

Confocal laser scanning microscopy is a nondestructive imaging technique that has an optical sectioning capability. Figure 3.8 shows 2D images of copy paper and filter paper samples stained with Safranin O and Acridine Orange fluorescent dyes. The filter paper

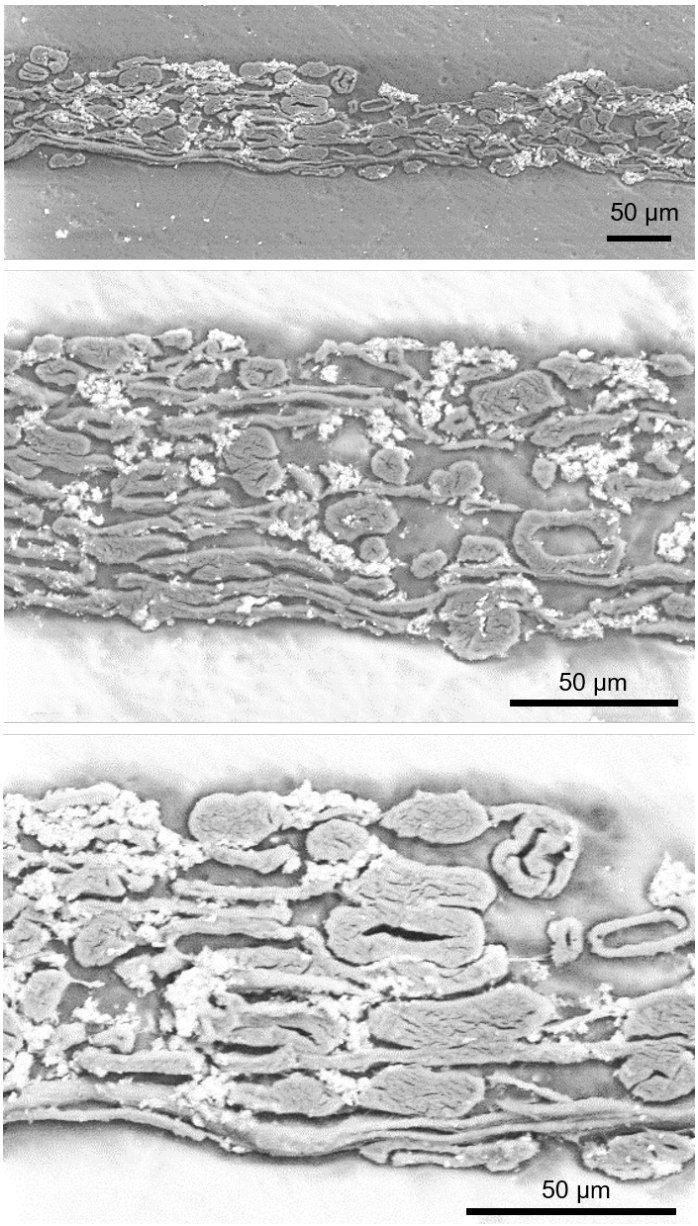

Figure 3.5: SEM image of a hand-grinded and resin removed cross section of copy paper sample embedded in MD orientation.

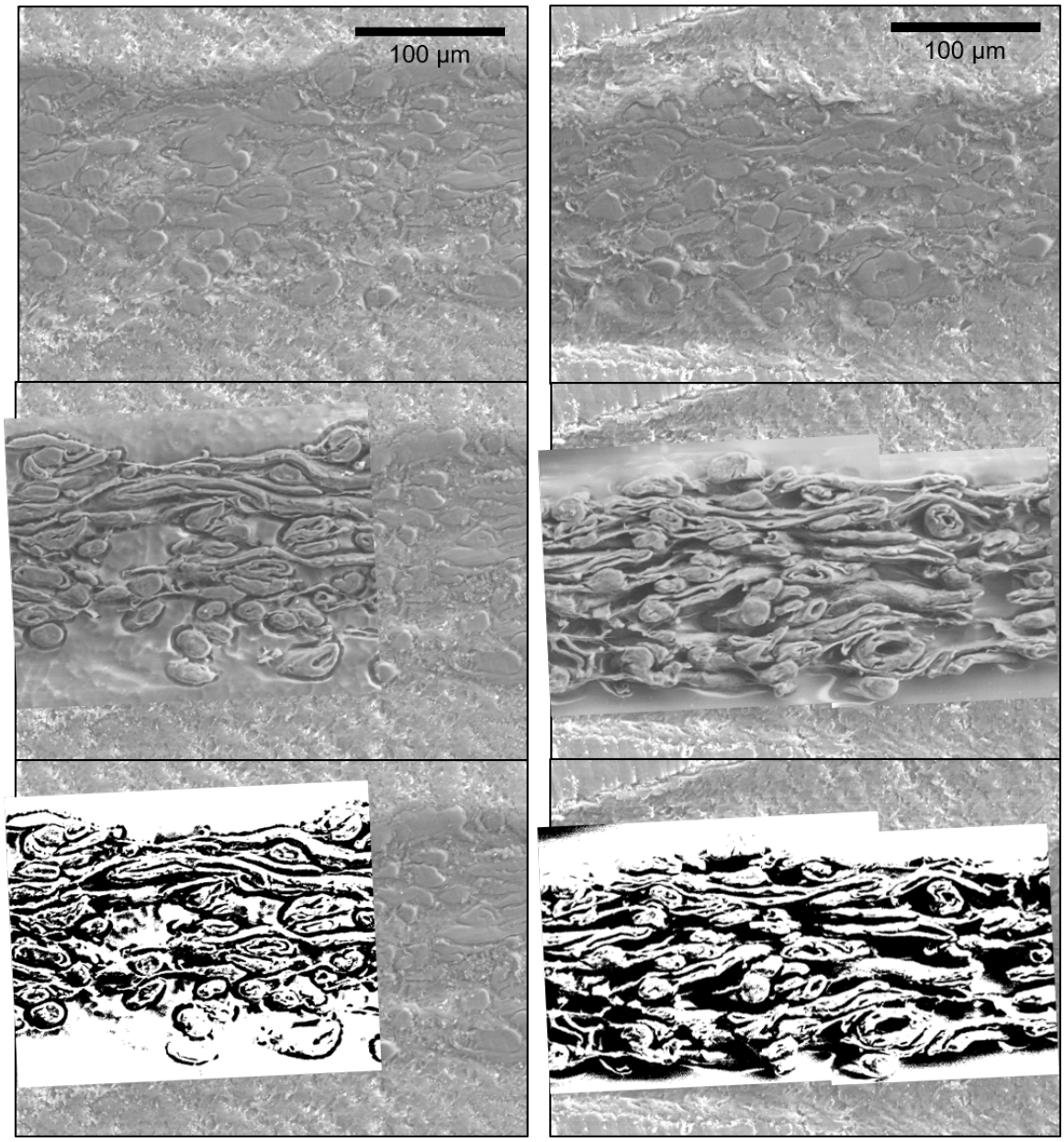

Figure 3.6: The cross-sectional images of a filter paper sample embedded in CD orientation (a)after grinding, (b)after resin removal, (c)after thresholding.

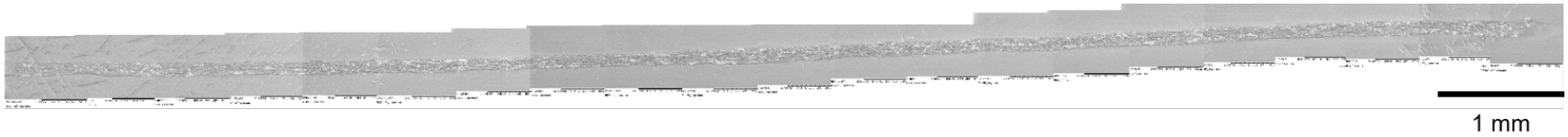

Figure 3.7: Stitched image of cross section of a copy paper specimen in full width (12.5 mm)

was imaged better than the copy paper, possibly due to the material not having any ceramic fillers in the structure. Also, the contrast and image quality was better for the sample stained with Safranine O. Figure 3.9 is the 3D reconstructed images of the filter paper sample stained with Safranine O. The reconstruction was done by z-stacking a series of 2D scans from the surface layer to the inner layer of fibers. However, the fluorescent signal was quickly attenuated, and there was limitation on from how deep the scans can be achieved, consistent with values reported in the literature [28]. Each scan yielded $320 \times 320\,\mu m^2$ and $160 \times 160\,\mu m^2$ images for 20X and 40X objected lenses respectively, and the deepest scan was obtained from 50 µm below the surface layer, which was not sufficient to fully characterize 100 µm copy paper and 180 µm filter paper.

3.4 Micro-computed Tomography

Micro-computed tomography (micro-CT) is a nondestructive X-ray imaging technique used for 3D network visualization of paper at a micrometer resolution. Figure 3.10(a) shows a test cross sectional scan of the copy paper sample obtained with a 2 µm voxel size. The nominal thickness of specimen in the image was about 100 µm as expected. The resolution of the image was not great in that the fibers were not fully distinguishable, and there was some amount of noise in the background that affected the image quality. As shown in Figure 3.11, ideally, these 2D scanned images will be thresholded to isolate individual fibers and to reconstruct 3D images. However, the thresholded, binary images clearly showed that it was hard to resolve individual fibers in paper because of the poor resolution. Quantitatively using the thresholded images, the object volume and average linear attenuation coefficient were calculated to be $0.0437\,mm^3$ and $2.0781\,cm^{-1}$. Figure3.10(b) shows a test scan performed with a 900 nm voxel size. Compared to the one obtained with a 2 µm voxel (Fig. 3.10(a)), the resolution and contrast between fibers and pores were slightly improved. However, the image quality was still not good enough to be used for 3D network structure reconstruction and could only be improved by using a higher quality X-ray or synchrotron

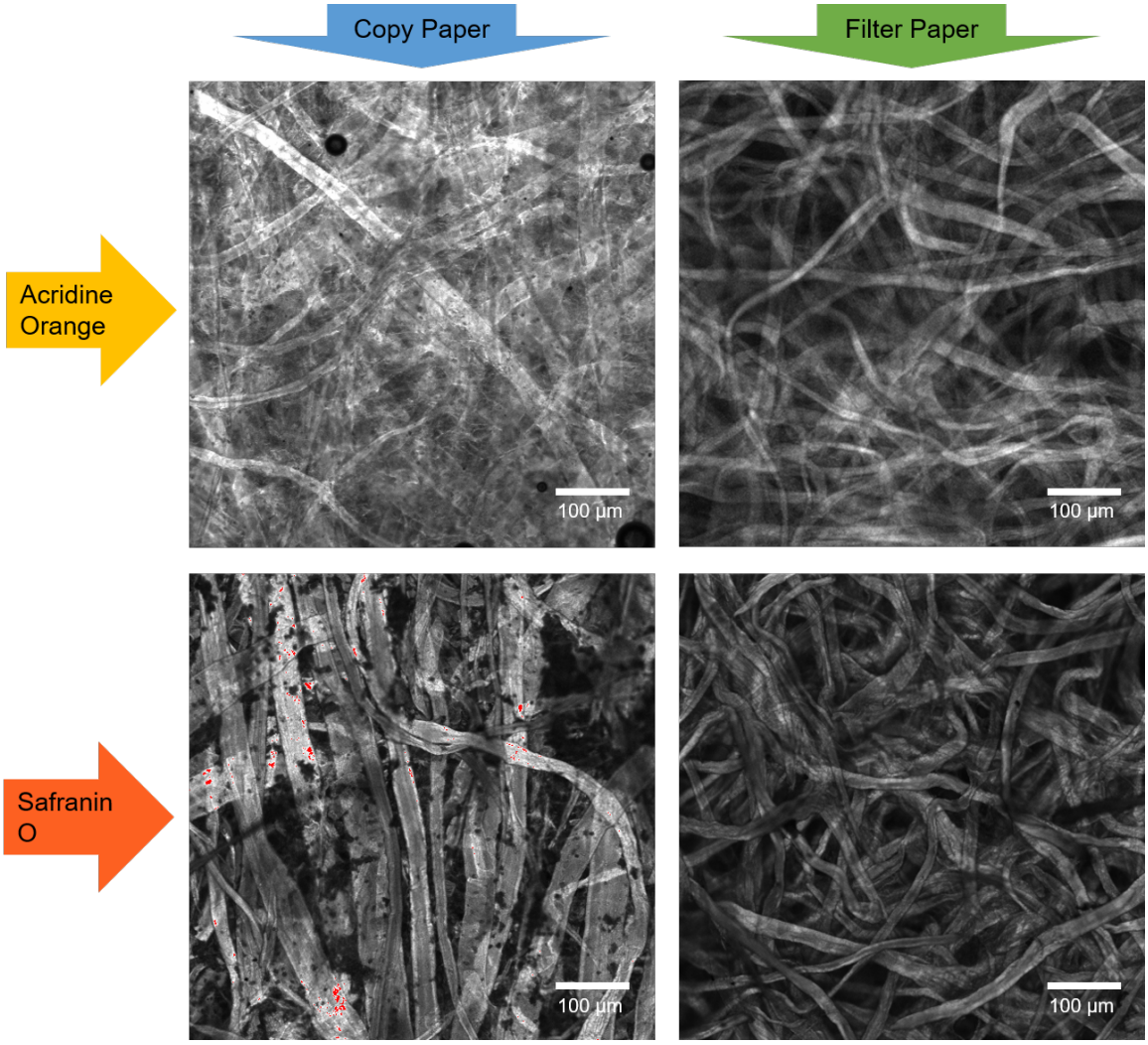

Figure 3.8: Representative 2D section of copy paper and filter paper samples stained with Acridine Orange and Safranin O dyes.

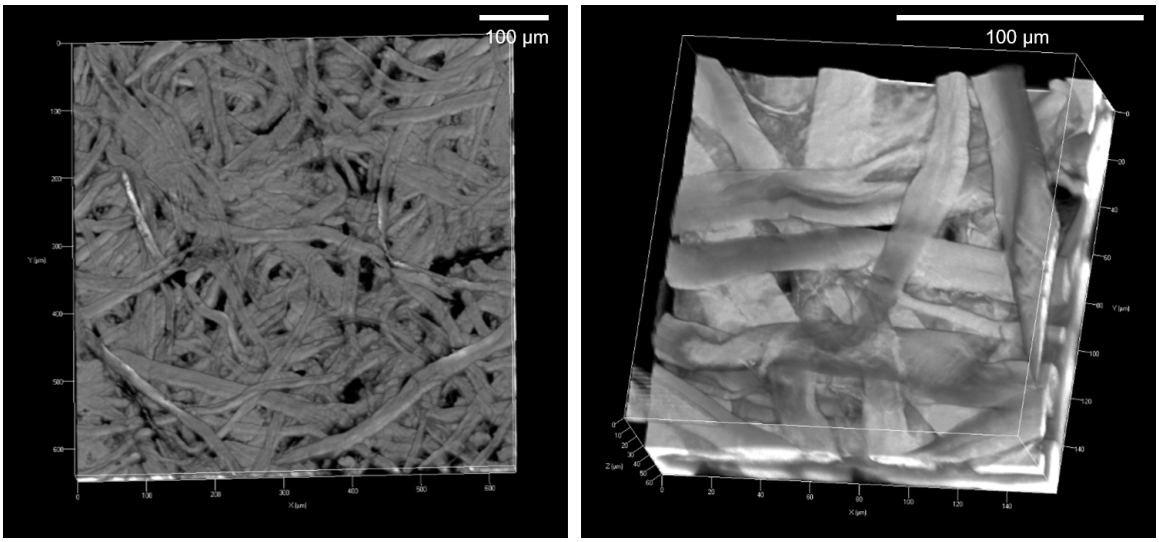

Figure 3.9: Z-stacked 3D reconstruction structure of the filter paper sample stained with Safranin O dyes, imaged with 10× dry lens and 40× oil lens.

sources.

If there were no resolution issue and experimental limitations, density variation in paper specimens could also be quantified using micro-CT analysis. For example, in Figure 3.12, two isolated regions were selected with small green contours. The total volume of these analysis regions, calculated with number of slices down this shape, and the volume of object (fibers) were used to calculate the volume fraction of fibers, which were 0.8304 and 0.8559. For using the 900 nm voxel size, the sample had to be fitted in a 2 mm diameter cylinder, and it took 2.2 hours to scan less than a 0.2 mm height of the sample. Because the technique requires expensive resources and time to overcome resolution and experimental limitations, micro-CT was not an ideal technique for characterize large volume of paper structure.

3.5 Conclusions

In this chapter, the structure of paper was evaluated using microtomy, grinding, CLSM, and micro-CT. Although details of fiber and pore structures of the planar slices of paper were obtained with the grinding and resin removal technique, it was too time consuming

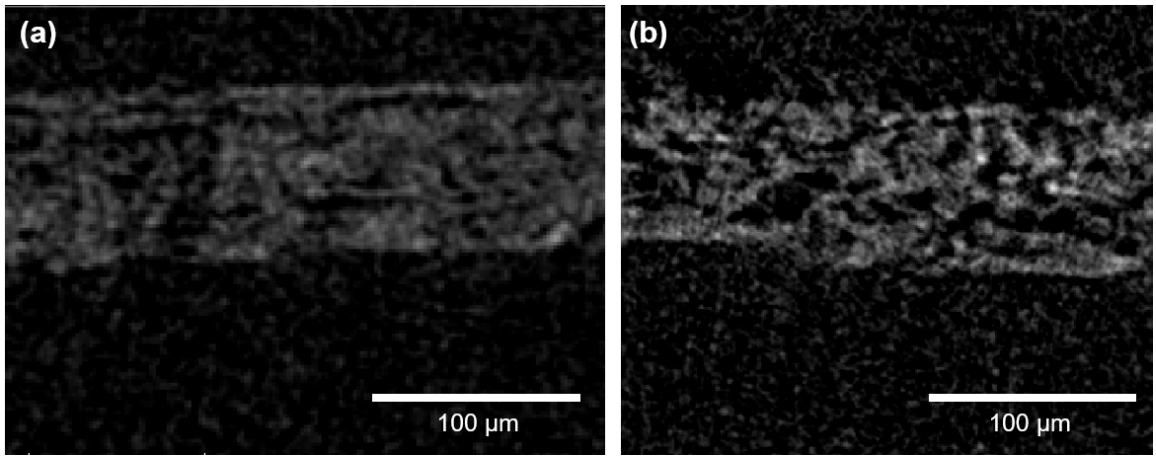

Figure 3.10: Test scans of copy paper sample using (a)2 µm voxel and (b)900 nm voxel sizes.

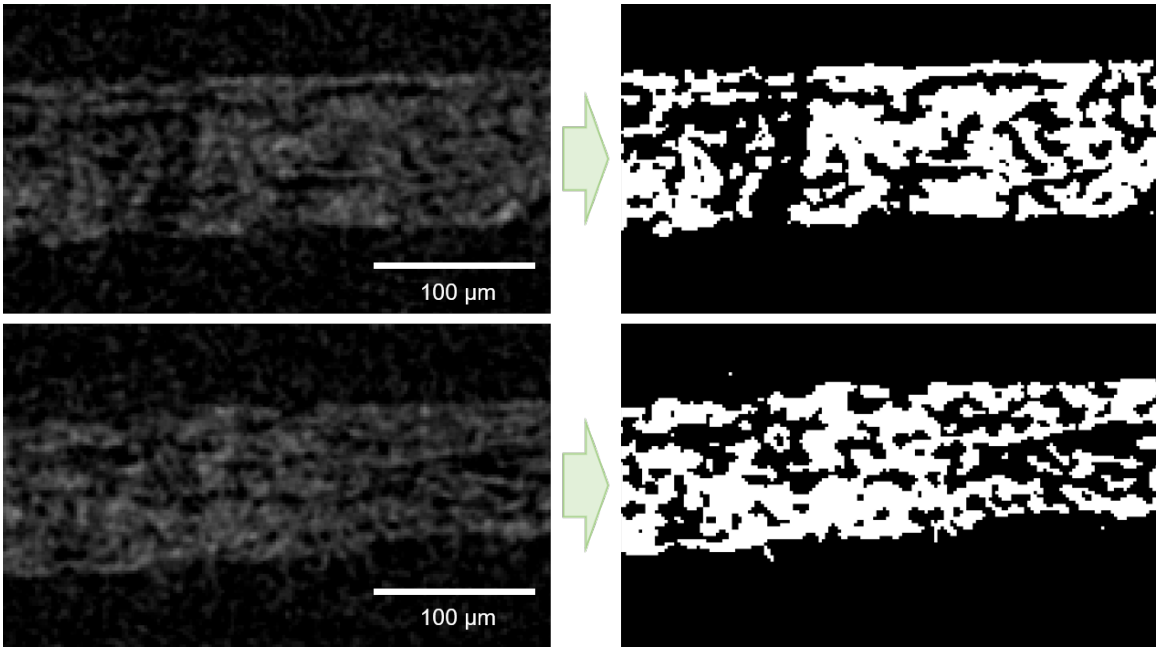

Figure 3.11: Thresholding images of test scans of copy paper sample obtained with a 2 µm voxel size.

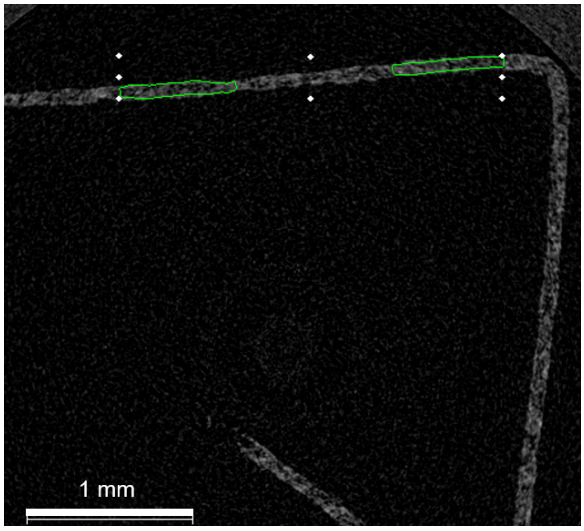

Figure 3.12: A scanned cross-section of a copy paper sample obtained with a 900 nm voxel size. Two isolated regions were selected (indicated with green contours) to compare the volume fraction of fibers.

to use this method to characterize a large volume of paper. CLSM and micro-CT on the other hand had optical sectioning capabilities that can ideally produce a 3D reconstructed structure of fiber network. However, both techniques had resolution issues and were not successful. Therefore, we cannot rely on structure characterization to find its relationship to the mechanical properties of paper. Therefore, in the following chapters, we will use microstructure and mesostructure of the strain fields to determine deformation, fracture, and subcritical crack growth mechanisms in paper.

CHAPTER 4

NONAFFINE TENSILE DEFORMATION OF PAPER

This chapter will discuss how strain fields and deformation maps of paper specimens under tensile loading revealed new information that could not be revealed from macroscopic tensile relationship and properties. The heterogeneous strain fields and nonaffine deformation maps were quantitatively analyzed using strain field mining. The strain hot spot locations were identified, and the characteristic shapes and length scales of these hot spots were calculated using thresholding and lineal path correlation. The spatial distribution and extent of nonaffine (non-continuum) deformations during tensile loading of a commercial paper were quantified, and how they were critical features of deformation and tearing mechanisms in paper will be shown.

This work (except the Weibull data) has been published in Experimental Mechanics [65].

4.1 Introduction

The porous, cellulosic fiber networks in commercial paper are generally regarded as continuum materials when the sheet is large compared to the size of fiber agglomerates (flocs). The properties of the fibers, their topology, and the interfiber bonds control the physical properties of fiber network materials (see [10] for a comprehensive review). For example, experimental and numerical studies have established that mechanical and fluid transport properties of the fiber network materials change markedly as the density of bonds and the stiffness of the network increase [10]. Fiber networks in most commercial paper and packaging materials have relatively high bond densities and stiff topologies, so nonaffine deformation has not been perceived as an important issue. However, some numerical models have demonstrated that *all* network structured materials should exhibit nonaffine deforma-

tions, even when the topology is dense and stiff [16]. The following sections demonstrate that fiber networks in paper specimens exhibit significant nonuniform deformations transverse to the loading direction that can be used to identify fracture initiation regions.

4.2 Results and Discussion

The compliance corrected stress-strain curves and the average tensile properties of 60 MD and CD specimens are shown in Figure 4.1 and Table 4.1. Note that stress-strain (full-field averaged) response obtained with DIC was the same as the compliance corrected stress-strain curves (see section 2.4.2 and Figure 2.4) and was similar to data previously reported in the literature [1, 7, 17, 66]. The initial portion of the curves was linear, and above the yield point became nonlinear. As expected, MD specimens had higher elastic moduli and tensile strengths, and CD specimens had higher yield and tensile strains. This mechanical anisotropy is typical in machine made papers and is caused by a preferential fiber alignment in the machine direction and an orientation-dependent constraint during drying process [1].

The reproducible tensile curves (Figure 4.1) and low standard deviation values of the tensile properties (Table 4.1) are usually used as an implicit validation that the specimens are much larger than the representative volume element and that paper deforms as a continuum material. Clearly, the specimens in this work were large enough based on these criterion and the consistency in the macroscopic tensile behavior observed in Figure 4.1. However, we will show in sections 4.2.2 and 4.2.4 such a perspective is misguided on fundamental grounds.

The strength distribution of 60 tensile specimens in each orientation was further examined using the Weibull distribution function, which is commonly used to study the relationship between flaw populations and strength in materials [53, 54, 67]. Figure 4.2 shows the Weibull diagrams representing the distribution of tensile strengths of 60 MD and CD specimens. Two Weibull parameters, m and σ_0, obtained by the linear fit and MLE methods are listed in Table 4.2. The Weibull modulus, m, was greater than 20, which is a very high

value compared to the typical brittle materials where failure is controlled by weakest link (Weibull) statistics (e.g., 5-10 for glass) [2, 68, 69]. The high Weibull modulus meant that the variability of tensile strength in the copy paper was low. However, as shown in Figure 4.2, the scatter plot deviated from linear fits, where r^2 values were 0.926 for the MD and 0.961 for the CD specimens. The deviation from the linear fits suggest two possible reasons for the deviation from the Weibull relationship. One possibility was that the failure of paper is not governed by the weakest link statistics, and the other possibility was that paper has multiple flaw populations rather than a single flaw type. Among the 60 specimens, failure started from the side edge for some specimens and from the inner network for others. If flaws causing the edge failure and flaws causing the inner failure were two different defects, the strength distribution would have been separated into two populations. However, no correlation between the failure origination location and the strength was found.

For materials whose failure is controlled by the weakest link statistics, the specimen size and the mean failure strength are related [54]. Since the probability of finding the flaw in a larger area is higher, the mean strength of larger specimens is smaller. Thus, the Weibull statistics on different sets of copy paper specimens of various sizes were examined. The tensile strengths for longer ($l = 90\,\text{mm}$) and narrower ($w = 6.25\,\text{mm}$) specimens were obtained by running uniaxial tensile tests in the same loading condition as the original specimens ($l = 50\,\text{mm}$, $w = 12.5\,\text{mm}$). The Weibull diagrams of the original, long, and narrow specimen sets in MD and CD orientations are shown in Figure 4.3. In order to account for the specimen dimensional change, these strength distribution scatter plots were shifted with a volume scaling factor as shown in equation 4.1.

$$W_i = W_0 + \ln \frac{V_i}{V_0} \tag{4.1}$$

Here, W_i is the shifted strength distribution using the volume scaling factor, $\ln \frac{V_i}{V_0}$. Since the thickness of specimens did not change (0.1 mm), the volume scaling factors ($\ln(1.8)$ for

the long, $\ln(0.5)$ for the narrow specimens) and the area scaling factors ($\ln(1.798)$ for the long, $\ln(0.504)$ for the narrow specimens) were close enough to be considered the same. Even with the shift taking care of the dimensional change of specimens, the Weibull plots did not overlap. Thus, the strength distributions of paper specimens did not scale with size of the specimen in a manner consistent with the weakest-link statistics. This means that the failure was not controlled by defects or weak links that scaled with volume of surface area of paper and what controlled the failure of paper was not directly related to the specimen size. Hristopulus et al. claimed that the strength of newsprint paper followed weak-link scaling, but the Weibull plots presented nonlinear behavior and the sample size scaling did not work [70]. It is well known that paper is a fiber network material and each fiber typically has 50 bonds with other fibers and that the interfiber bond failure is one of the micromechanisms that leads to paper fracture [2]. Therefore, paper fracture was caused by hundreds of bond failure and fiber fracture events, which explains why Weibull statistics could not be used to explain fracture in paper. The microscopic defects (i.e., cracks, holes, shives) do exist in paper, but they are rarely dominant contributors to failure and for controlling the strength of paper [1, 2]. The high Weibull modulus (homogeneity) and the deviation from the weak link theory suggest that the average network properties, rather than a single defect, must be responsible for the strength of paper [2, 71]. Thus, it is crucial to directly examine how the network deforms under a load (e.g., strain maps) to identify network features that control the failure.

4.2.1 Poisson's Ratio

A popularly used continuum mechanics based orthotropic elasticity relationship [20, 72] shown in equation 4.2 describes the anisotropy in the mechanical properties of paper. The orthotropy is expressed with the Maxwell relation where E_{MD} and E_{CD} are elastic moduli

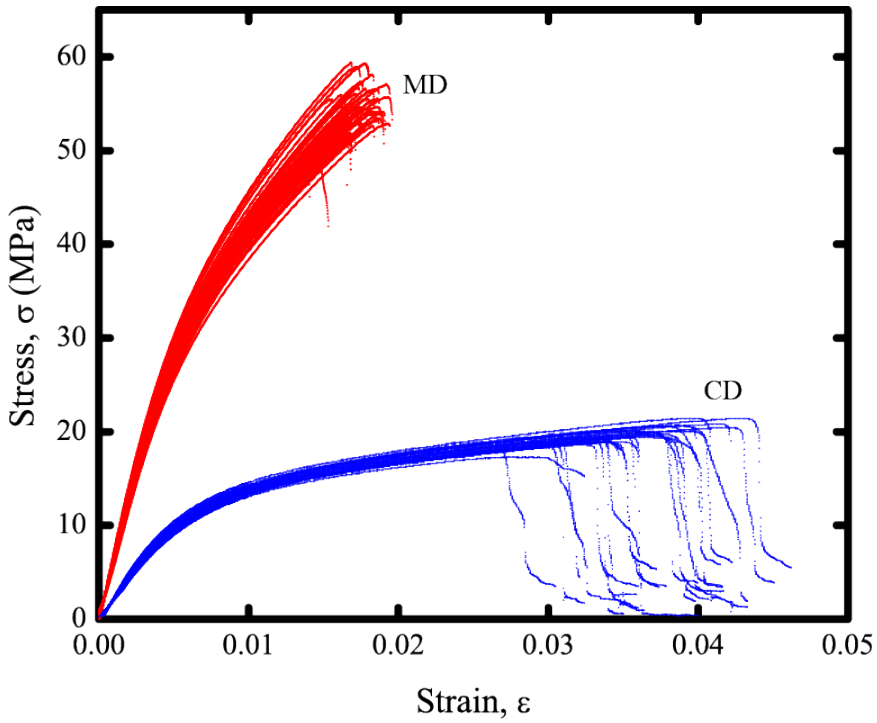

Figure 4.1: Compliance corrected tensile stress-strain curves of MD and CD specimens

Table 4.1: Average (number of samples, n=60) tensile properties of copy paper in two orthogonal orientations

	MD	CD
Elastic Modulus, E (GPa)	6.52 ± 0.28	2.23 ± 0.11
Yield Strength, σ_y (MPa)	16.3 ± 0.95	6.02 ± 0.23
Tensile Strength, σ_f (MPa)	54.0 ± 2.35	19.9 ± 1.03
Yield Strain, ε_y $(\%)$	0.256 ± 0.023	0.282 ± 0.017
Tensile Strain, ε_f $(\%)$	1.71 ± 0.115	3.5 ± 0.43
Tensile Energy Absorption, TEA (J/m^2)	59.7 ± 6.1	47.0 ± 6.0

Table 4.2: The Weibull parameters of 60 MD and CD specimens obtained by linear fit and MLE methods.

		m	σ_0 (MPa)
MD	Linear Fit	28.09	55.08
	MLE	23.31	55.16
CD	Linear Fit	23.85	20.37
	MLE	21.34	20.39

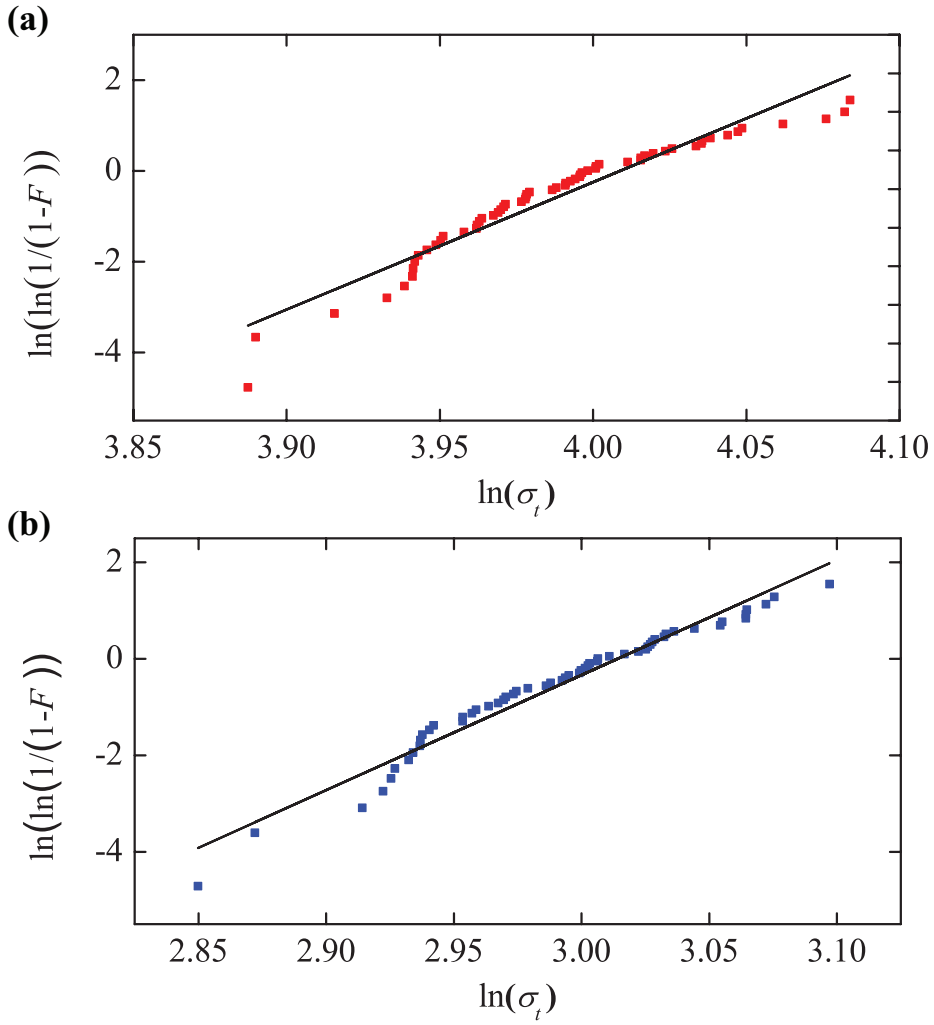

Figure 4.2: Weibull diagrams representing the scatter in tensile strengths of 60 specimens in (a)MD and (b)CD orientations.

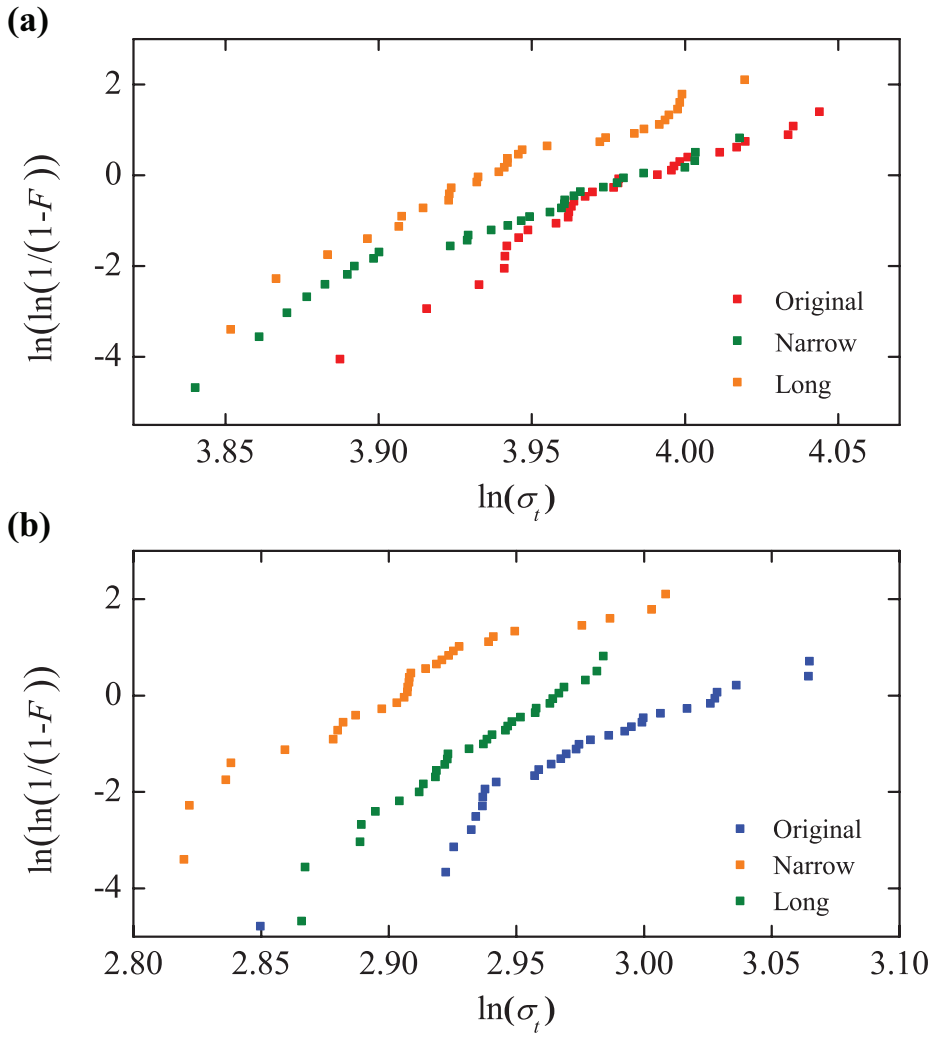

Figure 4.3: Shifted Weibull diagrams of three sets of (a)MD and (b)CD specimens of different sizes. The plots were shifted using Equation 4.1 and scaling factors of $\ln\frac{90}{50}$ and $\ln\frac{6.25}{12.5}$ for long and narrow specimens respectively.

and ν_{MD} and ν_{MD} are Poisson's ratios in MD and CD orientations respectively.

$$\frac{E_{MD}}{E_{CD}} = \frac{\nu_{MD}}{\nu_{CD}} \tag{4.2}$$

In this equation, Poisson's ratios as well as elastic moduli are treated as constants. However, as noted in the review article by Greaves, Greer, Lakes and Rouxel, the definition and interpretation of Poisson's ratio has evolved significantly since it was developed in the early 1800s for homogeneous, isotropic, linear elastic systems subjected to small strains [73]. It is generally recognized that Poisson's ratio provides useful insights into how the structure of the material influences the coupling between deformation in the loading and transverse directions from the earliest stages of (linear) elastic deformation through plastic deformation and failure. Moreover, the restrictions on the "allowable" values of Poisson's ratio do not apply to orthotropic materials such as the paper because the Poisson's ratio of anisotropic, elastic materials is theoretically unbounded [74–76]. Our experimental results showed that Poisson's ratio is not constant during elastic deformation of paper. The stress versus the full field average axial and transverse strain curves of three representative MD and CD specimens out of 60 are shown in Figures 4.4 and 4.5. At failure, axial strains were larger in the CD specimens, but transverse strains were larger in the MD specimens. The transverse strains at failure were 58 % and 16 % of the axial strains at failure in MD and CD specimens respectively. This difference in the strain ratio (transverse to axial strains) manifested that MD specimens were more easily contracted in the transverse direction than CD specimens due to fibers preferentially aligned in the MD.

Figure 4.4 and Figure 4.5 show that the strain ratio was not constant even in the linear elastic regime (Poisson's ratio, the negative of transverse to axial strain ratio) for all of the representative specimens. The strain ratio ranged from 0.25 to 0.75 among MD specimens and from 0.12 to 0.32 among CD specimens and eventually converged to 0.58 for MD and 0.18 for CD before the rupture. For some specimens, the strain ratio started at a higher

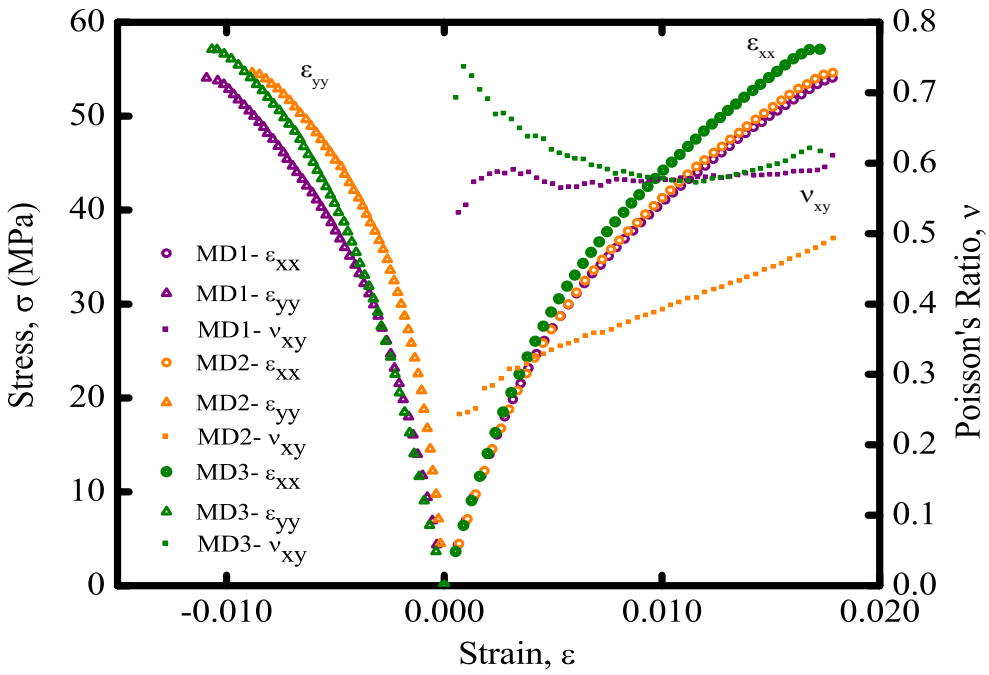

Figure 4.4: Stress versus full field averaged axial strains (circle) and full field averaged transverse strains (triangle) for three representative MD specimens. Poisson's ratio (square) versus full field averaged axial strain is plotted on the secondary vertical axis

value than the converged final value, and for some specimens it started at a lower value and peaked to the final value. So, at what value a specimen's strain ratio will start from was unpredictable and varied among specimens even those having the same orientation. Calculations of the average incremental Poisson's ratios did not provide additional insights into the system behavior. However, the final strain ratio values were predictable in that strain ratios of all MD specimens or all CD specimens converged to the single value. The evolution of strain ratio (Poisson's ratio) of paper in the elastic and plastic ranges has been previously observed by Schulgasser [13] and Szewczyk [77], yet its implication has not been appreciated until now. The dramatic change in Poisson's ratio has also been observed in other network materials like polyeurethane foam and ultra high molecular weight polyethylene which exhibit varying degrees of nonaffine deformations [73, 78]. In the following sections we will show that the variation in magnitude and evolution of the transverse strain ratio in paper was a direct result of nonaffine deformation of the heterogeneous fiber network.

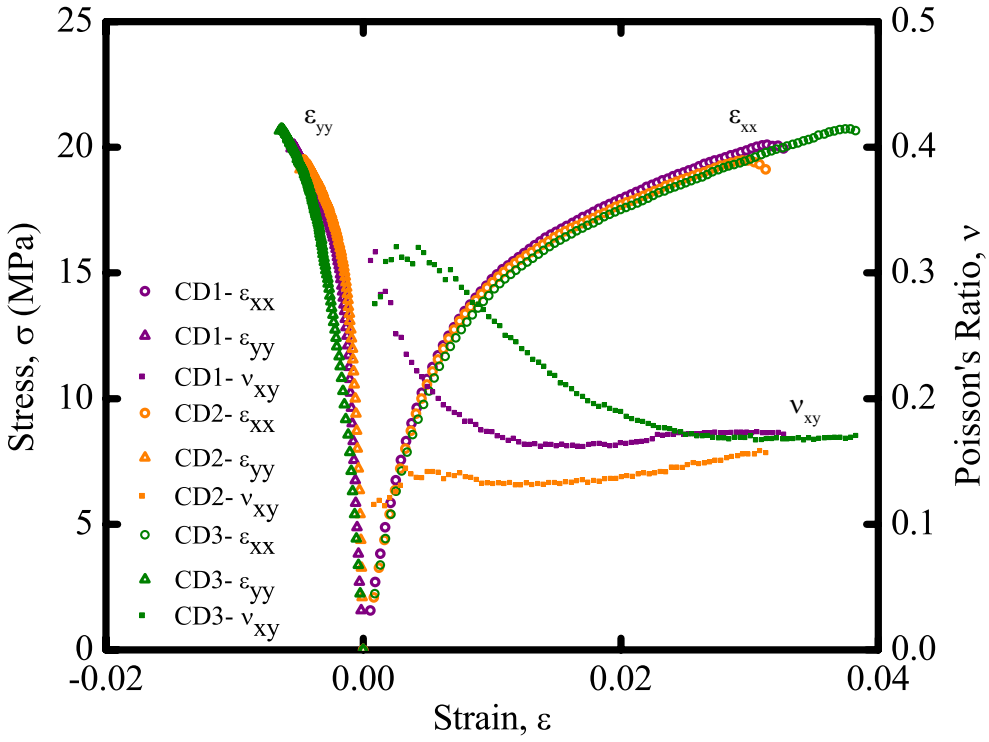

Figure 4.5: Stress versus full field averaged axial strains (circle) and full field averaged transverse strains (triangle) for three representative CD specimens. Poisson's ratio (square) versus full field averaged axial strain is plotted on the secondary vertical axis

4.2.2 Strain Maps

The spatial distribution and evolution of strains during deformation of both continuous and heterogeneous materials can be locally elevated because of variations in microstructure and the observation length scale.[1] Heterogeneous strain fields have been previously observed in paper, but the specimens were much *smaller* than those in our experiments [42] and were from isotropic, random handsheets [36, 42] with a low grammage (one third of the grammage in our paper), so their structure is quite different from the machine made paper used in packaging applications. The main focus of previous studies was to correlate the locally elevated strains with network characteristics such as low fiber density regions (i.e., low grammage or "formation"). Machine made papers have anisotropic, heterogeneous fiber networks that have (nominally) orthotropic properties. Many studies have focused on identifying a suitable specimen (representative volume) that allows for homogenization of the materials properties so that *effective* elastic properties can be characterized (i.e., the specimen size and loading conditions allow the Hill condition to be met [79–83]). The focus of the present study is quite different. Huet [81] and Hazanov and Huet [82, 83] noted that when the heterogeneities are large relative to the material form that it may not be possible to experimentally evaluate a large enough specimen to homogenize the system (and determine effective properties). In fact, such a specimen size may not exist. More importantly, specimens larger than the representative volume are not *necessary* [81, 82]). Sub-sized specimens provide important insight into the bounds for the effective elastic properties by establishing the apparent properties. The average axial strain fields from the displacement controlled, uniaxial tensile tests presented in the current work establish the

[1] High spatial resolution measurements of strain fields inevitably have variations on fine length scales that are, by necessity, a direct byproduct the material structure, properties, and loading conditions. The nomenclature used in the literature to describe the deviations of strain fields from the expected (usually continuum) descriptions has been an ongoing source of confusion. In this dissertation we called regions where the strains were elevated (or depressed) relative to the expected continuum values "hot spots". Moreover, we used the standard terminology "nonaffine" to emphasize that paper does not behave as a continuum because it is a porous, network structured material. We avoided using heterogeneity, strain localization and other similar terminology because they conflated a number of material structure, defect, and failure concepts (e.g., heterogeneous properties material, network structured materials, and necking).

upper bound for the effective modulus [81, 82]. Here we point out that, by extension, the average transverse strains fields can be used to establish an upper bound for the ratio of the Poisson's ratio (via the apparent modulus tensor). This approach is valid for the same reasons that a uniaxial tensile test fulfills the Hill condition- but the variability in the bounds on the Poisson's ratio should decrease as the specimen width increased (provided the system can be homogenized). Once again, we want to emphasize that the objective of this work is not to homogenize the system and establish effective elastic properties for paper. Instead, we are interested in how the spatial distribution of strains and the fiber network structure are related and evolve during uniaxial loading.

In Figures 4.6 and 4.7, axial and transverse strain maps of representative MD and CD specimens are presented. Note that 24 other specimens behaved similarly. The progression of strain maps from pre-yield (i.e., elastic) to pre-failure (i.e., elastic-plastic) are presented here, and four stages correspond to when the full field averaged axial strain was 5, 20, 45 and 95 percent of the failure strain, ε_f. Color scales of the strain maps were adjusted so that red, green, and blue colors each represent the high positive strain, zero strain, and high negative strain, respectively. All strains values presented here are linearly interpolated strains from real data points, and the measurement noise level was significantly lower than strains seen here (see section 2.3.2).

A significant amount of elevated strains were observed in the pre-yield stage (first strain map, $\varepsilon/\varepsilon_f$=0.05) and throughout the remainder of the tensile test. For both MD and CD specimens, in the first axial and transverse strain maps, there was a mix of small positive and negative locally elevated strains that were evenly distributed. As the specimen was further deformed, negative axial strains disappeared, and a only positive axial elevated strains remained to grow. Likewise, positive transverse strains disappeared and a range of negative transverse strains continued to grow. These small elevated negative axial strains and positive transverse strains observed in the early stage ($\varepsilon/\varepsilon_f$=0.05) and soon disappeared could have been caused by rearrangement of the fiber network such as straightening bent fibers

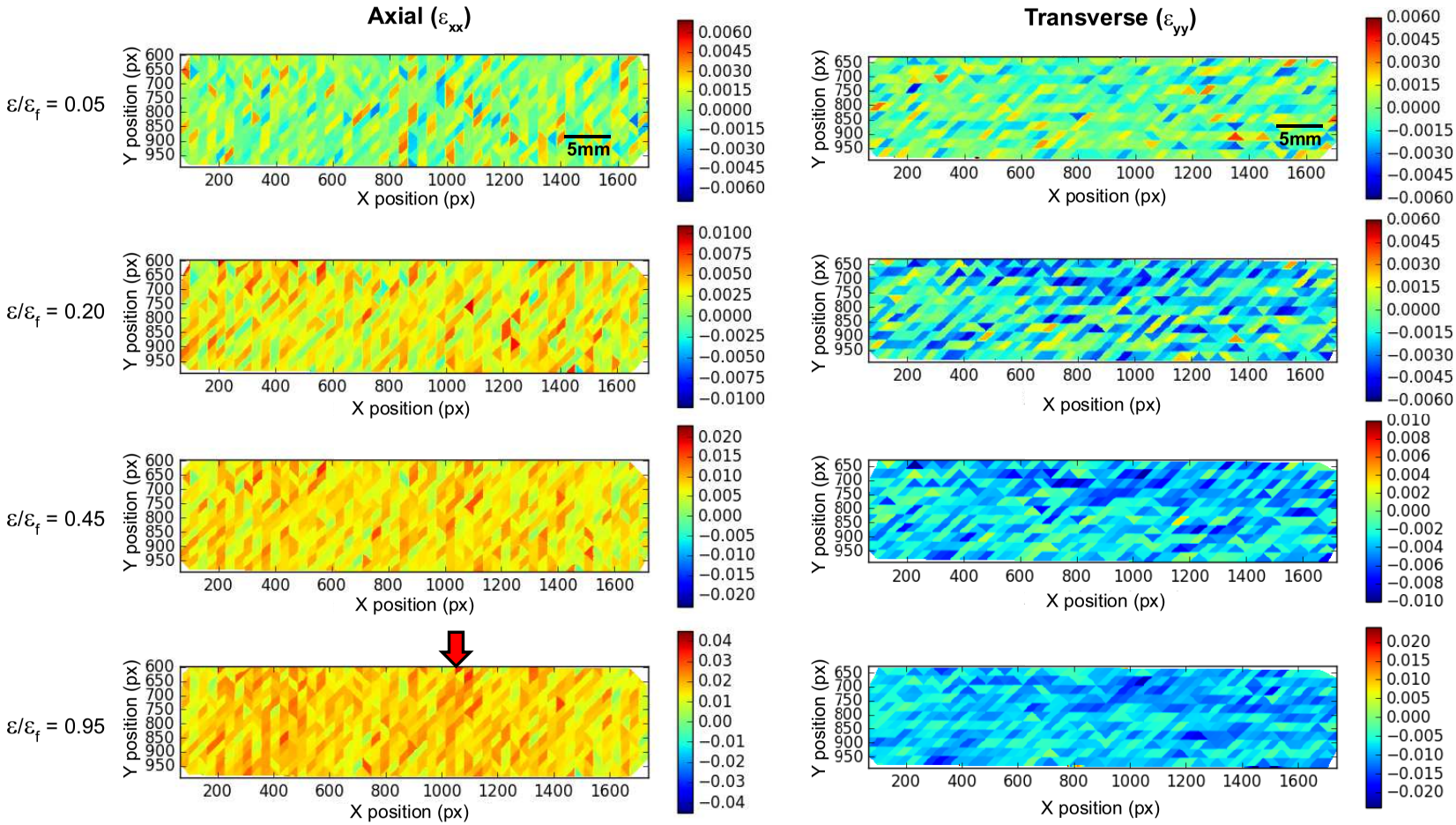

Figure 4.6: Progressions of axial (left column) and transverse (right column) strain maps of a representative MD specimen. Each row of strain maps corresponds to when the fraction of axial strain to failure is 0.05, 0.20, 0.45, and 0.95. Red arrow indicates the location failure originated, and the color bars show scale of strain.

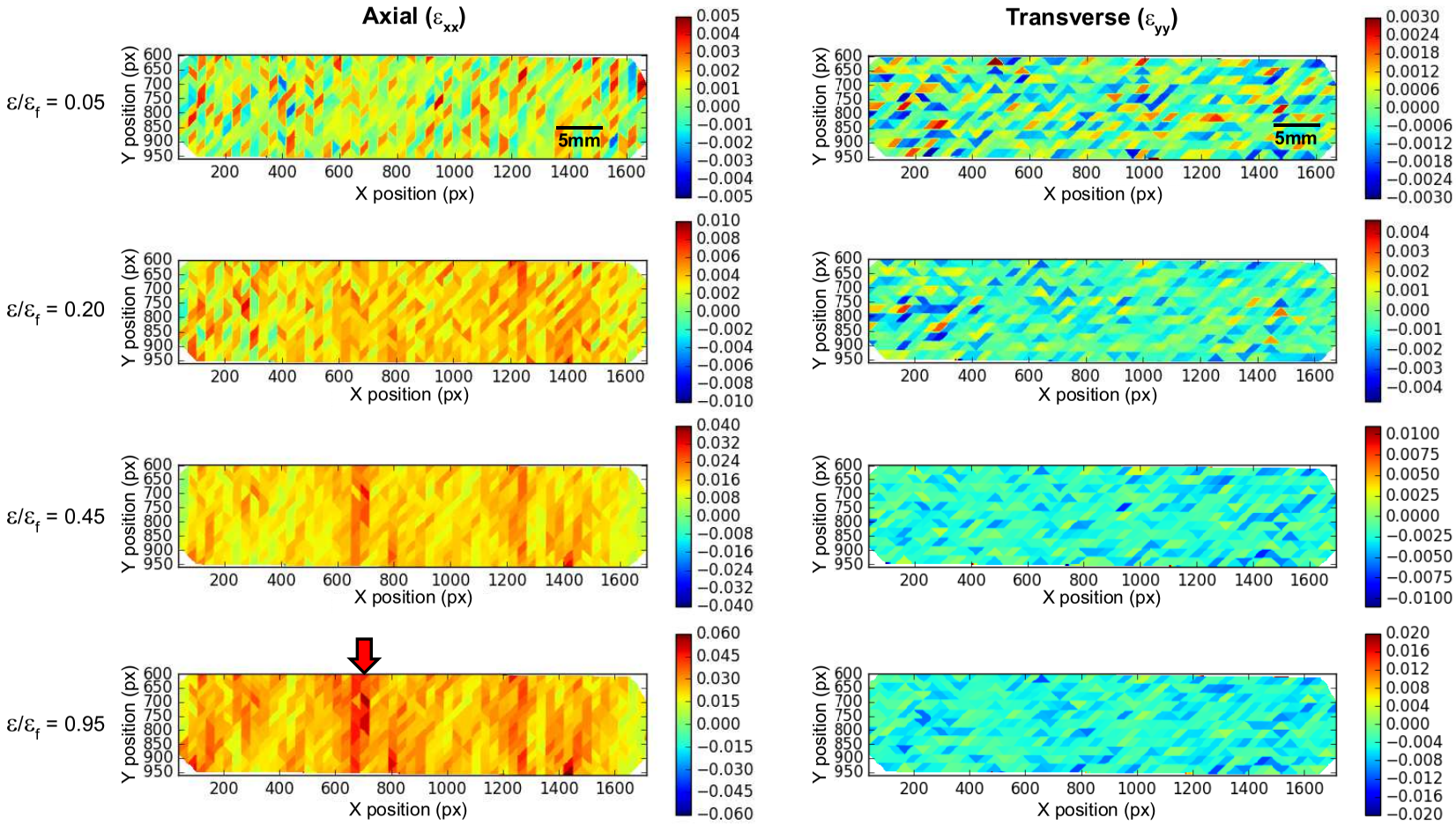

Figure 4.7: Progressions of axial (left column) and transverse (right column) strain maps of a representative CD specimen. Each row of strain maps corresponds to when the fraction of axial strain to failure is 0.05, 0.20, 0.45, and 0.95. Red arrow indicates the location failure originated, and the color bars show scale of strain.

and rotating tilted fibers.

Multiple regions with elevated strain were observed, and eventually failure initiated from one of these regions, indicated by a red arrow in the last axial strain maps. These high strain elevations could have been caused by different structural components in a fiber network from individual fibers to group of fiber regions. Generally, an area of the specimen can be highly strained when one side of the area has displaced significantly greater amount than the opposite side of the area. The fiber network was composed of overlapping fibers as well as pores, and the deformation around the pore was very prone to this kind of deformation. Therefore, the high strains can represent either actual highly deformed fiber or enlarged pores in the network. In the case of highly strained pores, a high strain did not necessarily correspond to a high stress because the elevated, localized strain region might not actually contain any load-bearing material at all. Next we will explore the quantitative links between the structures of the strain field and the fiber networks.

4.2.3 Characteristic Length Scales from Lineal Correlations

We observed local strain elevations and difference in strain evolution behavior between MD and CD specimens qualitatively in the previous section. While strain maps are qualitatively interesting, "strain field mining" techniques must be applied to isolate and quantify characteristics of strain elevation and distribution which can be related to material's structure or macroscale mechanical properties. To find characteristic length scales of elevated strain regions and distinguish different strain evolution behaviors between MD and CD specimens, the hot spot criteria was applied [48]. A threshold strain value, ε_{th}, was set as one standard deviation away from the mean strain value, and any local strain above this threshold value was treated as extreme value in the strain to separate high strain regions from the rest of the strain field. In principle a thresholding strain can be set to any value, but it is important to note that our strain threshold was not arbitrary. We showed in Figure 2.4 that the crosshead displacement, compliance corrected axial strains and the point

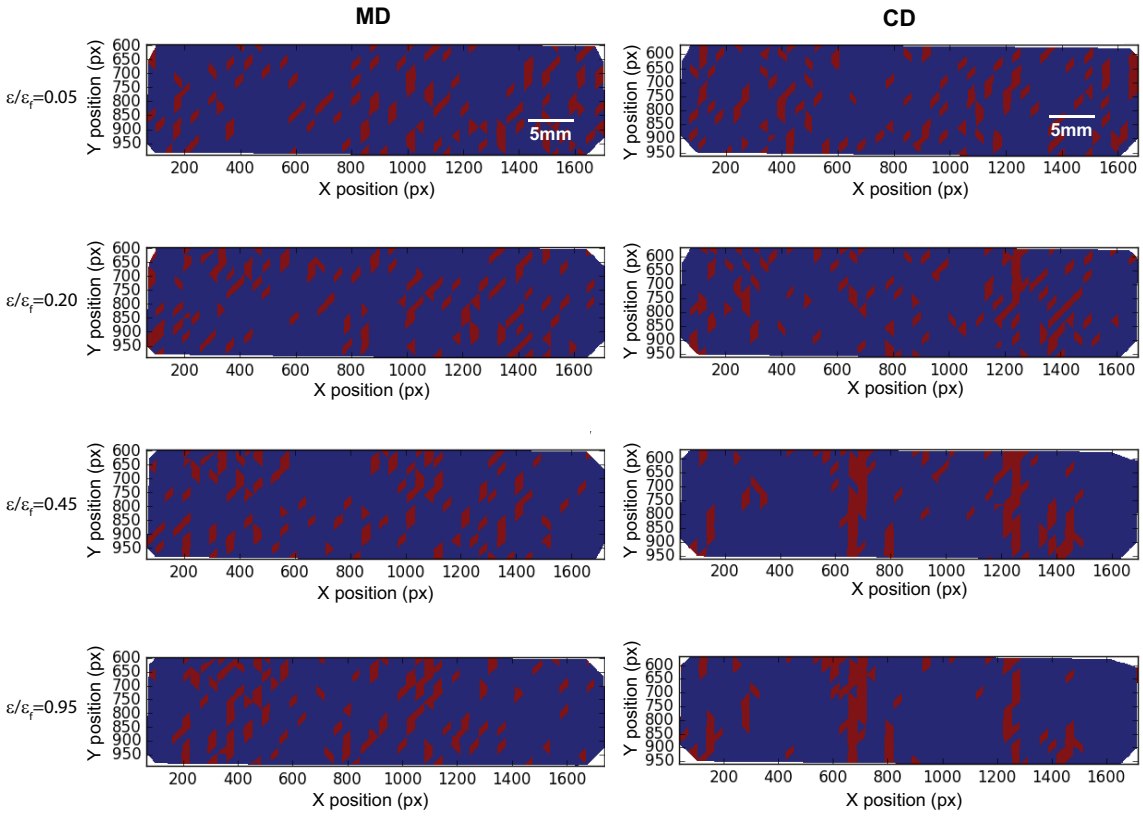

Figure 4.8: Thresholded axial strain maps of (a)MD and (b)CD specimens.

by point average of the full field axial strains are indistinguishable from one another, and characterize the general response of the specimens. As a result, the extremes in the strain field were significant because of their difference from the full field average axial strain and constituted the highest and lowest 15% of the strains in the field. We defined a "hot spot" as *contiguous regions* where the strain was above or below the threshold strain. We applied the detectability and contiguity criteria from [48]: the strain field hot spots contained at least three tracked points that were spaced greater than or equal to the minimum resolvable displacement (see section 2.3.2) divided by the threshold strain. Because we defined hot spots as contiguous, the mean value theorem guarantees that the strain between any two points contained within the hot spot region were above the threshold strain.

The thresholded binary images of the axial strain maps from Figures 4.6 and 4.7 are shown in Figure 4.8 (red(1) is the hot spot blue(0) is background). As we mentioned earlier, the formation of vertical bands of hot spot are only observed in the strain maps of the CD specimen. In order to quantitatively describe the difference in strain evolution behavior and extract characteristic length scales of hot spots from the thresholded strain maps of MD and CD specimens, we used a direction dependent function, lineal path correlation.

The lineal path probability distributions of 10 randomly selected specimens each in MD and CD orientations were analyzed, and we confirmed quantitatively that the characteristic length scales of hot spots in MD and CD specimens are different. The correlation analysis were done on pre-yield ($\varepsilon/\varepsilon_f$=0.05) and pre-failure ($\varepsilon/\varepsilon_f$=0.95) thresholded strain maps in both horizontal (θ=0) and vertical (θ=90) directions as shown in Figure 4.9 and Figure 4.10. Note that the horizontal direction is the loading direction, and the vertical direction is transverse direction.

$L00$ and $L11$ are the probabilities that a test line is completely inside the background (0) or hot spot (1) areas respectively. $L01$ is the probability that a test line segment of a specific length, R, crosses both components. As shown in Figure 4.9, two probability curves almost overlapped and were very similar for both thresholded strain maps of a MD specimen.

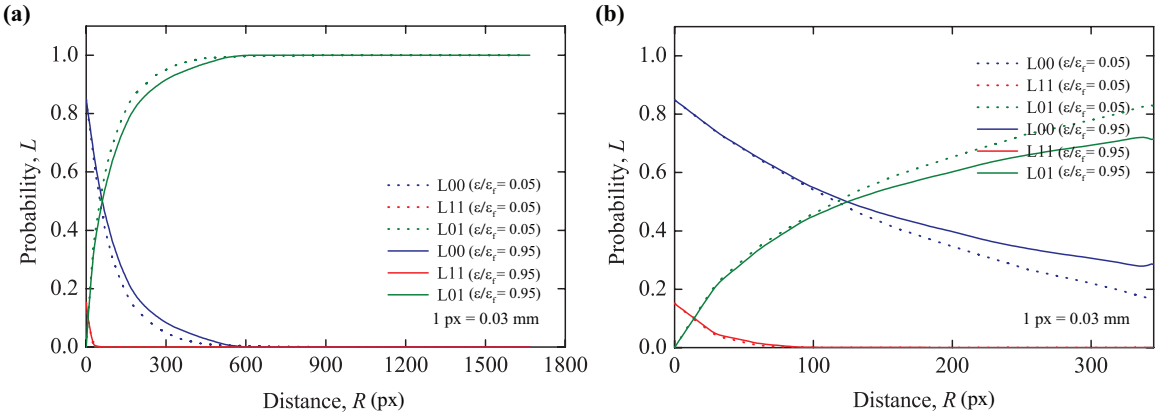

Figure 4.9: Line correlation results on thresholded MD strain maps analyzed in (a)horizontal and (b)vertical directions. The dotted lines are the results for the pre-yield ($\varepsilon/\varepsilon_f$=0.05) strain map and the solid lines are results for the strain map right before the failure ($\varepsilon/\varepsilon_f$=0.95).

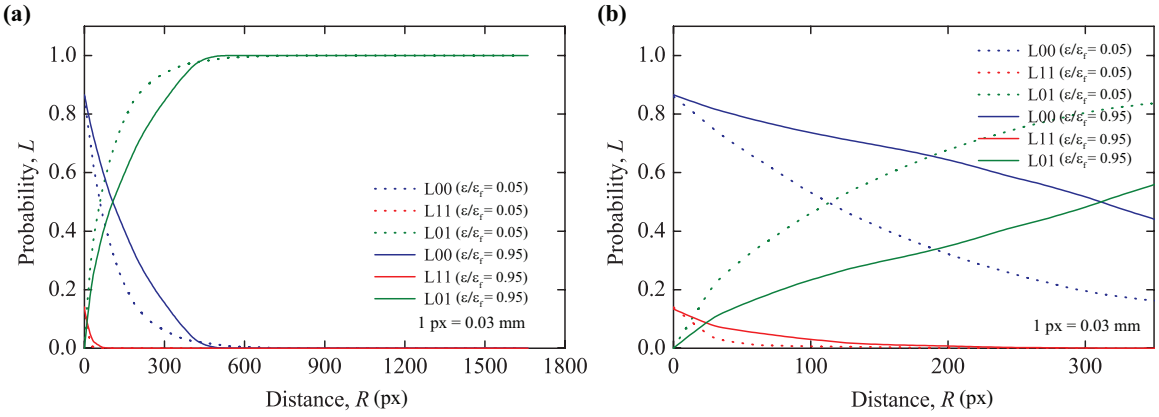

Figure 4.10: Line correlation results on thresholded CD strain maps analyzed in (a)horizontal and (b)vertical directions. The dotted lines are the results for the pre-yield ($\varepsilon/\varepsilon_f$=0.05) strain map and the solid lines are results for the strain map right before the failure ($\varepsilon/\varepsilon_f$=0.95).

Table 4.3: Averaged length scale values where lineal path probabilities approach zero

		MD		CD	
		Avg(px)	Avg(mm)	Avg(px)	Avg(mm)
P11 (0°)	Preyield	32	0.96	31	0.94
	Prefailure	33	1.01	63	1.90
P11 (90°)	Preyield	77	2.31	93	2.80
	Prefailure	91	2.73	171	5.13

The distance, R, where the $L00$ and $L11$ probabilities approached 0.01 was recorded as the characteristic length scale of the region of interest (hot spots or background) in the direction of the test line. In the horizontal direction (θ=0), L11 probability curves approached 0.01 around R of 30 pixels (0.9 mm) for both strain maps at two different stages. In the vertical direction (θ=90), L11 probability curves approached zero at 71 (2.13 mm) and 82 pixels (2.46 mm). These length (R) values represented the characteristic length scales of the hot spots; the hot spots were anisotropic and were elongated in the vertical direction. The overall trend of the L00, L11, and L01 probability curves did not change significantly over the course of tensile loading of MD specimens.

In contrast to the MD specimens, CD specimens displayed a different trend in the hot spot evolution. It was apparent that the thresholded strain maps changed significantly from beginning to end of the tensile test as shown in the second column of Figure 4.8. This difference was quantitatively confirmed with the lineal probability analysis result in Figure 4.10. The L00, L11, and L01 probability curves were significantly different between strain maps of early and late stages. The characteristic length scale of hot spots were 33 pixels (0.99 mm) and 132 pixels (3.96 mm) in horizontal (θ=0) and vertical (θ=90) directions for the early stage ($\varepsilon/\varepsilon_f$=0.05) and 66 pixels (1.98 mm) and 225 pixels (6.75 mm) for the late stage ($\varepsilon/\varepsilon_f$=0.95). The hot spot size nearly doubled in both horizontal and vertical directions from the beginning to the end of a tensile loading. This result is very different from result for MD specimens where the hot spot size did not increase over the course of

tensile loading. Thus, depending on the orientation of the paper, not only the macroscopic tensile properties (4.1) but also strain evolution characteristics are determined.

The characteristic length scales of hot spots averaged among 10 specimens are tabulated in Table 4.3. During elastic deformation ($\varepsilon/\varepsilon_f$=0.05) the average size of hot spot was 0.96 mm by 2.31 mm for MD specimens and 0.94 mm by 2.80 mm for CD specimens. The size of hot spots in MD and CD specimens were similar during this early stage of the tensile tests. Just before fracture ($\varepsilon/\varepsilon_f$=0.95) the average size of hot spots became 1.01 mm by 2.73 mm for MD specimens and 1.90 mm by 5.13 mm for CD specimens. The hot spots stayed small in MD specimens but nearly doubled in CD specimens. We speculated that the difference in the evolution behavior might be related to structural anisotropy in paper.

The spatial variation in the density of fibers in paper is generally called formation. The agglomerates of fibers which make up the higher density regions of the formation are called flocs. However, it is difficult to describe the characteristics of formation because the concept of this size of a floc and the lower density regions between them are not well defined in a heterogeneous material. One might expect that measuring the transmission of light through a paper would be an effective way to characterize the density spatial distribution (formation) of paper. While it is easy to see bright and dark areas in a backlit (transmitted light) image, they do *not* directly correlate with local density in most machine made papers because of how visible light scatters off of the fibers and fillers [43]. In spite of this limitation, it is still possible to estimate the characteristic length scales of the paper formation using transmitted light images. As detailed in section 2.5, we can quantify the length scales of the formation if we evaluate large areas and use a fast Fourier transformation to isolate the floc and interfloc regions [59–61]. Using this approach, we determined that the characteristic size of flocs in the paper were 2.99 mm in MD and 2.65 mm in CD. The characteristic size of the inter-floc regions was 2.83 mm in MD and 2.84 mm in CD. Since we found that the shape of flocs and inter-flocs were nearly isotropic, it did not directly correlate with the shape of anisotropic hot spots observed. However, we know that

the internal structure of flocs are anisotropic due to preferential fiber alignment– regardless of floc shape. Moreover, not all flocs will have the same fiber distribution. What we can state is that the average fiber areal densities were similar in flocs. Since hot spot sizes of both MD and CD specimens at the early stage of tensile test were smaller than characteristic floc sizes, we believe that other structural features of the network were responsible for the scale and evolution of strain field hot spots in paper.

4.2.4 Deformation Maps

The hot spots in the strain maps were readily visualized and quantified, but they are not the only approach to visualize the deformation of porous, heterogeneous materials. We found that deformation maps can directly show the rigid body motion and overall deforming pattern of the paper, and can be used to determine the degree of nonaffine deformation in paper. Deformation maps are often disregarded because strain maps, (calculated from deformations), contain all the relevant information for continuum materials. Deformation maps can be particularly useful for examining both continuum and network materials that contain discontinuities which can give rise to large apparent strains. It also provides the ultimate verification for a continuum model by showing that the final position and shape of a body can be predicted from the boundary and loading conditions and the constitutive relationship between stress and strain. Here, by comparing experimentally obtained deformation maps with ideal, affine ones, we found that there is significant nonaffine deformation in paper in the *transverse* direction for both MD and CD specimens during uniaxial tensile loading.

Figure 4.11 shows the expected affine (continuum) behavior based on full field average (or compliance corrected) axial and transverse strains data from one of the representative MD stress-strain curves. In the affine deformation fields, it was possible to predict the deformation values at any location inside the specimen by using the far field (imposed) strain and the constitutive relationship. Thus, we can use the degree to which a specimen follows this ideal behavior as an indicator of the degree of nonaffine deformation. This concept of

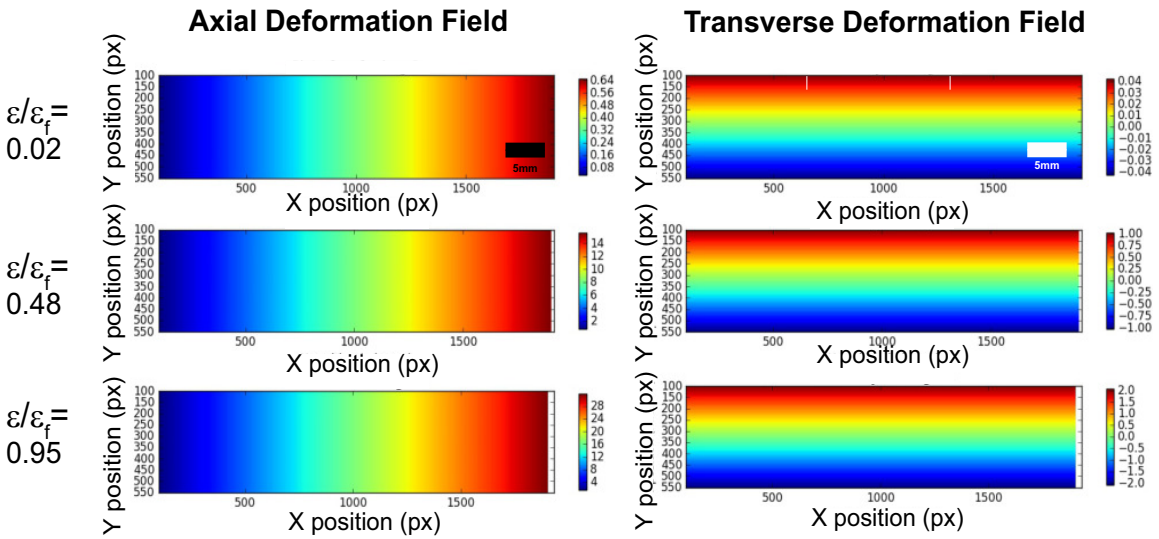

Figure 4.11: Progression of affine deformation fields of a homogeneous continuum specimen in axial (left column) and transverse (right column) directions. Each row of deformation fields corresponds to when the fraction of axial strain to failure is 0.02, 0.48, and 0.95.

nonaffinity has been used to quantify deviations from an affine, ideal scenario [84–86]. In our graphical representation in Figure 4.11 the left edge of the specimen is stationary and the right edge is axially loaded horizontally (rigid body motion from the load frame was measured directly at the fixed grip from images of the specimen during the tensile test and was subtracted accordingly). If a specimen were to deform in an ideal, affine manner (i.e. as a homogeneous continuum) in uniaxial tension, then both axial and transverse *strain* fields would be uniform over entire specimen at large enough length scales. In constrast, the *deformation* fields would not be uniform. The magnitude of axial deformation increases proportionally from the stationary end of the specimen. Therefore, the axial deformation fields have a linear gradient from a stationary boundary condition at the left edge of the specimen to the imposed crosshead deformation vector at the other end. The transverse deformation fields also have a linear gradient from a negative value to a positive value of the same magnitude. However, the axial centerline of the specimen has a zero deformation due to the material deforming inward uniformly. Thus, the magnitude of transverse deformations are symmetric along the horizontal centerline and increase proportionally with the

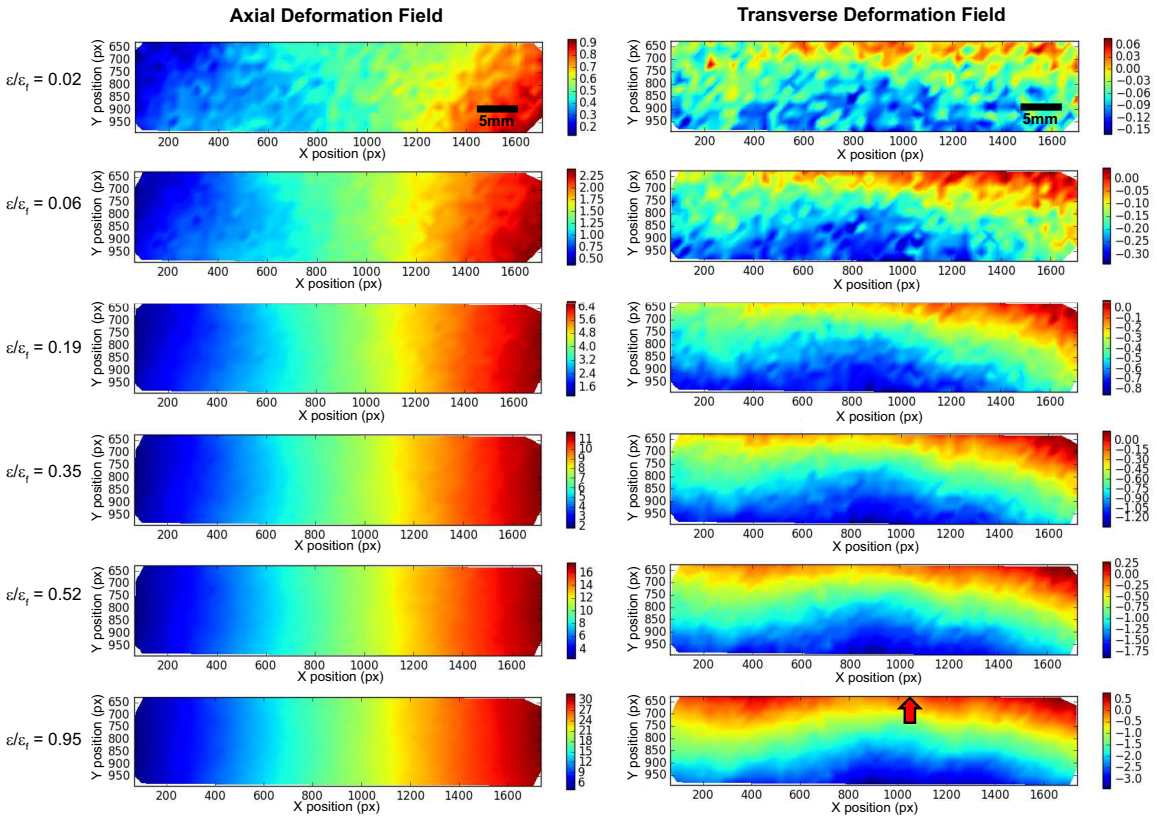

Figure 4.12: Progression of deformation fields of a representative MD specimen in axial (left column) and transverse (right column) directions. Each row of deformation fields corresponds to when the fraction of axial strain to failure is 0.02, 0.06, 0.19, 0.35, 0.52, and 0.95. Red arrow indicates the location failure originated, and the color bars show scale of displacement in pixel.

distance from that centerline.

Experimental deformation fields of the representative MD and CD specimens (same ones from Figs. 4.6, 4.7) are shown in Figure 4.12 and Figure 4.13. During the earliest stages of each experiment, the *axial* deformation fields of both MD and CD specimens deviated slightly from the ideal behavior. However, the distribution quickly became a linear gradient as the specimens were loaded, just like the affine distribution. On the other hand, we observe that the experimental *transverse* deformation fields of both MD and CD specimens were distinctly different from the affine ones. The transverse contraction was not symmetric along the horizontal centerline. As shown in Figure 4.11, the transverse deformation field of an ideal specimen had zero transverse deformation along the centerline, and

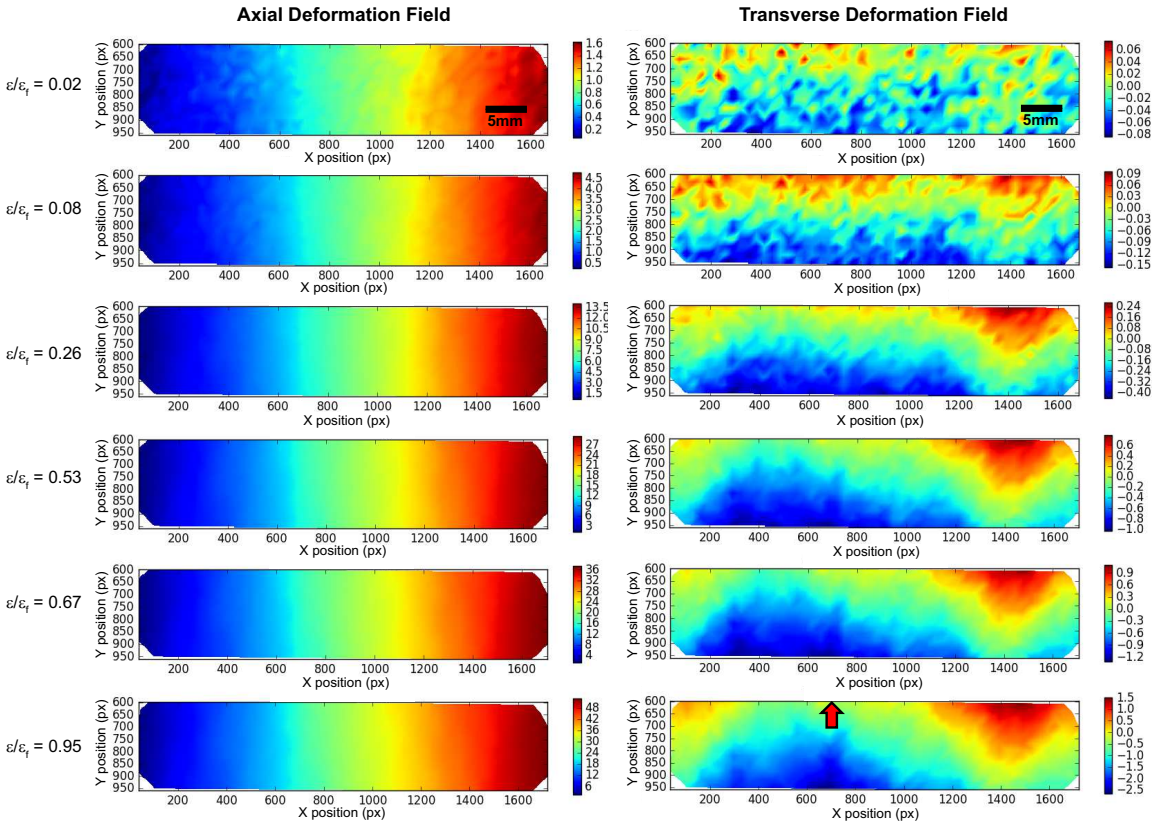

Figure 4.13: Progression of deformation fields of a representative CD specimen in axial (left column) and transverse (right column) directions. Each row of deformation fields corresponds to when the fraction of axial strain to failure is 0.02, 0.08, 0.26, 0.53, and 0.95. Red arrow indicates the location failure originated, and the color bars show scale of displacement in pixel.

linearly increasing deformation away from the centerline. In the experimental deformation maps (Figs. 4.12, 4.13), the transverse deformations were not symmetric along a horizontal centerline, but the lines of symmetry appeared as curves or waves running from the left end to the right end of the specimens. The undulation in the line was mild in the MD specimens and severe in the CD specimens. The difference in the degree nonaffine deformation in axial and transverse directions were not apparent in the strain fields, but the deviation from the affine case is clearly shown in the transverse deformation fields. Note that these undulations were not experimental artifacts. Our imaging system optics allowed us to confirm planar deformations (wrinkling due to misalignment and other experimental artifacts were readily observed), and our experiments were conducted using precisely tuned, closed loop system with high frequency data acquisition [note: the machine used in our experiments is not a conventional screw drive load frame- it is a dedicated low force, small displacement (20 nm resolution) system that was routinely used to conduct closed loop, force and displacement controlled tests on small, flexible specimens]. Also, feature tracking noise level during DIC was small and unbiased over entire field of specimen (see section 2.3.2). We captured full field images of the specimens that included the grips, and we directly measured rigid body motion of the grips and specimen (which were subtracted), and verified precise specimen alignment for each test. There was no evidence that there were grip, alignment, wrinkling, or other issues in either the displacement or strain fields. Thus, nonaffine transverse deformation behavior observed is noteworthy given the reproducible axial stress-strain curves (Fig. 4.1).

It is interesting to see that despite the structural and mechanical anisotropy in the paper, the deformations were nearly affine in axial direction and nonaffine in transverse direction for both MD and CD specimens. The non-uniform contraction in the transverse deformation cannot be explained by the fact that paper dried under restraint contains some kind of residual stress. It was previously found that the magnitudes of the residual stresses in paper are below the yield stress [87]. Therefore, the residual stress will not be large enough to

be translated in the transverse deformation fields after the yield point. Only the first two transverse deformation maps in Figure 4.12 and Figure 4.13 were in the elastic regime, and the undulations were still prominent in the post-elastic fields. Thus, we can conclude that the residual stress was not responsible for such behavior. Instead, we speculate that, in the axial loading, stress was transferred along the fibers that were nearly oriented in the axial direction, and those fibers were extensively stretching. Fibers that were not oriented in the axial direction can bend and/or rotate during the axial loading, which contributed to the compliance. Thus, the ratio of fibers oriented in the axial direction and transverse directions resulted in the mechanical anisotropy of machine made papers. The nonaffine transverse deformations were likely because of the motions of fibers that were not oriented in the axial direction, so the nonaffinity was caused by those fibers rotating and bending with very little stretching.

The transverse deformation fields not only showed nonaffine deformation of the fiber network but also provided important insights into which regions in the specimen were associated with fracture. Red arrows in Figure 4.12 and Figure 4.13 point to the fracture initiation sites. We observed that the fracture initiated from the opposite end of the region where the largest (magnitude) transverse displacement was present. For example, in Figure 4.12, we determined where the transverse displacement magnitude was the highest when the overall strain was still relatively small. Here, the highest displaced region was around position (x=1000, y=950), and we find that the failure originated at the opposite end at position (x=1000, y=650). This is an interesting finding because determining fracture initiation site among many elevated strain regions is difficult especially early on in. Since undulations in the transverse deformation were more severe in CD specimens, predicting where the specimen will fail by examining deformation fields was generally easier for the CD specimens. Thus, we can infer that the failure location is related to fiber network features that are important to the transverse deformation behavior. Characterizing the local structure of paper in these areas that contracts the most based on the strain hot spots and

undulations is a subject of our ongoing research and will be useful for identifying critical structural features that govern the deformation behavior of paper.

4.2.5 Degree of Nonaffinity

Various measures of nonaffinity have been used previously such as strain based [86], displacement based [85], and angle based [84] measures. Depending on the subject of comparison and loading conditions, one metric can be more effective than other ones in describing the level of nonaffinity in the system. We chose to use a deformation-based metric instead of strain-based one because we measured motion directly in our experiments. Moreover, we chose to normalize the metric to allow comparisons between axial and transverse directions and between MD and CD specimens. It is important to note that a strain based measurement cannot be used here with the normalization scheme because the metric is too sensitive to errors when local strains are very small during the early stages of tensile test. Thus, the deformation based degree of nonaffinity used in this work is defined by the magnitude of deviation from affine deformation normalized by magnitude of affine deformations as shown in equation 4.3.

$$D = < \frac{|u - u_{aff}|}{< |u_{aff}| >} > \tag{4.3}$$

The difference between the actual deformations, u, and corresponding affine deformations, u_{aff}, represents the magnitude of deviation from affine deformation behavior. Here, u_{aff} values for each grid points were easily calculated from given far-field strain and position values. Furthermore, we normalized the difference with the mean of the absolute u_{aff} so that it can be compared across different specimens and orientations. The normalization was done with an average u_{aff} rather than local u_{aff} because we wanted to equally weigh the deviation effect from all grid points regardless of their position. Note that $< |u_{aff}| >$ values are specific to each data points on Figure 4.14 because full-field deformation values were varying over the course of tensile loading, among specimens, and between axial and

transverse directions. This measure, D, is a scalar property, so it was calculated in axial and transverse directions separately. If deformation is completely affine, D would be 0.

In Figure 4.14, degree of nonaffinity, D, is plotted against axial strain ratio to failure, $\varepsilon/\varepsilon_f$, for 8 representative MD and CD specimens (one of the 8 shown in Figures 4.12 and 4.13). The degree of nonaffinity was significantly greater in transverse direction than in axial direction for both MD and CD specimens. In the axial direction, D stayed below 0.5 for most of specimens throughout the tensile test, so we can say that specimens deform nearly affinely in the axial direction. However, D in the transverse direction varied more from specimen to specimen, and ranged from 0.5 to 3 for MD and 1 to 3.5 for CD. but there was no clear trend for the CD specimens. The direction dependent D values were consistent with the results seen in the deformation maps (Figs. 4.12, 4.13). In the axial direction, both MD and CD specimens were relatively well behaved and did not deviate much from the affine behavior. On the other hand, deformation in the transverse direction was more heterogeneous and deviated significantly from the corresponding local affine behavior.

D in the transverse direction prior to the plastic deformation (yield) points (where on average $\varepsilon/\varepsilon_f$ was 0.15 for MD and 0.08 for CD) increased for some specimens and decreased for others irrespective of the specimen orientation. This means that before yielding, both MD and CD specimens behaved indistinguishably, which is the same observation we made in the thresholded strain maps (Fig.4.8) and deformation maps (Figs. 4.12, 4.13). At the early stage of the deformation, MD and CD specimens had similar transverse deformation fields, and the behavior was random among the specimens even in the same orientation. Right after the yield point ($\varepsilon_y/\varepsilon_f$), D in transverse direction decreased for all of the MD specimens and increased for the seven out of eight CD specimens. Again, we speculate that this difference between MD and CD specimens was resulted from the difference in the amount of fibers oriented in the axial direction. MD specimens have high ratio of axially oriented fibers, so when the network is loaded, most of fibers are stretching in the axial

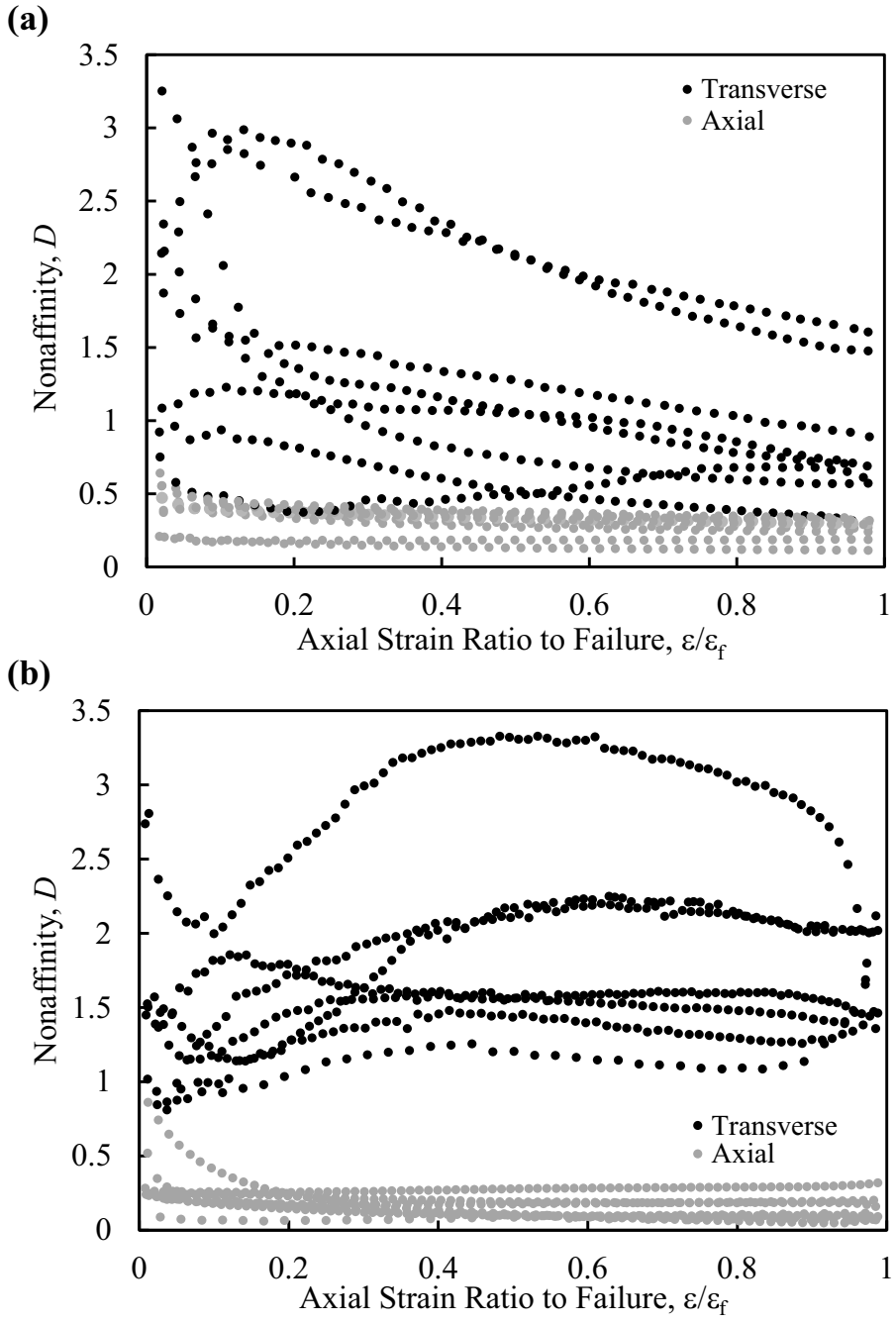

Figure 4.14: Quantitative measurement of nonaffinity, *D*, in axial (gray) and transverse (black) directions for (a)MD and (b)CD specimens

direction. However, CD specimens have high amount of fibers oriented in the transverse directions, and these fibers are not directly loaded but pulled in by the network, so the motion is not directly controlled by the axial loading.

As shown in Figure 4.14, the degree of nonaffinity, D, varied among different specimens and also evolved as the specimens were strained. Therefore, a single average value cannot be used to represent the degree of nonaffinity in MD or CD specimens. Instead we opted to compare the average nonaffinity ratio, $D_{transverse}/D_{axial}$, at an axial to failure strain ratio value of 0.5. This ratio represents how much more significant the degree of nonaffinity is in the transverse direction than it is in the axial direction. This ratio was 4.5 for MD specimens and 14.1 for CD specimens. These values, without any doubt, show that nonaffine deformation is more significant in the transverse direction than in axial. Moreover, the degree of nonaffinity was three times more pronounced in the CD specimens than in MD specimens. This quantitative result is consistent with the observations made in the deformation maps (Figures 4.12 and 4.13) where we saw significant nonaffine behavior in the transverse direction in the CD specimens.

We evaluated D on a series of proprietary, commercial linerboards that were produced with different material and processing variables. As shown in inset plots of Figure 4.15, the stress-strain curves of two types of linerboards are indistinguishable. However, when we calculated the degree of nonaffinity, we were able to see that the transverse D were very different between two types of linerboards. Specifically, the CD transverse degree of nonaffinity (Fig. 4.15b) shows that the type 4 paper has higher nonaffinity and more variable response than the type 2 paper. This means that their fiber networks are quite different even though their stress-strain responses were the same. Therefore, strain field mining and degree of nonaffinity metric can potentially quantify how processing variables change the fiber network in ways that directly impact mechanical performance.

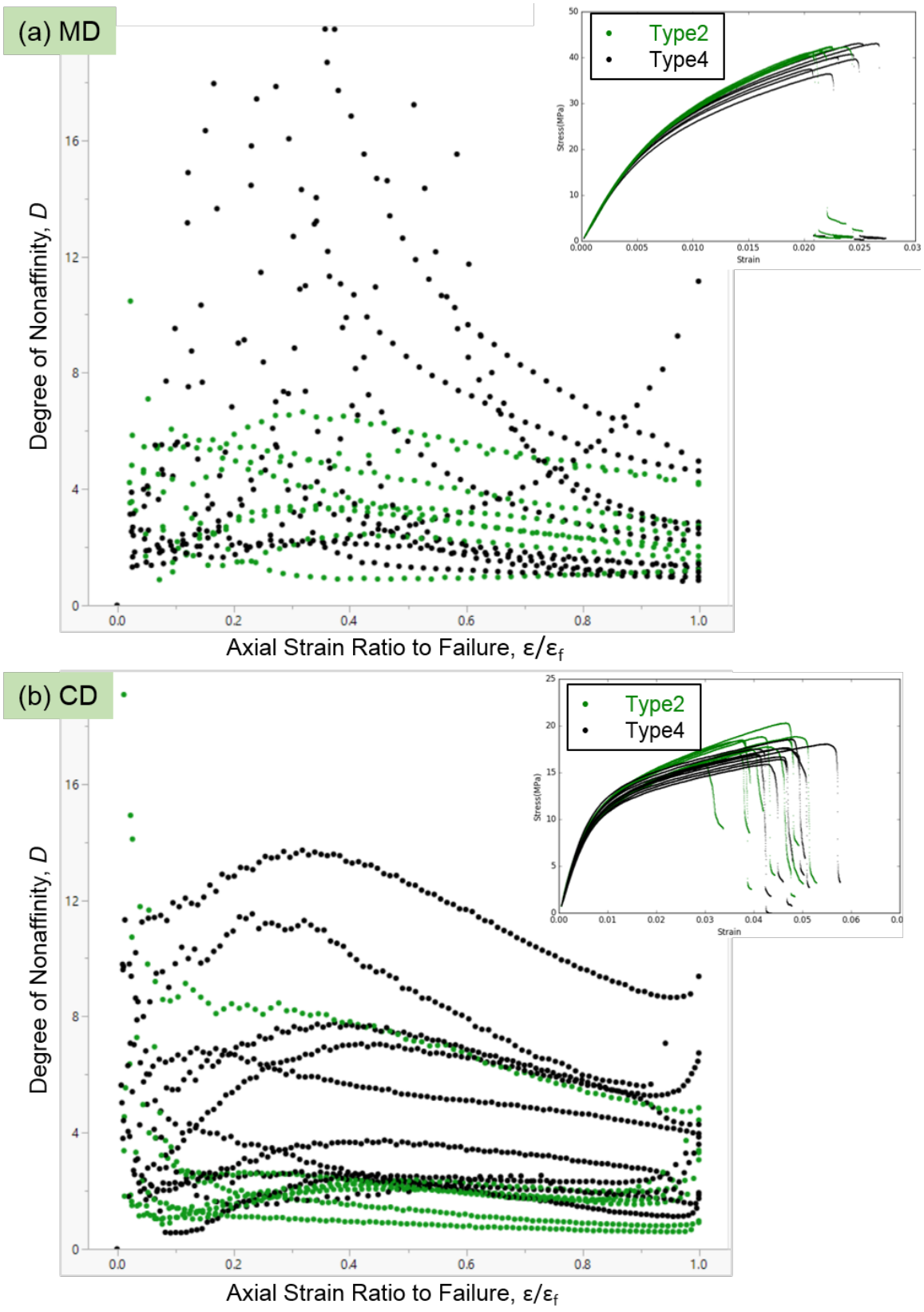

Figure 4.15: Quantitative measurement of the transverse nonaffinity, D, of two types of commercial linerboards with the same macroscopic stress-strain response (inset figures).

4.3 Conclusions

The tensile deformation of paper is nonaffine, especially in the transverse direction, and interplay between two orthogonal directions (MD and CD) is a critical feature of underlying failure mechanism in its fiber network. This behavior manifests itself as a varying Poisson's ratio that is a byproduct of a specimen-specimen network topography. For example, failure locations are identified in axial strain maps as well as transverse deformation maps. The nonaffine deformations are significant even when the specimen is larger than the size of the fiber agglomerates (flocs), and occur for all orientations of the orthotropic sheet. We found that strain hot spots are initally smaller than the size of flocs but becomes larger than flocs only in CD specimens. Also, the characteristic shape of hot spots are elongated where the shape of flocs are found to be isotropic. While the axial deformations are essentially affine (nonaffinity metric, D, below 0.5), the transverse deformations are not (nonaffinity metric, D, from 0.5 to 3.5). The anisotropic, nonaffine behavior is a result of the fiber orientation relative to the loading direction: The tensile deformations are controlled by stretching of axially oriented fibers, and the transverse deformations are from bending and rotation of fibers that are inclined to the loading direction. The ratio of the number of axially-oriented to inclined fibers is different for MD and CD specimens due to processing-induced network anisotropy: CD specimens have about 3 times higher degree of nonaffinity in the transverse direction than MD specimens. Moreover, the nonaffine deformations in the transverse direction are an essential feature of the tensile deformation and failure mechanisms of the fiber network in paper. Direct relationships between the network structure and the nonaffine, transverse deformations (strains) will probably require a complete characterization of the fiber network topography.

CHAPTER 5
FATIGUE DAMAGE ACCUMULATION IN PAPER

This chapter will explores paper's fatigue degradation mechanism that is unique to tensile cyclic loading conditions. The extent of fatigue damage accumulation was determined with thresholding strain field mining analysis. Therefore, the difficulty in defining cracks in fibrous network of paper was overcome by extracting the size of cracks from the strain fields. Paper specimens in the CD orientation were fractured under monotonically increasing, constant, and sinusoidally varying stresses to compare effects of tensile, creep, and fatigue damages on paper. It was found that fatigue damage can accumulate quickly via a fiber fracture mechanism, while additional damage accumulation occurs by the failure of inter-fiber bonds. Moreover, the synergistic iterations between creep and fatigue damage accumulation mechanisms which is key for extending fatigue life of paper was also discovered.

5.1 Introduction

Although tensile overload and creep deformation of paper have been thoroughly studied in the past, cyclic loading in paper was only associated with repeatedly folding a paper back and forth on itself until a well-defined tear is created. Because different modes of loading, such as tension and bending (folding), are often associated with different deformation, degradation, and failure mechanisms, we must also understand how tensile cyclic stress condition damages the paper. Here we detail a unique tensile cyclic (fatigue) damage accumulation mechanism that can degrade the durability and performance of paper-based packaging and shipping boxes that are repeatedly stressed.

The mechanisms that control the deformation, degradation, and failure of wood fiber-based paper and packaging materials depend on how the stresses are applied (Fig. 5.2).

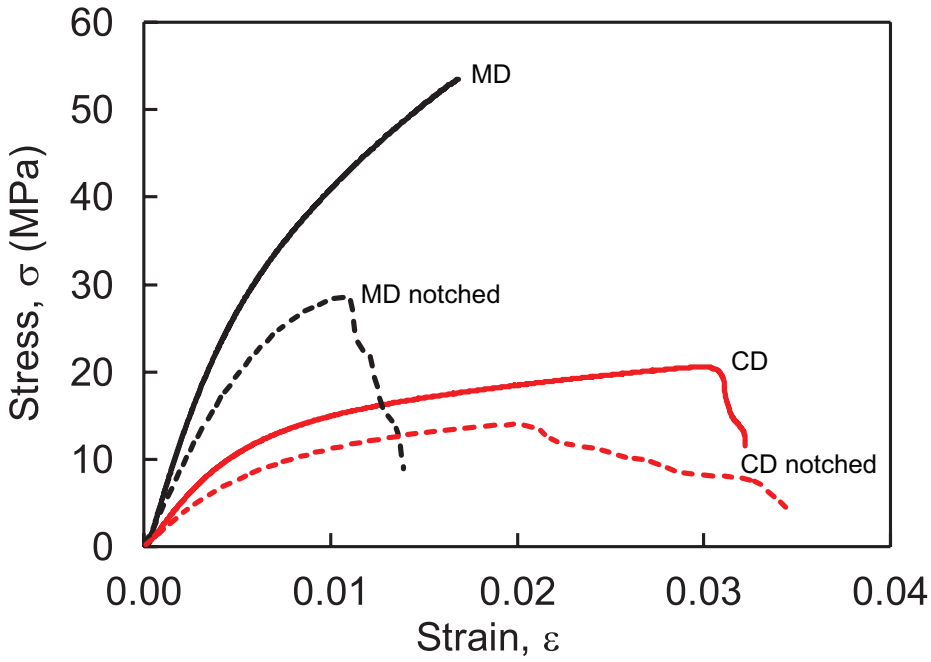

Figure 5.1: The uniaxial tensile deformation behavior of copy paper was measured in the machine direction (MD) and cross direction (CD). Representative data for plain and notched ($\frac{a}{w} = 0.27$) tensile specimens are shown. The addition of a notch reduced the stiffness and strength of the paper (dashed lines). The error bars were within the line width.

When paper is pulled to failure in tension, the fiber network deforms (first elastically, then plastically) and fibers move relative to one another [4, 5]. This behavior cannot continue indefinitely- eventually the inter-fiber bonds fail and the paper breaks. The resulting fracture surfaces are typically hairy (Fig. 5.3a), providing clear evidence of inter-fiber bond failure and the fiber pull-out fracture mechanism during tensile failure [2, 5]. Similarly, the fracture surfaces of folded (or creased) papers that are then torn show some fiber damage (typically crushing and buckling)[88], but are also hairy because they fail by a similar tensile failure mechanism. A constant load can cause time-dependent damage via processes known as creep [89], again causing fracture surfaces that are hairy in appearance (Fig. 5.3e) because of a time-dependent inter-fiber bond failure and fiber pull-out fracture mechanism [89]. We also know that repeated loading and unloading of paper can create cycle-dependent (as opposed to time-dependent) damage, but in this case it has not been clear if the mechanisms are distinct from the ones that control conventional tensile and

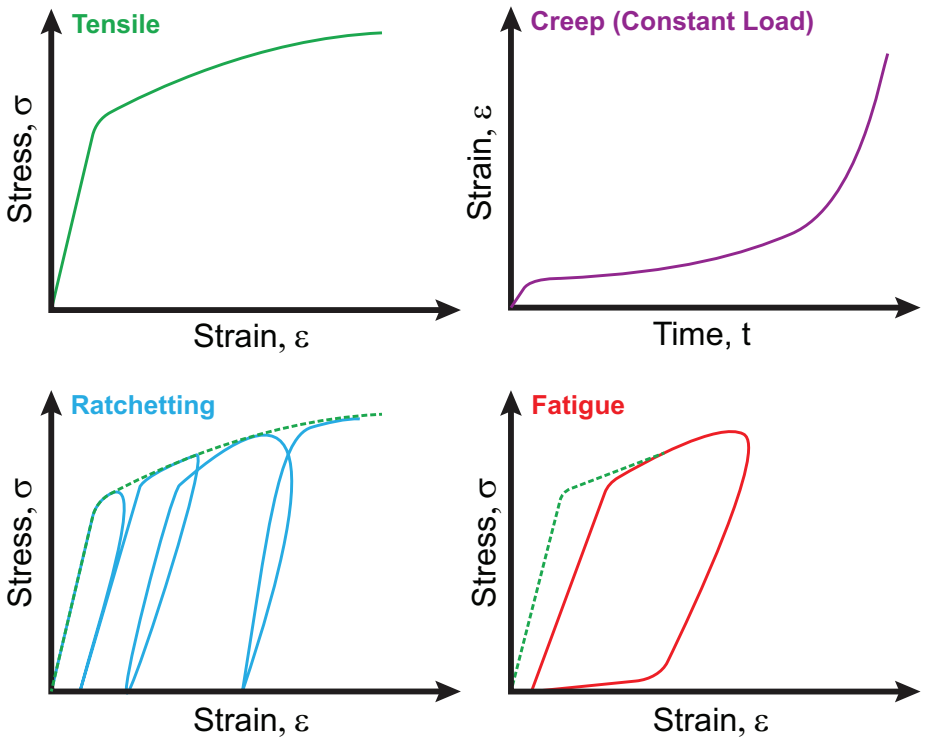

Figure 5.2: The amount of strain (ε) that develops in a uniaxially loaded material depends on both the applied stress (σ) and the loading conditions (tensile, creep, ratchetting, and fatigue).

creep fractures [90].

Ratchetting and fatigue are the two types of cyclic damage that are observed in materials, and they arise from different mechanisms (Fig. 5.2) [91, 92]. When a material is stressed in tension above its yield strength (but not to failure), plastic deformation and damage can accumulate. If the material is then unloaded and then reloaded to a higher stress (and strain), the loading path will be bounded by an envelope defined by its uniaxial tensile behavior. If the loading-unloading hysteresis loop does not close on itself, additional loading cycles will cause progressively larger ratchetting strains to accumulate. Ratchetting fractures occur as the tensile fracture strain is approached. Ratchetting arises in a wide range of materials including paper [89, 90, 93–96], and is most prominent in materials that show significant time-dependent (creep) deformation (reviews by Ohno and Kang [91, 92] detail ratchetting and how it is distinguished from fatigue). Ratchetting fracture sur-

faces in paper are hairy and indistinguishable from tensile fracture and creep because the damage mechanisms are essentially the same. However, if the cyclic stress amplitude is reduced so that the specimen lasts for tens of cycles or more, truly cycle dependent (fatigue) mechanisms can occur. However, high cycle fatigue damage in the hydrogen-bonded fiber network of paper and packaging materials has not been previously described or characterized.

5.2 Results and Discussion

This chapter will demonstrate how cellulose fiber networks in paper accumulated cyclic damage during high cycle fatigue loading. Notched paper specimens were loaded with monotonically increasing, constant, and sinusoidally varying cyclic stresses. By comparing the resulting tensile, creep, and fatigue damage accumulation rates and the fracture surfaces of each loading conditions, we will show that there is a unique cyclic damage mechanism in paper that is different from creep or tensile damage mechanism.

5.2.1 Cyclic Loading Lifetimes

A series of notched specimens were cyclically loaded with peak stresses greater than the yield stress, cyclic damage was accumulated, and the specimens eventually fractured into two pieces within about 10^6 cycles (Fig. 5.5). The number of cycles to failure, N_f, as a function of stress range, $\Delta\sigma$, showed the power law trend commonly observed in metallic materials [97]. The first indications of a distinct fatigue damage accumulation mechanism in paper became clear when we viewed crack profiles of the test specimens (Fig. 5.3). The short life fatigue specimen (Fig. 5.3b), which lived around 200 cycles at a stress range of 9.72 MPa, had a very fibrous and hairy fracture path like the tensile test specimens (Fig. 5.3a). However, the fatigue crack profiles of the intermediate and long life specimens were quite different. The fibers adjacent to the notch of the intermediate life specimen (Fig. 5.3c) ($N_f = 20000$ cycles at a stress range of 7.2 MPa) were fractured instead of

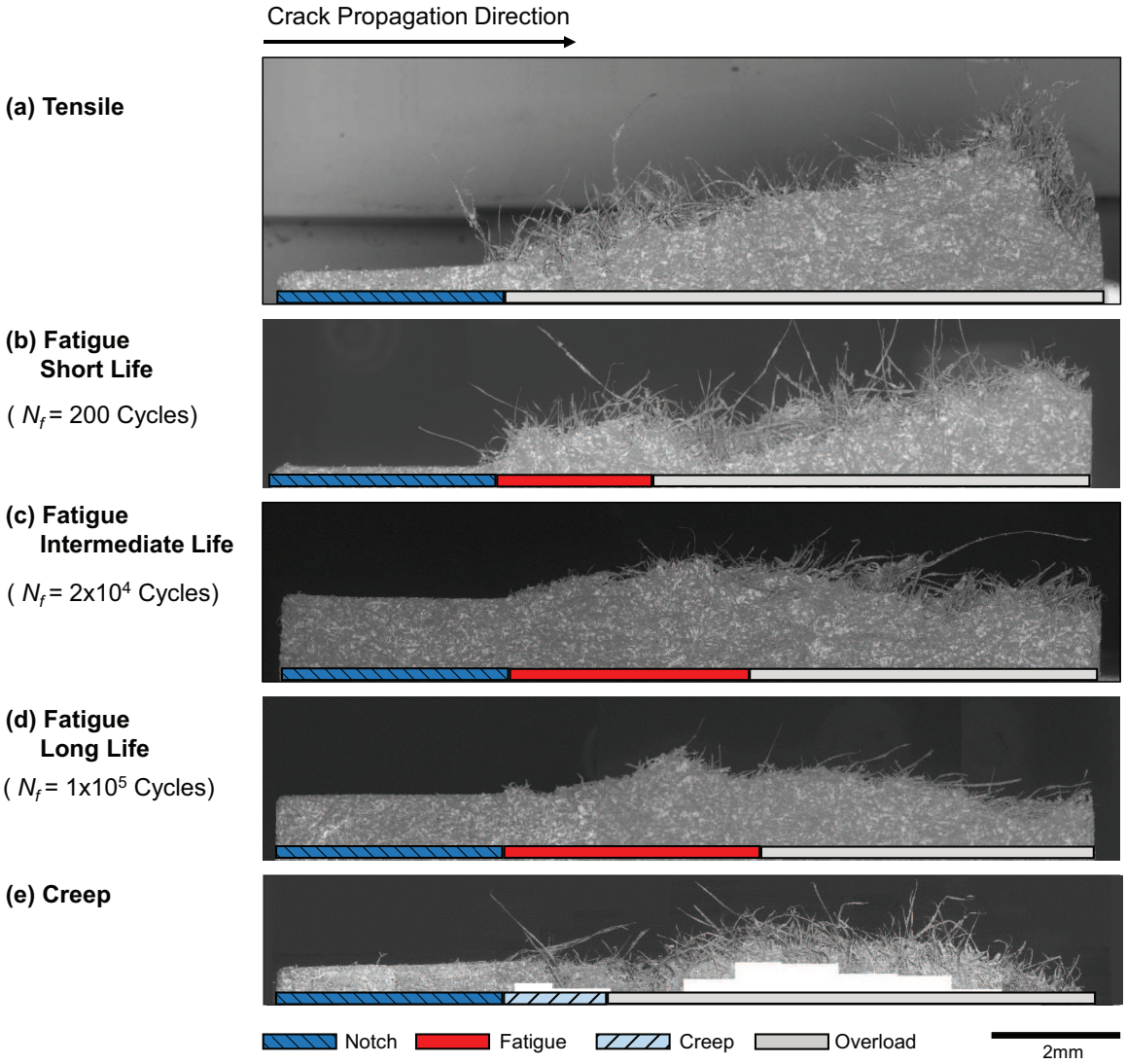

Figure 5.3: Scanning electron microscopy was used to image representative crack profiles of notched paper specimens that failed during tensile, fatigue, and creep tests. The cracks grew completely across the specimen from the cut notch tip as indicated in the figure. Tensile overload and creep fractures are fibrous (hairy) because the inter-fiber bonds fail and fibers pull out. In contrast, fatigue damage causes fiber fracture and less fibrous fracture surfaces. The various parts of the crack path (notch, fatigue, creep, and overload) for each specimen were determined using strain field mining and can be identified using the horizontal bar under each crack profile and the legend.

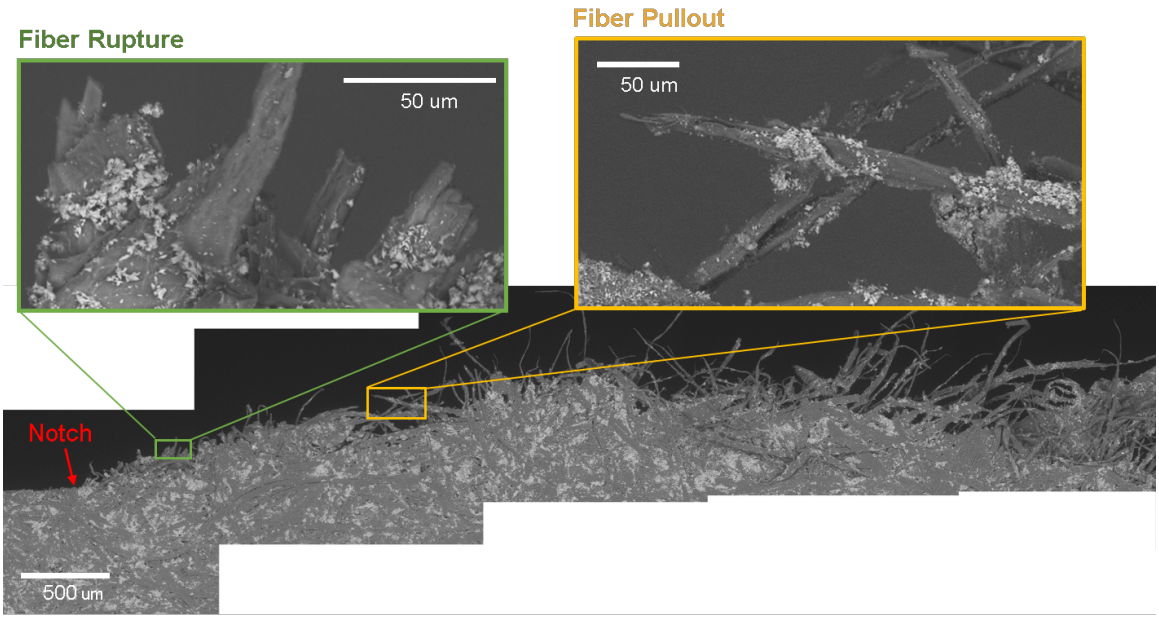

Figure 5.4: Zoomed in fracture profile images of the fatigue intermediate life specimen shown in Figure 5.3. Near the notch tip, the profile shows fiber fracture due to the fatigue damage accumulation. Away from the notch tip, the specimen failed via fiber pull-out.

pulled out, so the fracture surface near the precut notch was not hairy (Fig. 5.4). The crack growth mechanism transitioned back to the hairy, fiber pull-out mechanism when the fracture toughness of the specimen was exceeded. A longer fatigue damage region (fractured fibers) was observed in the crack profile of a long life specimen (Fig. 5.3d) (N_f =100000 at stress range of 5.4 MPa). Therefore, from the crack profiles of different fatigue specimens, we concluded that the damage mechanism in paper due to fatigue was distinct from the mechanism observed in other failure modes.

5.2.2 Strain Field Mining for Cracks

The mechanisms that enable fatigue damage accumulation are classified based on how and where damage accumulates as a crack grows [97]. Intrinsic mechanisms such as cyclic plastic deformation occur in a zone ahead of the advancing crack. In contrast, extrinsic mechanisms generally operate in a region behind the crack tip. Real materials are complex, so multiple intrinsic and extrinsic fatigue mechanisms are often observed along with

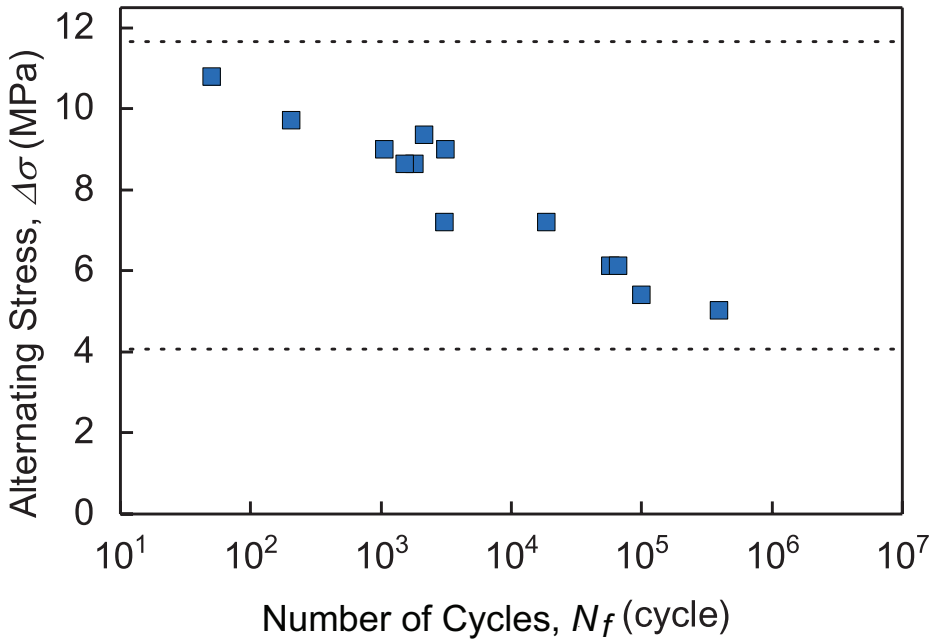

Figure 5.5: The high cycle fatigue life (N_f) was measured as a function of the applied alternating stress range ($\Delta\sigma$). The fatigue lives ranged from < 100 to nearly 10^6 cycles to failure for stress ranges that were bounded by the notched specimen ultimate and yield strengths, respectively (dashed lines). The error bars were smaller than the symbols used to denote the fatigue lives.

time-dependent crack growth mechanisms (e.g., creep). An effective strategy for isolating damage mechanisms is to monitor the growth of cracks under strategically selected, controlled loading and environmental conditions. In conventional, dense structural materials it is relatively easy to define the location and size of a crack because it is bounded by free surfaces. Unfortunately, it is very difficult to clearly observe and define cracks in the heterogeneous, porous, heavily bridged fiber networks found in wood fiber-based paper and packaging materials. In the case of our paper specimens, it was impossible to use transmitted and/or reflected visible light images to directly define the length of the crack during our experiments because crack lengths were underestimated in the optical images (Fig. 5.6). The porous fiber network structure and diffuse (extrinsic bridging) damage made it difficult to distinguish the crack. Instead, we developed a strain field mining strategy that quantified the fatigue damage zone extent (size) and growth rates (see section 2.4.5 for details). The spatial distribution of the experimentally measured strains were used to identify continu-

Table 5.1: Strain field mining was used to experimentally measure the average (up to a=6 mm) and maximum fatigue crack growth rates as a function of the alternating stress range.

Alternating Stress, $\Delta\sigma$ (MPa)	Average da/dN (mm/cycle)	Maximum da/dN (mm/cycle)
5.04	8.31×10^{-6}	2.91×10^{-5}
5.4	3.97×10^{-5}	3.31×10^{-4}
6.12	5.25×10^{-5}	3.26×10^{-4}
6.12	5.55×10^{-5}	1.69×10^{-4}
7.2	1.74×10^{-4}	6.92×10^{-4}
9	2.19×10^{-3}	2.96×10^{-3}

ous, crack-like regions where the fiber network had failed. This is the first application of this type of approach to heterogeneous fiber composites. It is important to note that the crack sizes found using the strain field mining were much larger than the apparent crack sizes in the optical images because changes in light transmission only become visible once all the fibers have moved from their initial positions- which occurs long after the fiber or inter-fiber failure. We then were able to measure the crack growth rates and recorded specimen lives under fatigue ($\Delta\sigma = 5.04 - 9$ MPa), creep ($\sigma = 6.8$ MPa), and various alternating creep-fatigue loading conditions.

The fatigue crack growth rates systematically decreased as the applied stress amplitude was reduced (See Fig. 5.7 and Table 5.1). The maximum fatigue crack growth rate was 2.96×10^{-3} mm/cycle for the specimen with the highest stress amplitude and shortest life ($\Delta\sigma = 9$ MPa, $N_f = 1228$). The growth rate dropped by two orders of magnitude (2.91×10^{-5} mm/cycle) when the driving force was reduced ($\Delta\sigma = 5.04$ MPa) and the specimen lasted 300 times longer (381 628 cycles). Table 5.1 shows that as alternating stress was increased, the average and maximum crack growth rate of paper under cyclic loading increased.

The suitability of the linear elastic stress intensity factor range, ΔK, as a characterizing

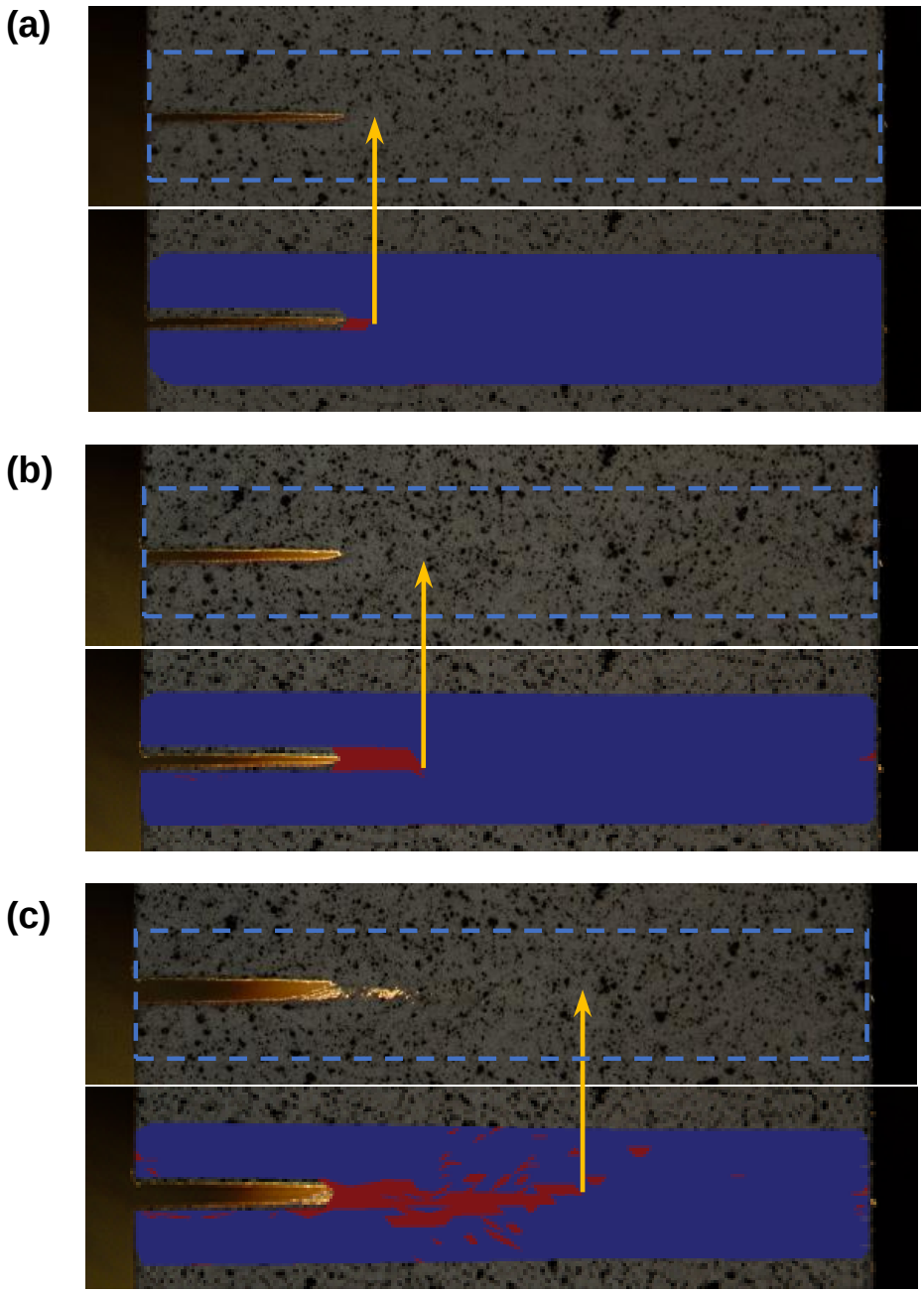

Figure 5.6: Optical images (top) and thresholded strain map overlaps (bottom) showing extent of crack growth at (a)early, (b)intermediate, (c)late stages of a fatigue test. It was difficult to discern the crack tip in the transmitted light optical images, but the thresholded strain maps allowed for measurement of the crack length. The total width of the specimen is 12.5 mm

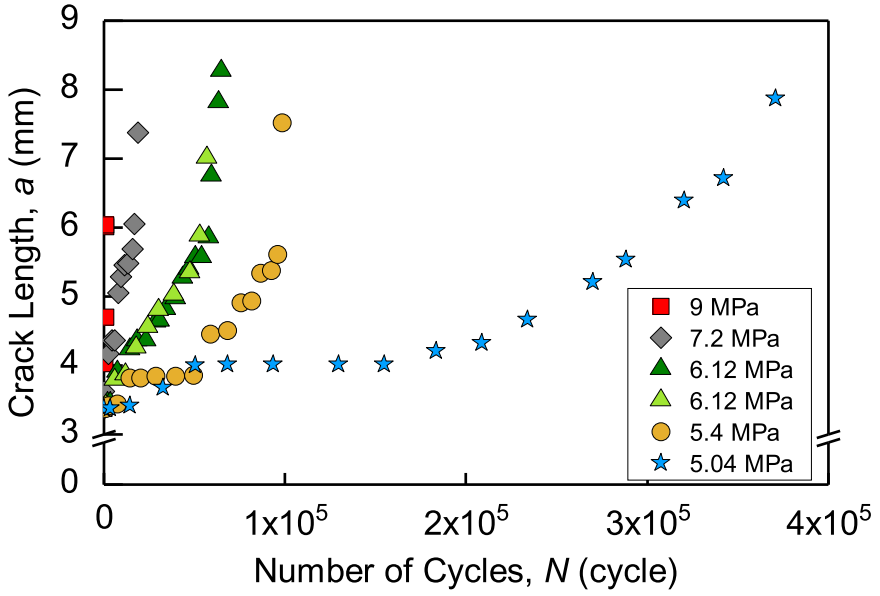

Figure 5.7: Strain field mining was used to determine the crack length as a function of the number of applied cycles. The legend indicates the alternating stress range for each specimen. The error bars were smaller than the symbols used to denote the crack lengths.

parameter for fatigue crack growth in paper at room temperature was considered. The ΔK for a given fatigue crack growth rate was calculated using the relevant crack length (determined from the strain field mining technique described in the methods section) and a K solution established in our previous studies of single edge notched tension specimens held in fixed grips [98]. The solution had the general form $\Delta K = \Delta\sigma Y\sqrt{\pi a}$ where $\Delta\sigma$ was the applied stress range, a was the crack length, and Y was the geometric term shown below (eq. 5.1).

$$Y = 1.12 - 1.54(\frac{a}{w}) + 30.80(\frac{a}{w})^2 - 146.63(\frac{a}{w})^3 + 341.81(\frac{a}{w})^4 - 365.38(\frac{a}{w})^5 + 145.67(\frac{a}{w})^6 \quad (5.1)$$

Figure 5.8 shows the crack growth rate (da/dN) at the calculated ΔK values. It was clear that fatigue crack growth in paper at room temperature is not ΔK-controlled: A unique growth rate for a given ΔK was not observed. Instead the fatigue crack growth rate varied

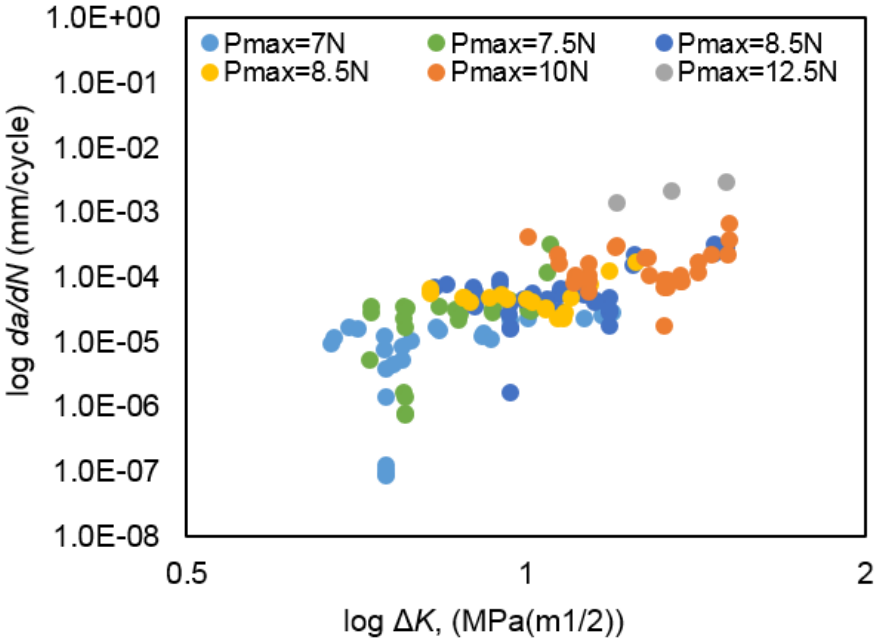

Figure 5.8: Crack growth rate versus ΔK values for fatigue specimens with different cyclic loading amplitudes

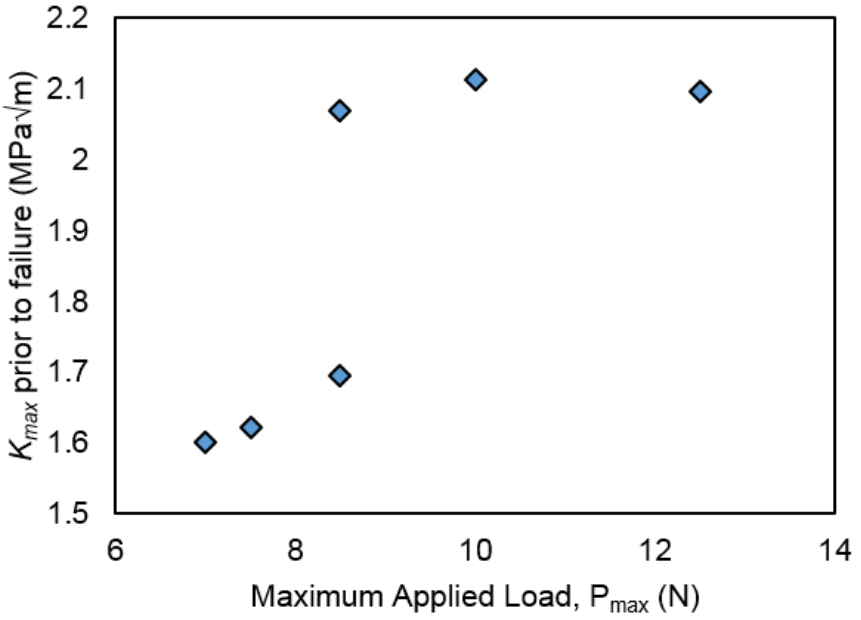

Figure 5.9: ΔK_{max} values just prior to failure for six fatigue specimens with different cyclic maximum loads (P_{max}) applied

(by up to two orders of magnitude), and depended on the stress range that was used. This also alluded to a companion observation: the apparent fracture toughness of the paper cannot be characterized with K. Figure 5.9 shows the maximum K value just prior to failure for different fatigue specimens. K_{max} is a measure of the apparent fracture toughness, which ranged from 1.6 to 2.1 MPa$\sqrt{\text{m}}$. If K were an appropriate crack tip characterizing parameter for paper, then it would uniquely correlate to crack growth rate or fracture toughness. Therefore, fatigue crack growth cannot be correlated with the linear elastic fracture mechanics parameter, ΔK.

5.2.3 Fatigue-Creep Interaction in Paper

The fatigue crack growth rate was sensitive to the applied stress and loading mode (constant, monotonically increasing, and cyclic), so we examined the creep and fatigue damage accumulation mechanisms and their synergistic interactions. Figure 5.10 shows two fatigue only specimens (F1 and F2) that lived 57329 and 65970 cycles. Two other specimens were subjected to a sequence of cyclic loading, constant loading, and back to cyclic loading (Fatigue→Creep→Fatigue). Another two specimens were subjected to constant loading then cyclic loading (Creep→Fatigue). The total fatigue loading cycles lived by each of these four specimens were 101 591 cycles (FCF1), 73 833 cycles (FCF2), 354 741 cycles (CF1), and 192 498 cycles (CF2). These specimens subjected to combinations of cyclic and constant loadings all lived *longer* than the specimens that were only subjected to cyclic loading. Depending on the combination of loading conditions, the fatigue life endured by a paper specimen was increased up to 6.2 times. This was surprising given the general perception that creep damage is more important than fatigue for the life of packaging materials. It was clear that the creep and fatigue damage mechanisms in paper are different, and there is a synergistic interaction between creep and fatigue that can *enhance* fatigue resistance.

Like most materials, it was difficult to tell just from the total life data how creep and

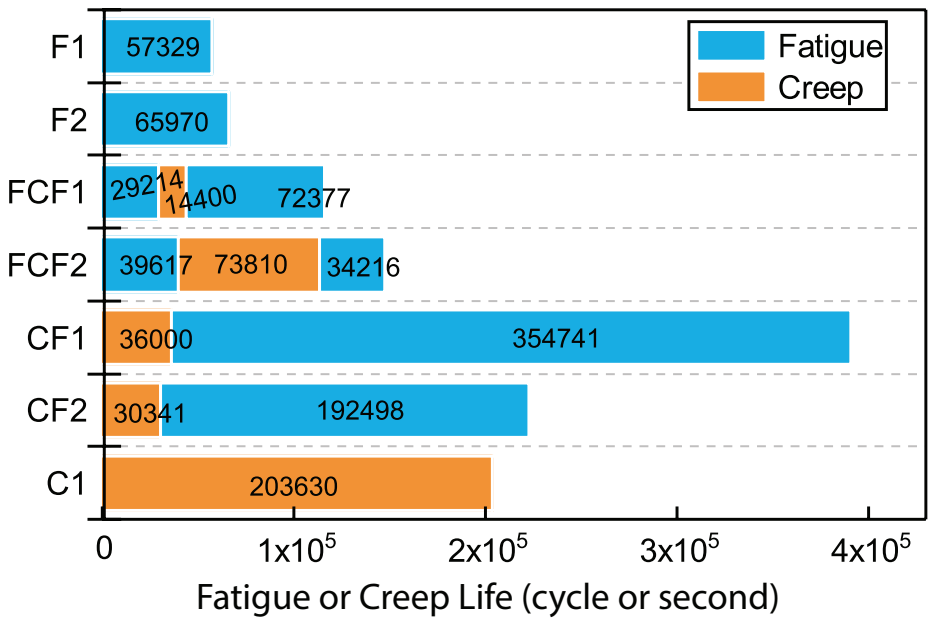

Figure 5.10: The specimen life (in number of cycles or seconds for fatigue and creep loading conditions, respectively) were measured. The application of a constant stress induced creep damage that extended the specimen life because it inhibited fatigue damage accumulation.

fatigue processes interact in paper [97]. Once we used our strain field mining approach to identify the crack size (see section 2.4.5), the interactions between and relative importance of the creep and fatigue became clear. Figure 5.11 shows how cracks grew in fatigue, creep, and alternating creep-fatigue loading conditions. As previously shown in Figure 5.7, for the two specimens (F1 and F2) subjected to cyclic loading only ($\Delta\sigma = 6.12\,\text{MPa}$), the crack grew at a constant rate ($3.9 \times 10^{-5}\,\text{mm/cycle}$) until crack size was around 6 mm when the growth rate accelerated an order of magnitude to $3.4 \times 10^{-4}\,\text{mm/cycle}$. Creep cracks (C1) grew an order of magnitude slower ($2.5 \times 10^{-6}\,\text{mm/cycle}$) than the cyclically loaded specimens. Clearly fatigue damage accumulated more rapidly than creep under these conditions. For the fatigue-creep-fatigue specimens (FCF1 and FCF2), the crack growth rate under the initial cyclic loading was similar to the rate of fatigue only specimens because specimens in both cases were subjected to the same loading condition. When the condition was switched to constant loading, the crack growth rate was dramatically reduced to a rate similar to that of the creep only specimen, $2.5 \times 10^{-6}\,\text{mm/cycle}$. However, an interesting observa-

tion was made when we switched the loading condition back to cyclic loading. When the specimen FCF1 was cyclically loaded for the second time after the constant loading, the crack growth rate remained very low, 3.3×10^{-6} mm/cycle, which was an order of magnitude smaller than when the specimen was subjected to cyclic loading at the beginning of the experiment prior to the constant loading (3.2×10^{-5} mm/cycle). A more dramatic delay in the fatigue crack growth was observed in the two Creep-Fatigue specimens (CF1 and CF2). When the loading was switched to cyclic loading after a short period of constant loading (about 30 000 sec), the crack growth rate stayed small (3.0×10^{-6} mm/cycle and 2.5×10^{-6} mm/cycle). Compared to the crack growth rate of fatigue only specimens (F1, F2), the fatigue crack growth here is an order of magnitude slower. The rate stayed small for at least 150000 cycles, then the rate increased to 3.1×10^{-5} mm/cycle and 3.5×10^{-5} mm/cycle, driving the crack to failure. Therefore, the fatigue crack growth rate of CF1 and CF2 specimens were an order of magnitude slower than that of F1 and F2 specimens during the entire time that the specimens were loaded in cyclic tension.

The different crack growth rate behaviors and fracture profiles in creep-only and fatigue only specimens suggest that the damage mechanisms are different between the two loading conditions. The creep specimen, having a similar crack profile as the tensile overload specimens (Fig. 5.3), must have a similar type of final damage, where more bonds breaks than fibers do. It is known that the creep characteristics of paper are mostly due to the microcompressions that exist in bonds and fibers [4]. As the microcompressions get released, the material elongates under a constant loading condition. The microcompressions will be permanently released if plastically deformed or will be back to the compressed state if elastically deformed. For the specimens that showed delays in fatigue damage after subjected to creep damage, it is likely that the structural change during the creep damage is helping the specimen survive the fatigue damage accumulation and resist crack growth. One postulation is that energy necessary to grow fatigue cracks was being used to extend and close the microcompressions that were elastically released (activated) during the previous creep

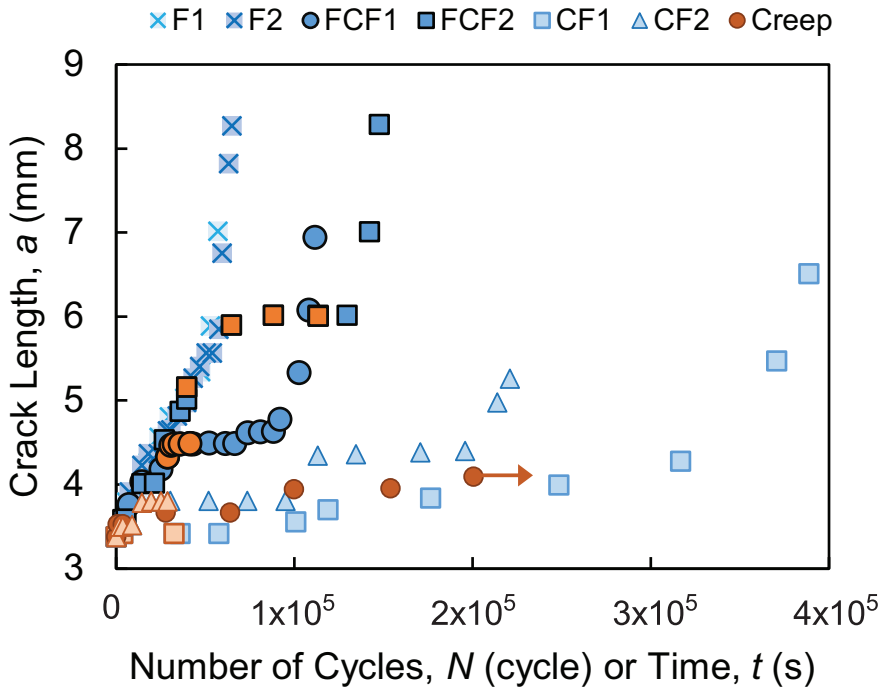

Figure 5.11: The crack length (a) as a function of accumulated cycles (N) during the cyclic and constant stress loading experiments was measured using strain field mining. The horizontal arrow indicates that the experiment was halted before the specimen failed. The error bars were smaller than the symbols used to denote the crack lengths.

damage. Without the activation during the creep stage, cyclic loads were directly used to debond the hydrogen bonds and wear out the fibers with frictional or bending damage.

It was clear from the fracture surfaces and crack growth rate trends that high cycle fatigue had a distinct damage accumulation mechanism. During tensile fracture, creep, and ratchetting, the fibers deformed and moved relative to one another [4, 5]. Ultimately, the interfiber bonds failed because they were weaker than the fibers themselves. In contrast, during high cycle fatigue the fibers fractured. In principle, the preferred crack path and micromechanism could change with the fiber network topography, composition, and environment. Paper fiber networks have several characteristic length scales that define the types of locations where high cycle fatigue can cause fibers to fracture. The fibers in this study (see section 2.1 and [65] for additional details) had an average length of 0.704 mm and diameter of 21.6 μm. Both the higher and lower fiber density regions (also known as floc and interfloc, respectively) had characteristic length scales on the order of several millimeters. One could argue that an interfloc fatigue crack path should have been energetically favored because fewer fibers rupture per unit crack extension. However, we did not find evidence of such a preferred fatigue crack path. Thus we concluded that there were two possible types of fiber network locations that could accumulate high cycle fatigue damage. First, contact damage (fretting) could have occurred where the fibers touched each other. These contacts could occur at interfiber bonds formed when the paper was manufactured, or when fibers moved into contact during deformation. Second, individual fibers could have accumulated high cycle fatigue damage in the regions between the interfiber bonds. In principle, these two classes of high cycle fatigue damage accumulation can operate simultaneously. However, the dramatic reductions in fatigue crack growth rate after exposure to creep loading conditions suggested that high cycle fatigue damage occurred preferentially at the interfiber bonds because creep is dominated by strain accumulation at interfiber bonds [4]. These new insights will allow for the fiber properties and network topography in paper to be engineered for high cycle fatigue damage resistance.

5.3 Conclusions

In this chapter, we used a strain field mining strategy to quantify the growth rates of damage in paper during constant and cyclic stress conditions. We found that there is a distinct fatigue damage accumulation mechanism in paper that causes fiber fracture, instead of inter-fiber bond failure. The fracture surfaces indicated that tensile and creep failure occur by fiber pull-out (and inter-fiber bond failure) where fatigue failure, in contrast, occurs by fiber fracture.Fatigue specimens that were subjected to lower stress amplitudes lived longer and exhibited a longer portion of fiber fractured profile when they did fail, indicated by a clean, sharp crack profile. Moreover, we found that pre-applied creep damage in paper can help delay the upcoming fatigue damage accumulation and extend paper's high cycle fatigue life, possibly due to a structural change at interfiber bonds in the network caused by creep damage.

CHAPTER 6
FRACTURE PROCESS OF PAPER

In this chapter experimentally measured crack tip strain fields established that tearing of paper is a steady-state process. The force required to grow a crack in MD and CD orientated single edge notched tension (SENT) specimens under displacement-controlled conditions was measured. The relationship between the applied nominal stresses and normalized crack lengths followed the three stage process that has been observed in thin, ductile metal sheets. Finally, strain field mining revealed the extent and evolution of the crack tip process zones, and that (like metals) steady-state zone of active plasticity (ZAP) developed during tearing of paper.

6.1 Introduction

Understanding the size and shape of crack tip process zones is essential for reliable crack growth predictions using engineering fracture mechanics methods. Fracture mechanics methods should be applicable to manufacturing, converting, and end use performance of paper products [99]. The resistance of paper products to subcritical crack growth and fracture have been studied for decades, and linear elastic and elastic plastic fracture mechanics methods (LEFM and EPFM, respectively) have been applied. The stress intensity factor, K from LEFM is the simplest among the fracture mechanics approaches and should be applicable if the crack tip process zone is small relative to the crack length and specimen width. Previous research showed limited success in using very large specimens to ensure small scale yielding conditions [72, 100]. Later attempts to use elastic-plastic fracture mechanics (i.e., J-integral approach) to predict paper's fracture were also unsuccessful [101–104]. For example, Wellmar et al.[102] calculated the J-integral for their experimental configuration, but it was not a valid crack tip parameter (i.e., the result was not independent of specimen

and crack geometries) [103, 104]. Lastly, the essential work of fracture (EWF) approach was used to measure the fracture toughness on double edge notched tension (DENT) paper specimens [103, 105, 106]. This method is effective when the plastic zone is geometrically constrained to be an elliptically-shaped region between the crack tips, but was not generally applicable. Despite the decades of research, there is still no generally accepted fracture mechanics methodology for evaluating crack growth in paper [99, 107].

Understanding how deformation, degradation, and failure occur in the crack tip process zones are the key to using fracture mechanics for paper products. The peculiar features of the process zones in paper are a byproduct of its fiber network structure. Paper is known to have a large process zone ahead of a crack tip, where micromechanical processes of crack growth such as fiber pull-out, realignment, and breakage occur [64, 108]. The long fibers are distributed amongst the floc and interfloc regions, so the plastic zone is larger and its boundaries are more diffuse than seen in fully dense materials. As a result, deformation and damage accumulate in volumes that are very large compared to the fiber dimensions [2]. Additionally, the failure of the network structure causes significant fiber pull-out and crack bridging, so it is difficult to measure the crack lengths of paper. Several works have attempted to directly and indirectly observe the onset of stable crack growth and deformation around the crack front using IR thermography and image analysis. Tanaka et al.[106] and Yamauchi et al.[109] used an infrared thermography system to track the temperature distribution and observed an elliptically shaped process zone in DENT specimens. Similarly, Wanigaratne et al. used an image analysis method (grayscale intensity comparison) to measure a deformation field around a crack tip in a DENT specimen and concluded it was approximately elliptical or circular [110]. However, they reported a very *small* observation region ($2 \times 2\,\mathrm{mm}^2$), and actual deformation maps were not shown. Zechner et al. used comparatively higher resolution digital image correlation (DIC) to determine the crack length in a single edge notched tensile (SENT) specimen [108], but the crack tip strain maps or deformation maps were neither shown nor discussed. The crack tip process zones in paper

are directly linked to the characteristic length scales of the fiber network and the materials ability to concentrate energy in specific regions of the structure [111]. In this work we examined the evolution of the crack tip process zones that develop during the stable tearing of a heterogeneous fiber network material, paper.

6.2 Results and Discussion

Copy paper and aluminum foil have remarkably similar elastic–strain hardening plastic constitutive behavior and material forms. However, the underlying deformation, hardening, and failure mechanisms are radically different. Plastic deformation in pure aluminum is a dislocation glide process and is isochoric. In contrast, plastic deformation in paper is due to a combination of fiber rearrangement and interfiber bond rupture, and it is not an isochoric process. Similarly, the types of and criteria for plastic instabilities are different– deformation bands may form in paper, but diffuse and/or transverse necks do not. These differences in structure and deformation mechanism allowed us to explore fundamental questions about crack growth mechanisms in very thin, ductile sheets.

6.2.1 Steady-state Crack Propagation

In our recent studies of thin sheet 1235 aluminum [98, 112, 113], we found that very thin ($<$1 mm) sheets of ductile metals showed a three-stage tearing process: crack growth initiated from the notch (I), and after a transition (II) steady-state conditions prevailed (III). Crack tip process zones are at steady-state if the shape and magnitude of the incremental strain field remains fixed as the coordinate system (reference frame) translates with the growing crack tip [114]. We proved the existence of steady-state conditions when we showed that the size of the zone of incremental active plasticity (ZAP) and the characteristic (net section) stress, σ_c, were both constant. It is important to note that the fracture process zone in aluminum contained a large amount of transverse necking; the fracture surfaces were a fine, transgranular ridge (i.e., nearly 100 % reduction in area) that was essentially

free of microvoids. Because the tearing was a steady-state growth process, it could not be characterized with conventional (static) linear elastic or elastic-plastic fracture mechanics. Instead, crack growth was predicted from the materials (thickness dependent) characteristic steady-state stress, σ_c [98, 112, 113]. If steady-state conditions develop during tearing of paper, then we know how to develop an appropriate fracture mechanics framework. Secondly, the similarities and differences between paper and aluminum foil tearing will allow us to determine if steady-state conditions are a byproduct of the relative sizes of the sheet thickness and crack tip plastic zones instead or of transverse necking in the fracture process zone.

The nominal stress, $\sigma = \frac{P}{B \times w}$, and normalized crack length, $\frac{a}{w}$, were measured for a series of notched copy paper specimens. As shown in Figure 6.1, the single edge notched, MD and CD oriented specimens (initial notch sizes of $\frac{a}{w} = 0.20, 0.25, 0.30$) followed the same crack growth trend: the crack did not grow until the maximum nominal stress was reached. Once the crack started to grow, the nominal stress decreased linearly. Like the thin aluminum sheets, we divided these plots into three parts: initiation, transition, and steady-state. The end of the initiation stage was defined as the maximum nominal stress (without noticeable crack growth). The end of the transition stage was distinguished from the linear, steady-state portion of the response using a set of cutoff criteria (Fig. 6.3). Although specimens with larger initial notch sizes started growing cracks at lower nominal stresses, every specimen reached steady-state regardless of the notch sizes. This trend was previously observed in thin sheet ductile metals; however, the nominal stress value at the end of crack growth ($a/w = 1$) in paper was non-zero. In metallic system, crack growth fully separates materials in two parts as the crack tip approached the back edge of the specimen because failure was controlled by intrinsic (plastic deformation) mechanisms (see Fig. 2.5). However, because paper is an extrinsically toughened fiber network material the specimen was was able to carry load when the crack tip reached the back edge of the specimen ($\frac{a}{w} = 1$), as shown in Figure 6.2. The fractured path, traced with a red dotted line,

was identified visually as a subtly darker region because the pulled-out fibers affected light transmission.

The non-zero nominal stress that we observed at the end of the paper tearing experiments due to the fiber bridging required a slight modification to the analysis of variance (ANOVA) methods that we used in our previous work [112, 113]. From the steady-state region in Figure 6.1, the characteristic steady-state stress, σ_c, was extracted. As shown in Figure 6.3, the steady-state for each specimen was determined using a single criteria. For each specimen, any data points that had stress values greater than $0.85\sigma_{max}$ and normalized crack lengths greater than 0.95 were excluded from for calculating σ_c. The stress criteria ($\sigma < 0.85\sigma_{max}$) was to account for the transition part of the propagation curve near the start of the crack growth, and the crack length criteria ($a/w < 0.95$) was to account for the offset stress, σ_{offset}. Then, σ_c was obtained by a least squares linear fit through data for all specimens in each orientation. Figure 6.4 shows the linear fits through the data that satisfied the steady-state criteria. The stress-axis intercept (when $\frac{a}{w} = 0$) of the linear fit was the characteristic steady-state stress, σ_c, which is essentially a measure of the steady-state crack growth resistance.

As mentioned earlier, thin ductile metal specimens separate when crack is fully extended, so the fitted line is described by Equation 6.1. However, since paper has an offset stress, σ_{offset}, when $a/w = 1$, the fitted line follows Equation 6.2 instead.

$$\sigma = \sigma_c \cdot (1 - a/w) \tag{6.1}$$

$$\sigma = (\sigma_c - \sigma_{offset}) \cdot (1 - a/w) + \sigma_{offset} \tag{6.2}$$

With this relationship fitted in Figure 6.4, σ_c was found to be 37.3 MPa for MD specimens and 20.1 MPa for CD specimens, and σ_{offset} was 6.0 MPa for MD specimens and 2.9 MPa for CD specimens. The differences in σ_c and σ_{offset} values between the MD and CD

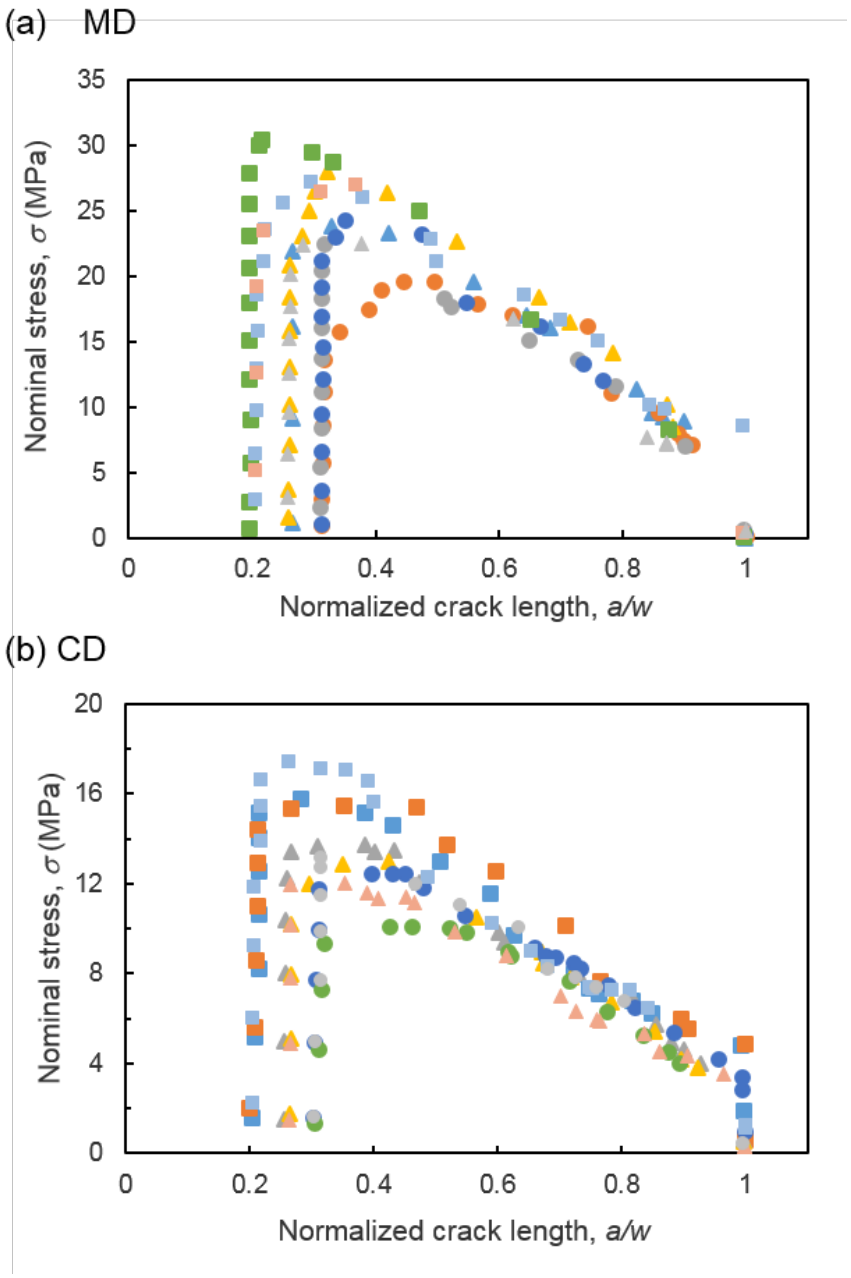

Figure 6.1: Nominal stress vs. normalized crack length plots of (a)MD and (b)CD specimens with three different initial notch sizes ($a/w = 0.20$ (square), 0.25 (triangle), 0.30 (circle)).

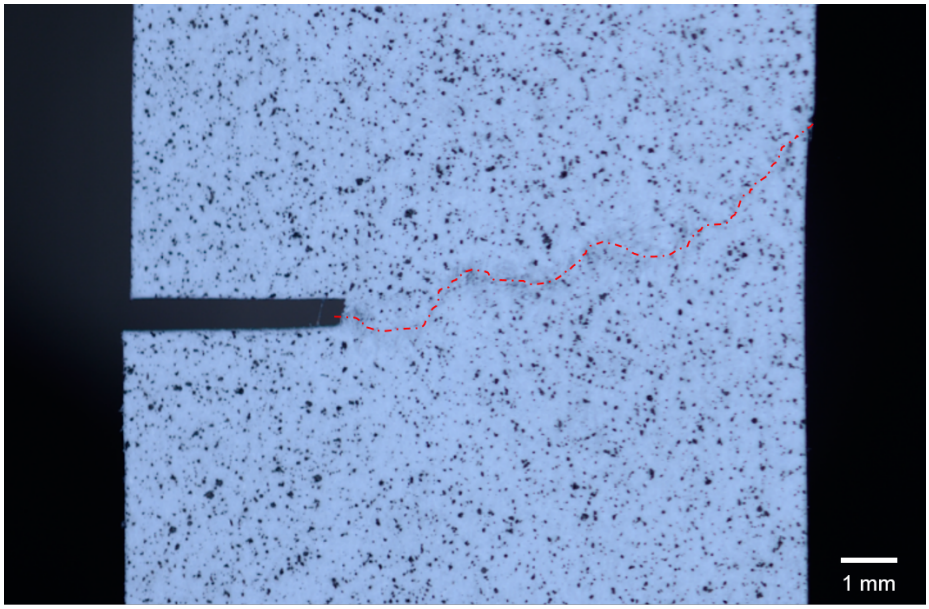

Figure 6.2: A representative optical image of a completely fractured specimen ($a/w = 1$). The fractured path, traced with a red dotted line.

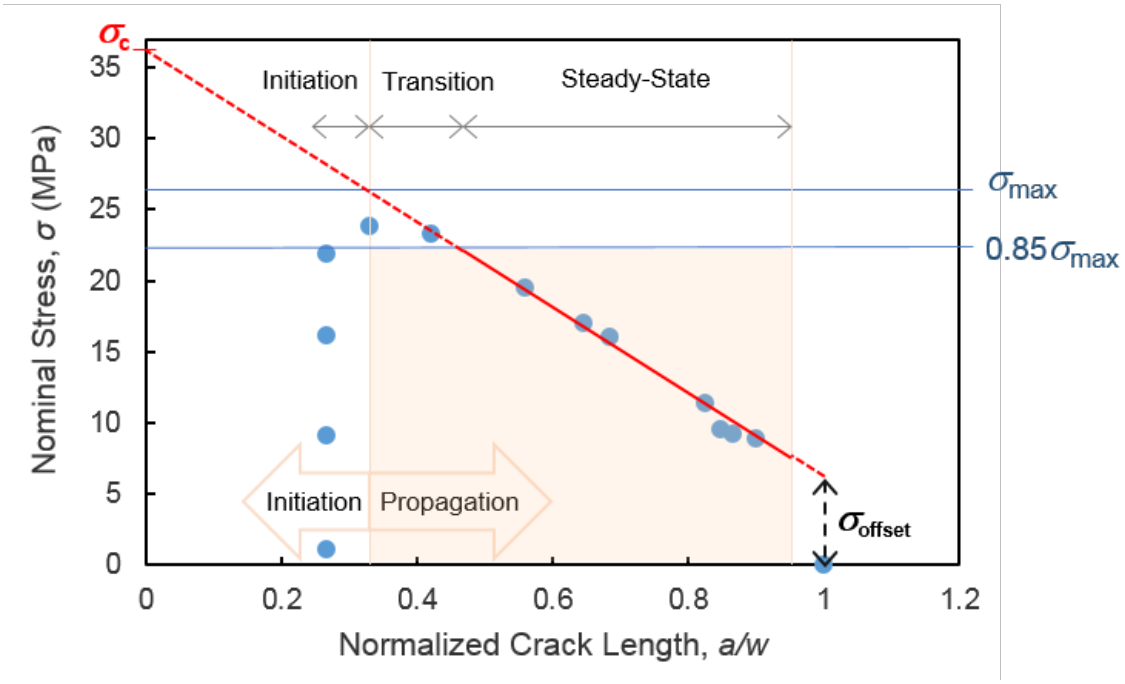

Figure 6.3: A representative nominal stress vs. normalized crack length plot, divided into three parts: initiation, transition, and steady-state. The characteristic steady-state stress, σ_c, can be found with the linear fit on the data points that satisfy the stress criteria ($\sigma < 0.85\sigma_{max}$) and crack length criteria ($a/w < 0.95$).

specimens were expected due to the anisotropic structure and tensile properties discussed earlier in the dissertation (see section 1.1 and Table 4.1). As shown in equation 6.3, the relationship between characteristic steady-state stress, σ_c and the net section stress for the uncracked ligament, $\frac{P}{B(w-a)}$ were obtained by rearranging equation 6.2.

$$\begin{aligned} \sigma_c &= \frac{P - P_{offset}}{B(w-a)} + \sigma_{offset} \\ \sigma_c &= \frac{P}{B(w-a)} - \sigma_{offset} \cdot \left(\frac{a}{w-a} \right) \end{aligned} \tag{6.3}$$

Unlike thin sheet metal systems where the net section stress equals σ_c, the relationship is not as simple due to the additional term, σ_{offset}, associated with the fiber pullout. Therefore, for describing the fracture of paper, we must know not only the characterizing steady-state stress, σ_c, but also the fiber bridging stress, σ_{offset}.

6.2.2 Crack Tip Plastic Zone

The nominal stress vs. normalized crack length plots (Figs. 6.1 and 6.4) showed that paper fracture followed a nominal stress versus crack length relationship that was similar to the the thin sheet metals. We then used the experimentally measured crack tip strain fields to determine if steady-state conditions were present. Figure 6.5 shows axial strains of a representative notched MD and CD specimens over the course of tensile loading. Shortly after specimens were loaded, the material ahead of the crack was plastically deformed (surpassed the yield strain, ε_y), which meant that the material was fully yielded before crack started advancing (images d-h). Also, a zone of highly localized strains appeared at the crack front, and the zone advanced as the crack tip advanced; however, the detailed shape and size of this plastic zone was hard to discern in these cumulative strain maps when the reference frame was the first image taken at the start of the experiment (zero load).

The incremental strain maps were calculated using a rolling window reference frame. 20 images were chosen as the rolling window, and this window frame corresponds to specimen extension of 0.67 millistrain at 0.1 mm/min cross-head displacement rate and 1 Hz

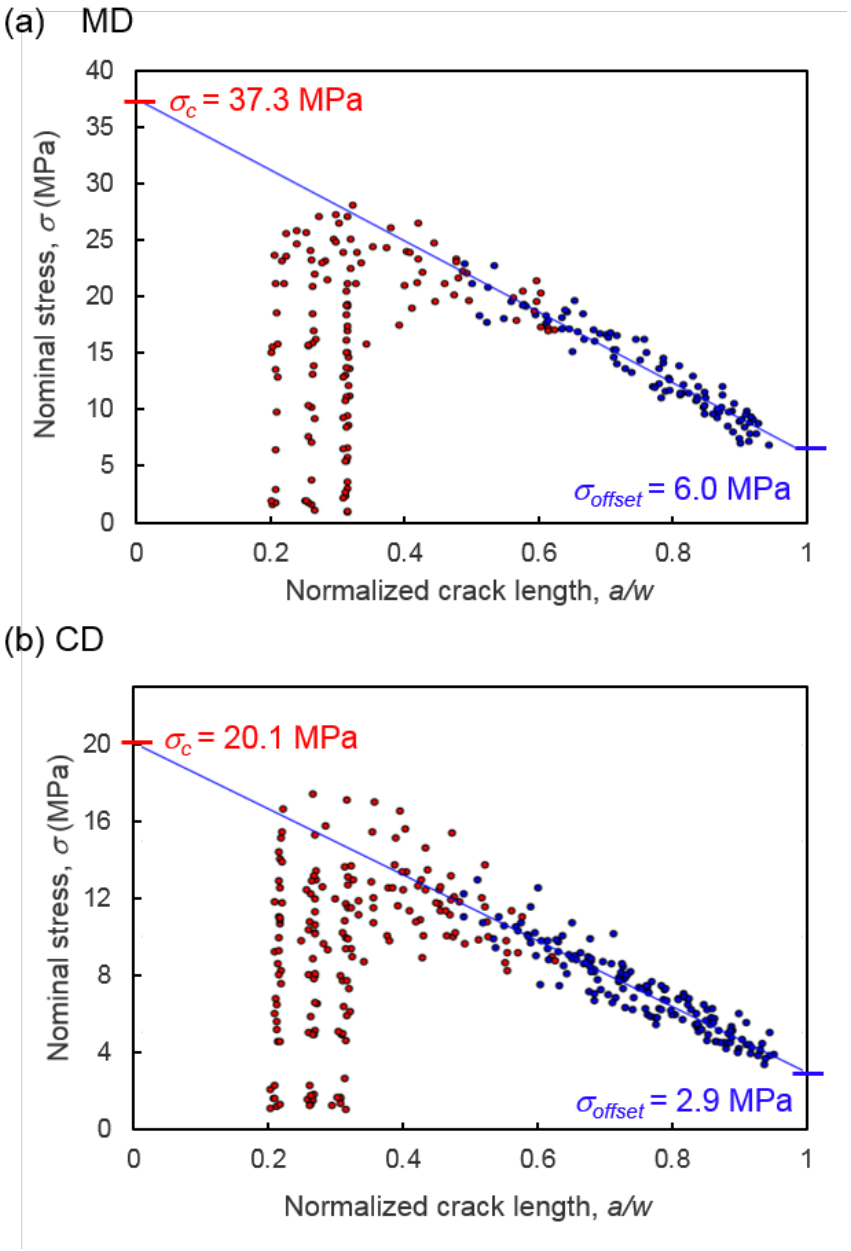

Figure 6.4: Nominal stress vs. normalized crack length plots showing the linear fit to steady-state region of the data.

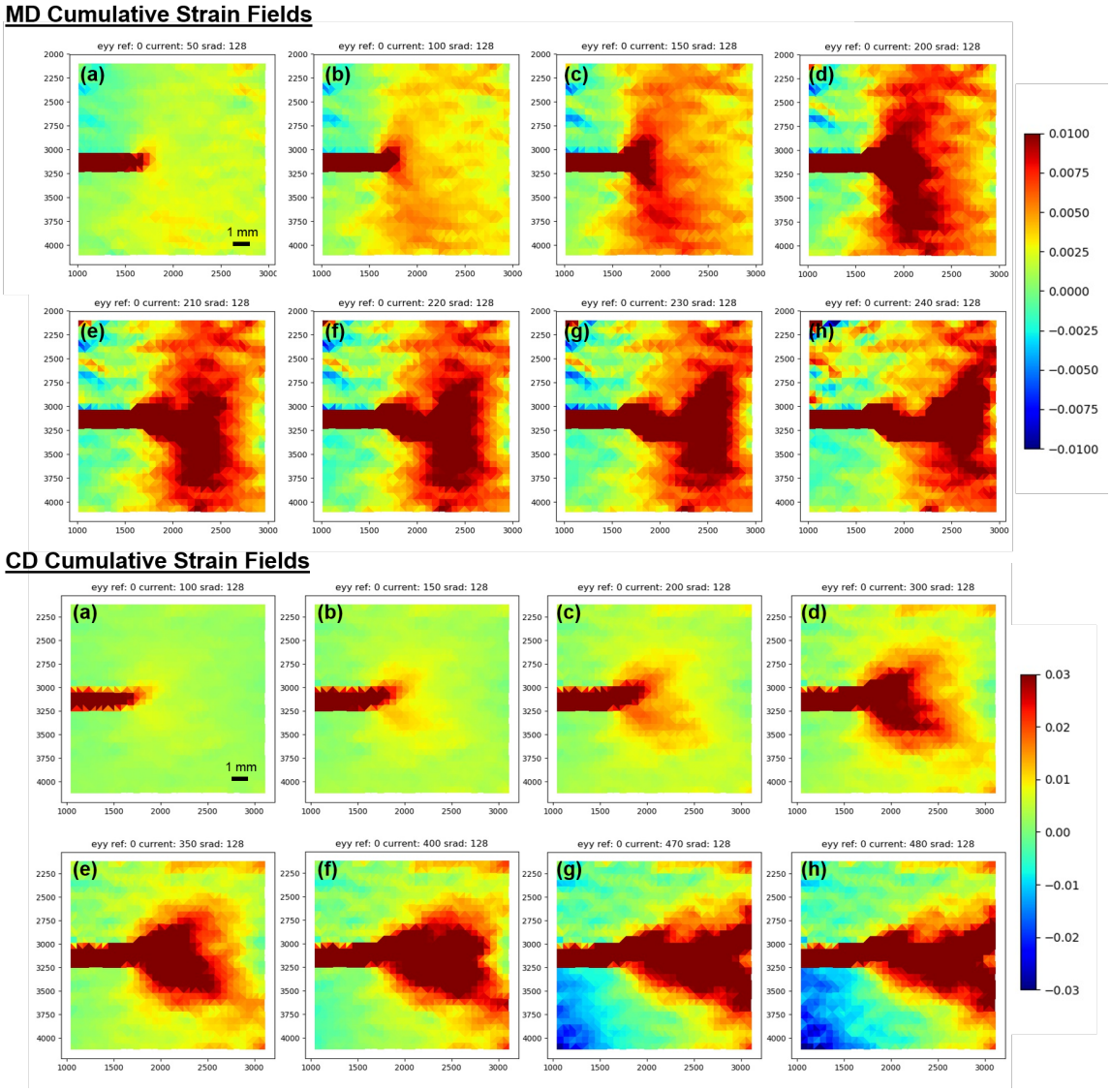

Figure 6.5: Cumulative strain maps of of representative MD and CD specimens. The strain maps were reference to the beginning of the tearing experiments.

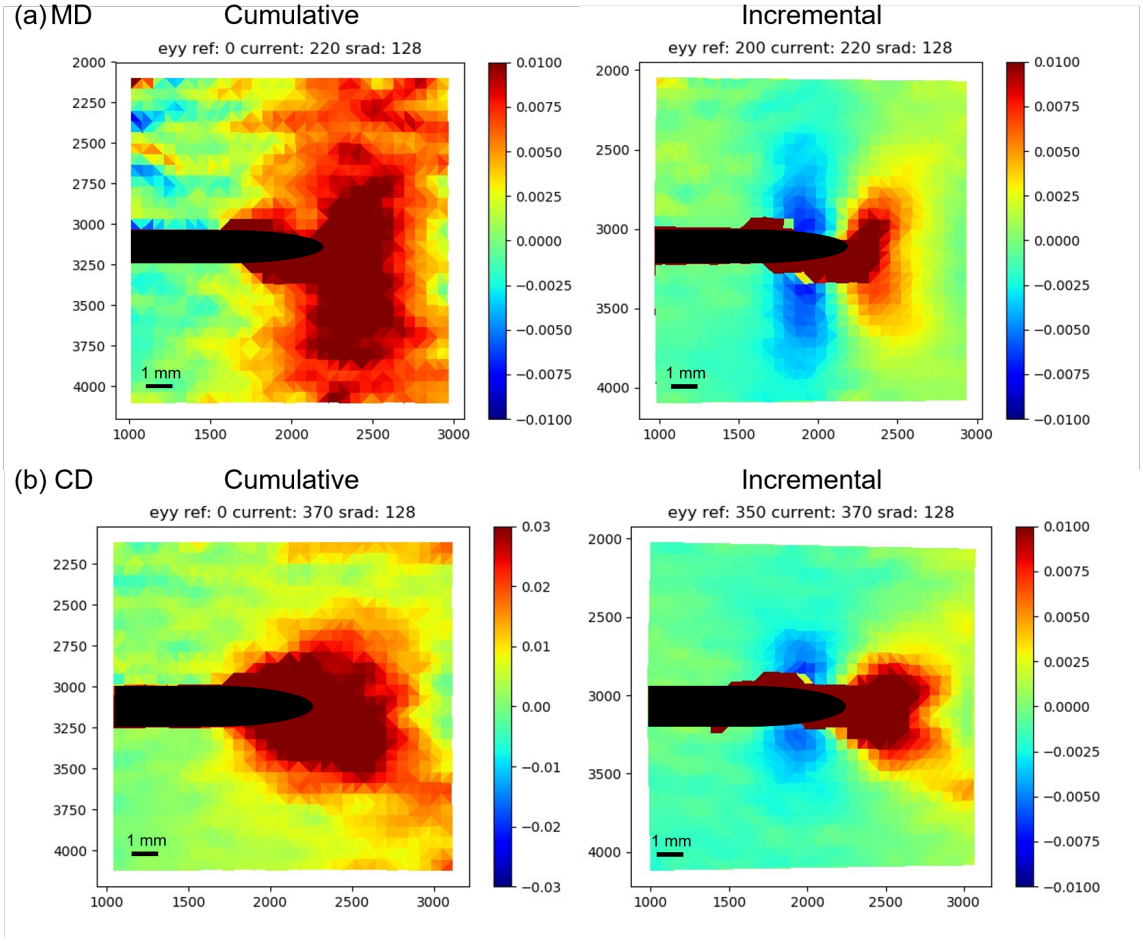

Figure 6.6: Cumulative vs. incremental strains of representative MD and CD specimens at $a/w = 0.6$. The cumulative strain maps are referenced to the first image where the incremental strain maps are reference to 20 images before ($\Delta\varepsilon = 0.00067$).

image capture rate. In Figure 6.5 the difference between the cumulative and the incremental strain maps are shown. The details of the process zone were hidden in the cumulative maps. However, the incremental strain maps revealed the true character crack tip process zones of paper. Figure 6.7 shows the evolution of incremental strain maps of the same specimens that was shown in Figure 6.5 over the course of the tearing experiment. Note that in order to discern the shape of the process zone more easily, 10 distinct (not continuous spectrum) colors were used to represent strain values from -0.01 to 0.01. In the initiation stage (Fig. 6.7 a-c), the process zone in front of the crack tip started forming yet stayed small. The size and magnitude of it increased as the maximum nominal stress was reached and crack started to propagate. When the steady-state condition was reached (Fig. 6.7e), the size of the crack tip process zone was large compared to the remaining ligament width, $(w-a)$, and the specimen width, w. (note that the strain maps show the full width of the specimens in Figure 6.7.) At steady-state, a peanut-shaped high (positive) strained zones as well as two smaller (negative) reversed zones on the sides of the crack wake were observed in both MD and CD specimens. Similar characteristics of steady-state process zones have been observed in earlier works, but for small-scale yielding conditions [114–117]. The two key features of the steady-state process zone were found to be a wedge-shaped process zone with a constant half angle, θ_p, and a small reversed plastic zone in the wake of the growing crack. The size and shape of ZAPs at steady-state from three different specimens in each orientation were compared in Figure 6.8. This comparison showed that the characteristics of ZAPs were consistent among same orientation specimens but different across the specimen orientation. The shape of ZAP of MD specimens were long elliptical where that of CD specimens were round and shorter. The reversed zones were less consistent in that the magnitudes of them were higher in some and smaller in others.

In Figure 6.7, we observed that as the crack advanced, the ZAP also moved along with the crack tip and the kept the same shape until it hit the back edge. When the crack tip was closed to the back edge, the ZAP interacted with the back edge and morphed into a wedge

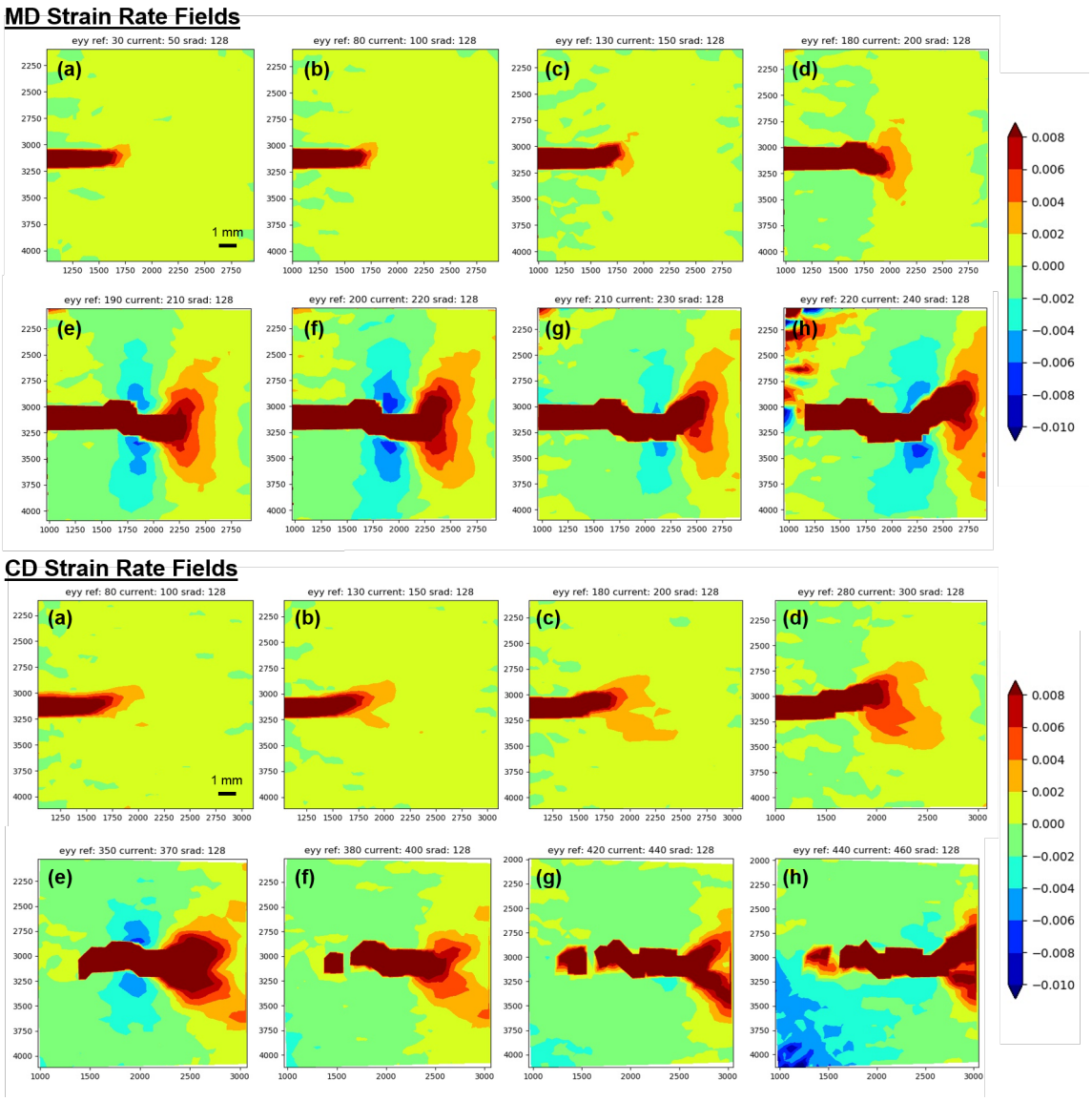

Figure 6.7: Incremental strain maps of of representative MD and CD specimens. The strain maps were reference to 20 images prior to the current image, which corresponds to the crosshead strain of $\Delta\varepsilon = 0.00067$.

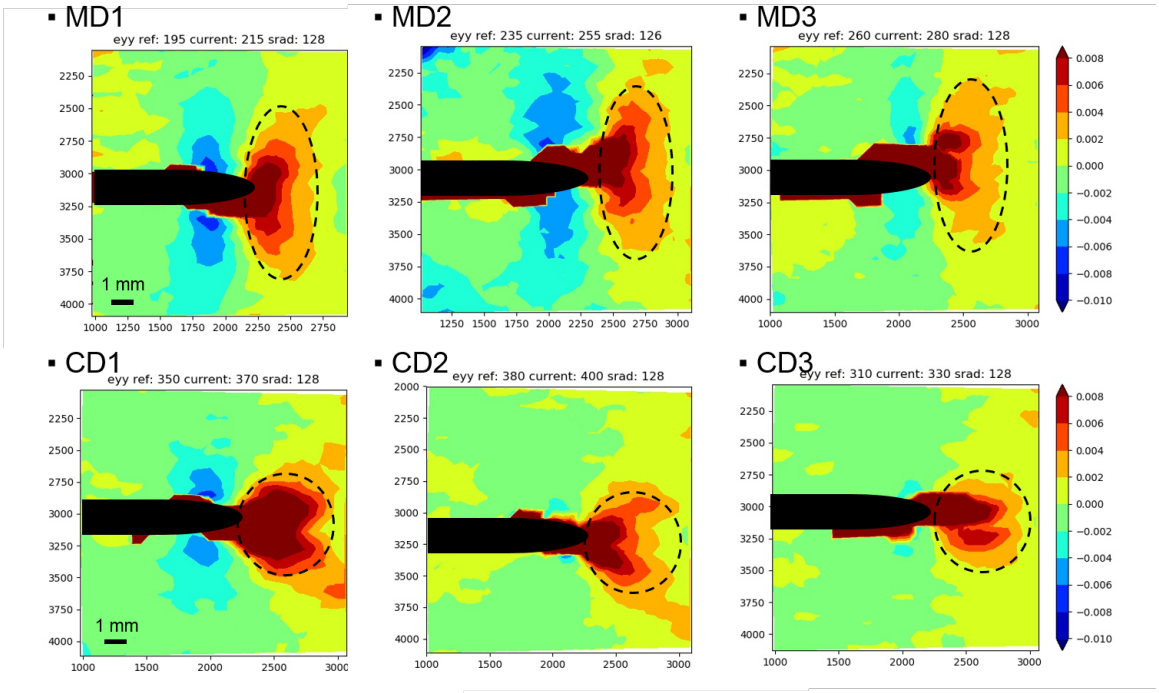

Figure 6.8: Incremental strain maps of 6 different specimens at $a/w = 0.6$. Crack is masked with black color on the left. Dotted black line is arbitrarily drawn on the strain maps to compare sizes of ZAP among different samples.

shape zone. The crack tip process zones are at steady-state if the shape and magnitude of the crack tip strain field remains fixed as the coordinate system (reference frame) translates with the growing crack tip. The size of the ZAP was quantified by measuring the height of the ZAP as shown in Figure 6.9. Here, ZAP boundary was set as the a zone that had strains larger than 0.002. (Note that the yield strains of MD and CD tensile specimens were 0.002 56 and 0.002 82, respectively.) The x positions of the crack tip and the farthest location of the ZAP were divided into three regions. Then, the height of the ZAP (indicated with red arrows) was measured at the one-third location for the MD and two-thirds location for the CD specimens. The height of ZAPs were measured for six specimens from the beginning to the end of the tearing experiment. Figure 6.10 shows change of ZAP height of the six MD and CD specimens measured on incremental strain maps as a function of normalized crack lengths. For the CD specimens, the height of ZAP grew to 4 mm quickly after initiation and remained nearly constant during the crack growth for all three CD spec-

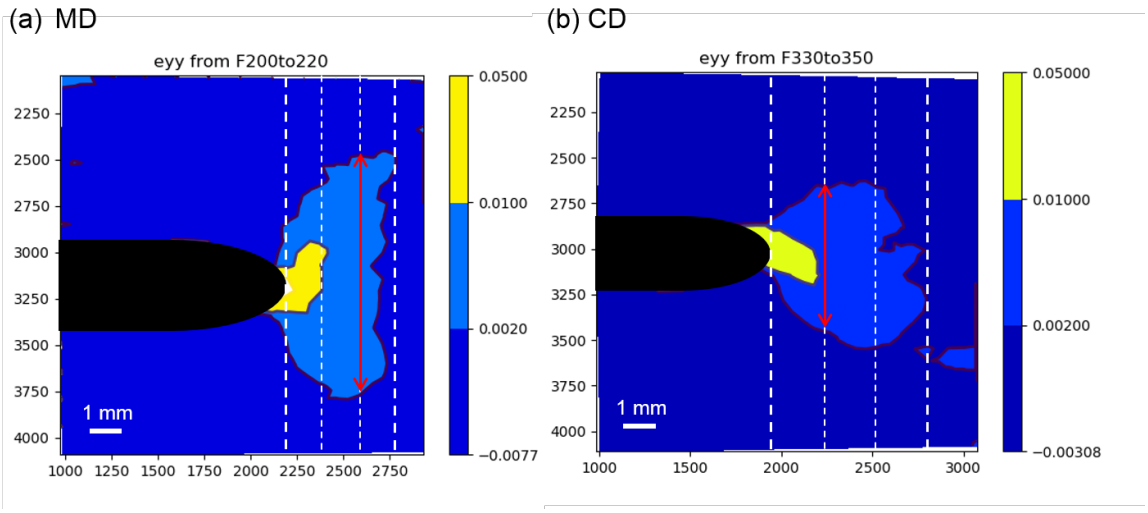

Figure 6.9: A schematic diagram for measuring the size of ZAP

imens. For the MD specimens, the height grew to approximately 8 mm at $a/w = 0.5$ then stayed in between 8 mm to 9 mm for all three MD specimens. Because the size of the ZAP remained constant for some part of (if not all) the propagation region, we concluded that the crack growth in paper is a steady-state process. Moreover, it was found that the zone size and shape were different depending on the specimen orientation and that steady-state was reached faster in the CD specimens than in the MD specimens.

6.3 Conclusions

In this chapter, notched paper specimens with varying notch sizes in two orientations were tested in tension and exhibited steady-state crack growth. We showed that the crack growth in copy paper followed steady-state crack propagation that is similar to that of thin sheet ductile metals. The characteristic steady-state stress (σ_c) and the offset stress (σ_{offset}) were 37.3 MPa and 6.0 MPa for the MD and 20.1 MPa and 2.9 MPa for the CD specimens. The incremental strain maps revealed that there were specimen orientation dependent process zones in front and in the wake of the crack tip. By thresholding strain maps and measuring the height of ZAP, we found that the size of ZAP stayed 4 mm for MD and 9 mm for CD during the steady-state crack growth.

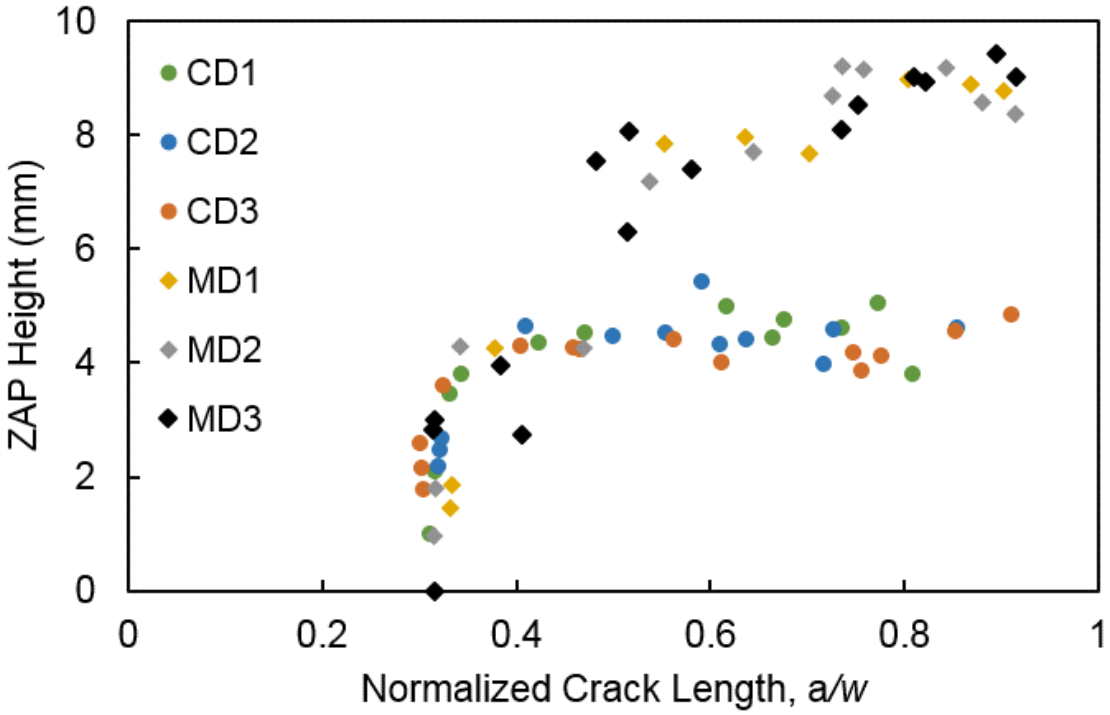

Figure 6.10: Height of ZAP vs. normalized crack lengths for three MD and three CD specimens from the beginning to the end of the tearing experiment.

CHAPTER 7
CONCLUSIONS

The purpose of this work was to use strain field mining to identify strain field structures that were relevant to mechanical behavior of machine-made papers. In the first part of this dissertation (Chapter 3), I introduced the results on using different characterization techniques and how difficult it was to characterize a large volume of heterogeneous network planar structure with details of individual fibers and pores. This chapter demonstrated that the challenges faced during the structural characterization required too much time and resources to overcome. Therefore, in this work, I used a fundamentally different strategy. Instead of focusing on the direct fiber network characterization, structures of the strain fields, which were essentially direct byproducts of structural changes, were identified and used toward making the structure-property relationship in paper. Digital image correlation was used to obtain the strain fields of deforming paper under tensile, fatigue, and tearing experiments; however, the obtained strain fields were interpreted using various strain field mining techniques which then highlighted useful features in the deforming structure. For example, strain hot spots were distinguished from the rest of the strain field by applying the thresholding criteria.

In Chapter 4, tensile deformation fields and strain fields revealed that the tensile deformation of paper was nonaffine, especially in the transverse direction. The sinusoidal movements in the transverse deformation maps were intensified as specimens were loaded and were more pronounced in the CD specimens. This behavior manifested itself as a direct byproduct of a specimen network topography, in which fibers were preferentially aligned in the MD. For example, the Poisson's ratio evolved over the course of tensile loading and it was smaller in the CD specimens (more transverse motion). Specimen failure locations were identified not only in axial strain maps but also in transverse deformation maps. I

found that the fracture initiated from the opposite end of the region where the largest (magnitude) transverse displacement was present. This information could be used to identify which hot spots among many would eventually lead to failure. The transverse deformations were not affine (nonaffinity metric, D, from 0.5 to 3.5), and CD specimens had 3 times higher degree of nonaffinity in the transverse direction than MD specimens. This anisotropic, nonaffine behavior was a result of the fiber orientation relative to the loading direction: the axial deformations were controlled by stretching of axially oriented fibers, and the transverse deformations were from bending and rotation of fibers that are inclined to the loading direction. Moreover, the size of hot spots were initially small but became larger only in the CD specimens, which could also be explained by the anisotropy in the structure.

In Chapter 5, a strain field mining strategy was used to quantify the extent crack growth in notched paper specimens during constant and cyclic stress conditions. The obtained crack growth rates along with the fracture profiles revealed that there was a distinct fatigue damage accumulation mechanism in paper that caused fiber fracture, instead of inter-fiber bond failure and fiber pull-out. Specimens that were subjected to lower cyclic stress amplitudes lived longer fatigue life and exhibited a longer portion of fiber fractured profile, indicated by a clean, sharp fractured surface. Moreover, I discovered that pre-applied creep damage in paper can help delay the upcoming fatigue damage accumulation and extend paper's high cycle fatigue life, possibly due to a structural change at interfiber bonds in the network caused by the prior creep damage. The specimens with prior creep damage lived up to 6.2 times more fatigue life than the fatigue only specimens (i.e., 354 741 cycles vs. 57 329 cycles), and their crack growth rates were an order of magnitude slower (i.e., 3.0×10^{-6} mm/cycle vs. 3.9×10^{-5} mm/cycle).

In Chapter 6, crack tip process zone and zone of active plasticity (ZAP) were examined in the strain fields of the single edge notched tension (SENT) specimens. Surprisingly, the relationship between the applied nominal stresses and normalized crack lengths fol-

lowed the three stage process (initiation, transition, steady-state) that had been previously observed in thin, ductile metal sheets. The relationship was identical except that there was an offset stress (σ_{offset}) at $a/w = 1$ which was induced by the fiber bridging and fiber pull-out. The characteristic steady-state stress (σ_c) and the offset stress (σ_{offset}) of the paper were 37.3 MPa and 6.0 MPa for the MD and 20.1 MPa and 2.9 MPa for the CD specimens. Using strain field mining, I also found that the shape and size of the ZAP in the incremental strain maps stayed constant as the crack grew, which was another proof of the steady-state tearing. Therefore, I found the shape and extent of crack tip damage accumulation in paper and also showed that the transverse necking was not a requirement for the steady-state tearing process in thin sheet materials.

In this dissertation, I have demonstrated that strain field mining was an effective technique for identifying critical regions of the fiber network and their relationships to tensile, fatigue, and fracture deformation mechanisms. The quantitative metrics developed in this dissertation (for characterizing the critical strain field structures) are a crucial step forward in quantifying the structure-processing-property relationships of heterogeneous fiber networks like paper. For example, I showed in section 4.2.5 that two types of linerboards with indistinguishable stress-strain curves had different nonaffinity metric, D, due to their difference in processing parameters. Further investigation on how structural and processing variables control this metric will provide new insights about the relationship between network structure and deformation of paper. This research could be extended to extremely thin, low basis weight papers so that the network architecture is more amenable to 3D characterization. Moreover, the application of this research is not just limited to wood paper products, but it can also be applied to other fiber network thin sheet materials (i.e., nonwoven fabrics, carbon nanofibrils (CNF) papers, buckypapers). It will be especially useful for studying the deformation mechanisms of nanofilament network materials because their long, nanoscale fiber networks are difficult to be fully characterized using conventional characterization techniques.

Appendices

APPENDIX A

FIBER QUALITY ANALYZER TEST RESULT

This report was prepared by the pulp analysis facility at Renewable Bioproducts Institute.

Summary

A paper sample was characterized by using FQA. Fines content, fiber length, kink, curl and fiber width were determined.

Procedure

Paper sample was soaked in cold water overnight. The wet paper sheet was torn into 2x3 cm pieces. The sample was disintegrated in a British disintegrator. Fiber slurry was used for the fiber characterization.

Result

FQA analysis results are tabulated as following.

Sample	Percentage fines, %		Mean Length, mm			Fiber width
	Arithmetic	L.W	Arithmetic	L.W	W. W	μm
Run 1	15.60	2.20	0.696	1.339	2.058	21.6
Run 2	15.40	2.20	0.712	1.379	2.101	21.5
Average	15.50	2.20	0.704	1.359	2.080	21.6
Sample	Mean Curl		Mean kink, 1/mm			
	Arithmetic	L.W	Kink index	Total kink angle, °		kinks/mm
Run 1	0.109	0.121	1.54	30.0		0.73
Run 2	0.108	0.116	1.53	30.4		0.73
Average	0.109	0.119	1.54	30.2		0.73

FQA analysis terminology

Terminology used in FQA analysis is shown as following:

1. Fines: FQA defines an object as a fiber object when its length is above 0.07 mm. Fines are fiber objects whose length is in the range of 0.07 mm to 0.1mm. An arithmetic fine% is calculated as

$$\%F = 100 \times \frac{\sum ni}{N}$$

Where n_i is number i fine, and N is the total fiber objects

Length weighted length fine is calculated as:

$$\%F = 100 \times \frac{\sum niLi}{Lt}$$

Where n_i is number of fines with a length of L_i, L_t is the total fiber length.

2. Fiber length: Fiber length is calculated in three forms:

a. Arithmetic length:

$$Ln = \frac{\sum niLi}{\sum ni}$$

Where: n_i is numbers of fibers with Li length

b. Length Weighted Length (L.W):

$$Lw = \frac{\sum niLi^2}{\sum niLi}$$

c. Weight Weighted Length (L.W.W):

$$Lww = \frac{\sum niLi^3}{\sum niLi^2}$$

3. Mean curl:

$$Cl_{LW} = \frac{\sum Cl_i L_i}{\sum L_i}$$

and Cl_i is defined by the formula:

$$Cl = \frac{L}{l} - 1$$

Where L is contour length (real length) and l is projected length.

4. Kink index:

$$KI = \frac{2N_{(21-45)} + 3N_{(46-90)} + 4N_{(91-180)}}{Lt}$$

So it is the weighted sum of the number, N_x, of kinks within a range of "x" kink angles, divided by the total fiber length of all the fibers.

5. Coarseness:

$$Coarseness = \frac{Mass\ of\ oven\ dry\ fiber\ tested(mg}{Fiber\ total \times Ln(mm) \times (\frac{1m}{1000mm})}$$

APPENDIX B

LINEAL PATH CORRELATION ANALYSIS

This is an example Python code for lineal path correlation analysis using test lines in the horizontal direction ($\theta = 0$).

```
import numpy as np
from operator import truediv
from PIL import Image
import matplotlib.pyplot as plt

img= Image.open('image.png').convert('L')
WIDTH, HEIGHT = img.size
data = list(img.getdata())
data = [data[offset:offset+WIDTH] for offset in range(0,
  ↪ WIDTH*HEIGHT, WIDTH)]
data =np.asarray(data)
row = len(data)
col = len(data[0])

#####For theta =0#####

lm=col
R = np.linspace(0,lm-1,lm)
L00 = np.zeros_like(R)
L11 = np.zeros_like(R)
nan_arr= np.zeros((row,1))

for j in range (0,row):
    restart = True
    i=0
    r=0
    nan=0
    m=[]
    while restart:
        restart =False
        for ii in range (1,lm+1):
            if i==lm:
                continue
```

```
                try:
                    int(data[j,i])
                except ValueError:
                    i=i+1
                    nan=nan+1
                    nan_arr[j]=nan
                    restart =True
                    break
                    continue
                if data[j,i]==0:
                    m=0
                if data[j,i]!=0:
                    m=1
                if i+ii == lm:
                    nan_arr[j]=nan
                    for jj in range (0,r+1):
                        if m==0:
                            L00[jj]=L00[jj]+(r+1-jj)
                        elif m==1:
                            L11[jj]=L11[jj]+(r+1-jj)
                    break
                    continue
                if i+ii < lm and data[j,i]==data[j,i+ii]:
                    r=r+1
                    continue
                if i+ii < lm and not data[j,i]==data[j,i+ii]:
                    i=i+r+1
                    for jj in range (0,r+1):
                        if m==0:
                            L00[jj]=L00[jj]+(r+1-jj)
                        elif m==1:
                            L11[jj]=L11[jj]+(r+1-jj)
                    r=0
                    nan_arr[j]=nan
                    restart=True
                    break
                    continue

Tot_ent = np.zeros_like(nan_arr)
Tot_ct = np.zeros_like(R)

for a in range(0,row):
    Tot_ent[a]=col-nan_arr[a]
    n = int(Tot_ent[a])
    for b in range(0,n):
```

```
        Tot_ct[b]= Tot_ct[b]+ n - b

P00 = truediv(L00,Tot_ct)
P11 = truediv(L11,Tot_ct)
P01 = 1-(P00+P11)

plt.figure(2)
plt.plot(R,P00,'b', label='L00')
plt.plot(R,P11,'r',label='L11')
plt.plot(R,P01,'g',label='L01')
plt.legend()
plt.xlabel('R, distance')
plt.ylabel('Probability')
axes = plt.gca()
axes.set_ylim([0,1])
plt. title('theta=0')

Data_0 = np.zeros((len(R),4))
Data_0[:,0]= R
Data_0[:,1]= P00
Data_0[:,2]= P11
Data_0[:,3]= P01
np.savetxt('Linecorr_0deg.txt', Data_0, fmt='%10.5f',
 ↪ delimiter='\t', header="R \t L00 \t L11 \t L01 " )

plt.show()
```

APPENDIX C

WEIBULL MLE ANALYSIS

```
import scipy.stats as s
import numpy as np
import matplotlib.pyplot as plt

def weib(x,n,a):
    return (a / n) * (x / n)**(a - 1) * np.exp(-(x / n)**a)

from Tkinter import Tk
from tkFileDialog import askopenfilename

Tk().withdraw()
file = askopenfilename()
data = np.loadtxt(file)

x = np.linspace(data.min(), data.max(),100)

(f0, loc, floc, scale) = s.exponweib.fit(data, floc=0, f0=1)
s.weibull_min.fit(data, floc=0)

plt.plot(x, s.exponweib.pdf(x, *s.exponweib.fit(data, 1, 1,
 ↪ scale=02, loc=0)))
_= plt.hist(data, bins=np.linspace(data.min(), data.max(),
 ↪ 100), normed=True, alpha=0.5);

weibull= np.zeros((1,2))
weibull[0,0]=loc
weibull[0,1]=scale

np.savetxt('weibull.txt', weibull, delimiter='\t',
 ↪ header="m\tcharacteristic strength")

plt.show()
```

APPENDIX D

DEGREE OF NONAFFINITY CALCULATION

```
author = "Yoon Joo Na"
programname = "Naffinity"
version = 1.0
update = "11 July 2018"
introtext = "This program takes in tracking files (valid or
 ↪ Traj.txt), compares with ideal values, calculates degree
 ↪ of nonaffinity"

## LIBRARIES
import numpy as np
import matplotlib
import matplotlib.pyplot as plt
from scipy import stats
import math
from numpy.random import normal
from tkFileDialog import askopenfilename
from Tkinter import Tk
from Tkinter import *
import ttk
import tkFileDialog
import tkMessageBox
import os
import glob
import fnmatch
import pandas as pd
import cv2

########################################
########## Global Variables ############
########################################
gridx=[]
gridy=[]
Trajx=[]
Trajy=[]
exx=[]
eyy=[]
left=[]
```

```
right=[]
bottom=[]
xref=[]
yref=[]
displx=[]
disply=[]
u_affine=[]
v_affine=[]
img_no=0
del_u=[]
del_v=[]
ratio_x=[]
ratio_y=[]
spec_no = 'default'

##########################################
########## Command Definitions ###########
##########################################

def Gridfileopen():
    global gridx, gridy

    filename = askopenfilename()
    gridx = pd.read_csv(filename, header=None)      #used
     ↪ pd.read_csv instead of np.loadtxt
    gridxALERT.set("Grid_x Updated.")                #set
     ↪ header=none because the first row was taken as
     ↪ header automatically
    filename2 = askopenfilename()
    gridy = pd.read_csv(filename2, header=None)
    gridyALERT.set("Grid_y Updated.")

def Trajfileopen():
    global Trajx, Trajy

    filename = askopenfilename()
    Trajx = pd.read_csv(filename, delimiter=r"\s+",
     ↪ header=None, skip_blank_lines=True) #spacing
     ↪ delimiter
    TrajxALERT.set("Traj_x Updated.")
    filename2 = askopenfilename()
    Trajy = pd.read_csv(filename2, delimiter=r"\s+",
     ↪ header=None, index_col=False)
    TrajyALERT.set("Traj_y Updated.")
```

```
def Strainfileopen():
    global exx, eyy
    Tk().withdraw()
    filename = askopenfilename()
    exx, eyy = np.loadtxt(filename,
     ↪ delimiter='\t',skiprows=1, usecols=(3,4),
     ↪ unpack=True)
    StrainALERT.set("Full Field Strains Updated (exx,eyy)")

def specimenlocation():
    global left,right,bottom, xref, yref
    left = float(leftedgeENTRY.get())
    leftedgeALERT.set("Left Edge: "+str(left))
    right = float(rightedgeENTRY.get())
    rightedgeALERT.set("Right Edge: "+str(right))
    bottom = float(bottomedgeENTRY.get())
    bottomedgeALERT.set("Bottom Edge: "+str(bottom))
    xref=(left+right)/2      #Transverse reference point is
     ↪ the middle line of specimen (this point should have
     ↪ 0 transverse displacement)
    yref=bottom              #Axial reference point is the
     ↪ bottom line of specimen (this point should have 0
     ↪ axial displacement)

def calculateNA():
    global displx, disply, img_no, u_affine, v_affine,
     ↪ del_u, del_v, ratio_x, ratio_y, spec_no
    img_no=Trajx.shape[1]           #Trajx matrix has shape
     ↪ of <gridpoint#, img#>, here we want number of images
    displx = np.zeros_like(Trajx)
    disply = np.zeros_like(Trajy)
    u_affine = np.zeros_like(Trajx)
    v_affine = np.zeros_like(Trajy)
    del_u = np.zeros_like(Trajx)
    del_v = np.zeros_like(Trajy)
    ratio_x = np.zeros_like(exx)
    ratio_y = np.zeros_like(eyy)

    imgALERT.set("<-input img number out of
     ↪ {}".format(img_no-1))

    for i in range (1,img_no-1): #Calculate displacement
     ↪ values from subtracting original grid locations from
     ↪ tracked grid locations
```

```
#skip column 0, start the loop from 1 because first row
 ↪ displacement will be 0 anyways.
    displx[:,i]=
     ↪ np.array(Trajx.iloc[:,i])-np.array(Trajx.iloc[:,0])
     ↪ #Here, Traj[:,0] is same as grid points (grid
     ↪ location in the first img)
    disply[:,i]=
     ↪ np.array(Trajy.iloc[:,i])-np.array(Trajy.iloc[:,0])
    u_affine[:,i]=
     ↪ list(exx[i]*np.array(np.array(gridx)-xref))
    v_affine[:,i]=
     ↪ list(eyy[i]*np.array(np.array(gridy)-yref))
    del_u[:,i] = displx[:,i]-u_affine[:,i]
    del_v[:,i] = disply[:,i]-v_affine[:,i]

    ratio_x[i]= np.mean(np.absolute(del_u[:,i])/
     ↪ np.mean((np.absolute(u_affine[:,i]))))
    ratio_y[i]= np.mean(np.absolute(del_v[:,i])/
     ↪ np.mean((np.absolute(v_affine[:,i]))))

try:
    if specENTRY.get() != "":
        spec_no = specENTRY.get()
        specALERT.set("Specimen name: "+str(spec_no))
    else:
        specALERT.set("Specimen name: "+str(spec_no))
except ValueError:
    pass

Data = np.zeros((len(eyy),4))
Data[:,0]= eyy
Data[:,1]= np.array(eyy)/max(eyy)
Data[:,2]= ratio_y
Data[:,3]= ratio_x
np.savetxt('DegofNA_'+str(spec_no)+'.txt', Data,
 ↪ delimiter='\t',header="eyy \t eyy/eyy_max \t D_axial
 ↪ \t D_trans")

np.savetxt('del_x_'+str(spec_no)+'.txt', del_u,
 ↪ delimiter='\t')
np.savetxt('del_y_'+str(spec_no)+'.txt', del_v,
 ↪ delimiter='\t')

plt.plot(eyy, ratio_x,
 ↪ marker='.',linestyle='none',label='transverse',color='r')
```

```
    plt.plot(eyy, ratio_y,
     ↪ marker='.',linestyle='none',label='axial',color='b')
    plt.xlabel("Axial Strain")
    plt.ylabel("D, Degree of Nonaffinity")
    plt.legend(loc='best',fontsize=10)
    plt.title(str(spec_no),fontsize=10)

    plt.savefig("NA_{}.png".format(spec_no))
    plt.show()


def loadfiles():
    global gridx, gridy, Trajx, Trajy, exx, eyy, left,
     ↪ right, bottom, xref, yref

    gridx = pd.read_csv('grid_x.txt', header=None) #used
     ↪ pd.read_csv instead of np.loadtxt
    gridy = pd.read_csv('grid_y.txt', header=None)
    Trajx = pd.read_csv('trajx.txt', delimiter=r"\s+",
     ↪ header=None, skip_blank_lines=True)
    Trajy = pd.read_csv('trajy.txt', delimiter=r"\s+",
     ↪ header=None, index_col=False)
    exx, eyy = np.loadtxt('strainVimno.txt',
     ↪ delimiter='\t',skiprows=1, usecols=(3,4),
     ↪ unpack=True)
    left=556
    right=979
    bottom=2021
    xref=(left+right)/2
    yref=bottom
    gridxALERT.set("Grid_x Updated.")
    gridyALERT.set("Grid_y Updated.")
    TrajxALERT.set("Traj_x Updated.")
    TrajyALERT.set("Traj_y Updated.")
    StrainALERT.set("Full Field Strains Updated (exx,eyy)")
    leftedgeALERT.set("Left Edge: "+str(left))
    rightedgeALERT.set("Right Edge: "+str(right))
    bottomedgeALERT.set("Bottom Edge: "+str(bottom))

    print 'gridx, gridy, Trajx, Trajy, exx, eyy, files
     ↪ loaded'
    print 'Specimen locations updated'

def displacementplot():
```

```
plt.subplots(1,6,figsize=(20,8))
plt.tight_layout(pad=4.5, w_pad=3.2, h_pad=1.0)

for j in range (1,img_no-1):
    plt.clf()
    plt.suptitle('displacement vector fields for img{}
     ↪ out of {}'.format(j+1,img_no-1),fontsize=10)

    plt.subplot(1,6,3)
    plt.quiver(gridx, gridy, 0, -1*disply[:,j],
     ↪ np.hypot(0,disply[:,j]), width=0.015)
    plt.axis('equal')
    plt.gca().invert_yaxis()
    plt.colorbar()
    plt.axis('equal')
    plt.title('v_real',fontsize=11)
    plt.locator_params(axis='x', nbins=4)

    plt.subplot(1,6,4)
    plt.quiver(gridx, gridy,displx[:,j],0,
     ↪ np.hypot(displx[:,j],0), width=0.015)
    plt.colorbar()
    plt.axis('equal')
    plt.gca().invert_yaxis()
    plt.title('u_real',fontsize=11)
    plt.locator_params(axis='x', nbins=4)

    plt.subplot(1,6,1)
    plt.quiver(gridx, gridy, 0, -1*v_affine[:,j],
     ↪ np.hypot(0,v_affine[:,j]), width=0.015)
    plt.axis('equal')
    plt.gca().invert_yaxis()
    plt.colorbar()
    plt.axis('equal')
    plt.title('v_aff',fontsize=11)
    plt.locator_params(axis='x', nbins=4)

    plt.subplot(1,6,2)
    plt.quiver(gridx, gridy,u_affine[:,j],0,
     ↪ np.hypot(u_affine[:,j],0), width=0.015)
    plt.colorbar()
    plt.axis('equal')
    plt.gca().invert_yaxis()
    plt.title('u_aff',fontsize=11)
    plt.locator_params(axis='x', nbins=4)
```

```
            plt.subplot(1,6,5)
            plt.quiver(gridx, gridy, 0,-1*v_affine[:,j],
              ↪ np.hypot(0,del_v[:,j]), width=0.015)
            plt.axis('equal')
            plt.gca().invert_yaxis()
            plt.colorbar()
            plt.axis('equal')
            plt.title('v_real-v_aff',fontsize=11)
            plt.locator_params(axis='x', nbins=4)

            plt.subplot(1,6,6)
            plt.quiver(gridx, gridy, u_affine[:,j], 0,
              ↪ np.hypot(del_u[:,j],0), width=0.015)

            plt.axis('equal')
            plt.gca().invert_yaxis()
            plt.colorbar()
            plt.title('u_real-u_aff',fontsize=11)
            plt.locator_params(axis='x', nbins=4)

            if FIG_OPTION.get() == ".png":
                plt.savefig("Dispquiver_{}_{}.png"
                  ↪ .format(spec_no,j+1))
            elif FIG_OPTION.get() == ".eps":
                plt.savefig("Dispquiver_{}_{}.png"
                  ↪ .format(spec_no,j+1))
            elif FIG_OPTION.get() == ".jpg":
                 plt.savefig("Dispquiver_{}_{}.png"
                  ↪ .format(spec_no,j+1))
            print 'figure{}/{} saved'.format(j+1,img_no-1)
            plt.pause(0.0005)

    def specdisplacementplot():
        global img_no
        img=[]
        try:
            if imgENTRY.get() != "":
                img = int(imgENTRY.get())
                imgALERT.set("img{} out of
                  ↪ {}".format(img,img_no-1))
            else:
                imgALERT.set("img{} out of
                  ↪ {}".format(img,img_no-1))
        except ValueError:
```

```
    pass

plt.subplots(1,6,figsize=(20,8))
plt.tight_layout(pad=4.5, w_pad=3.2, h_pad=1.0)
plt.clf()
plt.suptitle('displacement vector fields for img{} out
 ↪ of {}'.format(img,img_no-1),fontsize=10)

plt.subplot(1,6,3)
plt.quiver(gridx, gridy, 0, -1*disply[:,img],
 ↪ np.hypot(0,disply[:,img]), width=0.015)
plt.axis('equal')
plt.gca().invert_yaxis()
plt.colorbar()
plt.axis('equal')
plt.title('v_real',fontsize=11)
plt.locator_params(axis='x', nbins=4)

plt.subplot(1,6,4)
plt.quiver(gridx, gridy,displx[:,img],0,
 ↪ np.hypot(displx[:,img],0), width=0.015)
plt.colorbar()
plt.axis('equal')
plt.gca().invert_yaxis()
plt.title('u_real',fontsize=11)
plt.locator_params(axis='x', nbins=4)

plt.subplot(1,6,1)
plt.quiver(gridx, gridy, 0, -1*v_affine[:,img],
 ↪ np.hypot(0,v_affine[:,img]), width=0.015)
plt.axis('equal')
plt.gca().invert_yaxis()
plt.colorbar()
plt.axis('equal')
plt.title('v_aff',fontsize=11)
plt.locator_params(axis='x', nbins=4)

plt.subplot(1,6,2)
plt.quiver(gridx, gridy,u_affine[:,img],0,
 ↪ np.hypot(u_affine[:,img],0), width=0.015)
plt.colorbar()
plt.axis('equal')
plt.gca().invert_yaxis()
plt.title('u_aff',fontsize=11)
plt.locator_params(axis='x', nbins=4)
```

```
        plt.subplot(1,6,5)
        plt.quiver(gridx, gridy, 0,-1*v_affine[:,img],
          ↪ np.hypot(0,del_v[:,img]), width=0.015)
        plt.axis('equal')
        plt.gca().invert_yaxis()
        plt.colorbar()
        plt.axis('equal')
        plt.title('v_real-v_aff',fontsize=11)
        plt.locator_params(axis='x', nbins=4)

        plt.subplot(1,6,6)
        plt.quiver(gridx, gridy, u_affine[:,img], 0,
          ↪ np.hypot(del_u[:,img],0), width=0.015)
        plt.axis('equal')
        plt.gca().invert_yaxis()
        plt.colorbar()
        plt.title('u_real-u_aff',fontsize=11)
        plt.locator_params(axis='x', nbins=4)
        plt.show()

    def stepdisplacementplot():
        step=1
        try:
            if stepENTRY.get() != "":
                step = int(stepENTRY.get())
                stepALERT.set("disply every {}
                  ↪ images".format(step))
            else:
                imgALERT.set("disply all images")
        except ValueError:
            pass

        plt.subplots(1,6,figsize=(20,8))
        plt.tight_layout(pad=4.5, w_pad=3.2, h_pad=1.0)

        for j in range (1,img_no-1,step):
            plt.clf()
            plt.suptitle('displacement vector fields for img{}
              ↪ out of {}'.format(j+1,img_no-1),fontsize=10)

            plt.subplot(1,6,3)
            plt.quiver(gridx, gridy, 0, -1*disply[:,j],
              ↪ np.hypot(0,disply[:,j]), width=0.015)
            plt.axis('equal')
```

```
plt.gca().invert_yaxis()
plt.colorbar()
plt.axis('equal')
plt.title('v_real',fontsize=11)
plt.locator_params(axis='x', nbins=4)

plt.subplot(1,6,4)
plt.quiver(gridx, gridy,displx[:,j],0,
 ↪ np.hypot(displx[:,j],0), width=0.015)
plt.colorbar()
plt.axis('equal')
plt.gca().invert_yaxis()
plt.title('u_real',fontsize=11)
plt.locator_params(axis='x', nbins=4)

plt.subplot(1,6,1)
plt.quiver(gridx, gridy, 0, -1*v_affine[:,j],
 ↪ np.hypot(0,v_affine[:,j]), width=0.015)
plt.axis('equal')
plt.gca().invert_yaxis()
plt.colorbar()
plt.axis('equal')
plt.title('v_aff',fontsize=11)
plt.locator_params(axis='x', nbins=4)

plt.subplot(1,6,2)
plt.quiver(gridx, gridy,u_affine[:,j],0,
 ↪ np.hypot(u_affine[:,j],0), width=0.015)
plt.colorbar()
plt.axis('equal')
plt.gca().invert_yaxis()
plt.title('u_aff',fontsize=11)
plt.locator_params(axis='x', nbins=4)

plt.subplot(1,6,5)
plt.quiver(gridx, gridy, 0,-1*v_affine[:,j],
 ↪ np.hypot(0,del_v[:,j]), width=0.015)
plt.axis('equal')
plt.gca().invert_yaxis()
plt.colorbar()
plt.axis('equal')
plt.title('v_real-v_aff',fontsize=11)
plt.locator_params(axis='x', nbins=4)

plt.subplot(1,6,6)
```

```
            plt.quiver(gridx, gridy, u_affine[:,j], 0,
              ↪ np.hypot(del_u[:,j],0), width=0.015)
            plt.axis('equal')
            plt.gca().invert_yaxis()
            plt.colorbar()
            plt.title('u_real-u_aff',fontsize=11)
            plt.locator_params(axis='x', nbins=4)

            if FIG_OPTION.get() == ".png":
                plt.savefig("Dispquiver_{}_{}.png"
                  ↪ .format(spec_no,j+1))
            elif FIG_OPTION.get() == ".eps":
                plt.savefig("Dispquiver_{}_{}.png"
                  ↪ .format(spec_no,j+1))
            elif FIG_OPTION.get() == ".jpg":
                 plt.savefig("Dispquiver_{}_{}.png"
                   ↪ .format(spec_no,j+1))
            print 'figure{}/{} saved'.format(j+1,img_no-1)
            plt.pause(0.0005)


########################################
############## BEGIN GUI ###############
########################################

root = Tk()
root.title("{0} {1}".format(programname,version))
mainframe = ttk.Frame(root, padding="3 3 12 12")
mainframe.grid(column=0, row=0, sticky=(N, W, E, S))
mainframe.columnconfigure(0, weight=1)
mainframe.rowconfigure(0, weight=1)

#row 0-1: Introduction
ttk.Label(mainframe, text='Created by:'+author+' /Last
 ↪ updated: '+update).grid(row=1, column=3,columnspan=3,
 ↪ sticky='E')
ttk.Label(mainframe, text=introtext).grid(row=0, column=0,
 ↪ columnspan=6, sticky='EW')

#row 2: Data File
ttk.Label(mainframe, text='1. Open Data Files',
 ↪ background='orange').grid(row=2, column=0, columnspan=6,
 ↪ sticky=W+E)

#row 3-5: Open data files
```

```
ttk.Button(mainframe, text="Open 'grid_x' and 'grid_y'
 ↪ files", command=Gridfileopen).grid(row=3, column=0,
 ↪ columnspan=2, sticky=(W,E))
gridxALERT = StringVar()
gridxALERT.set("Not Opened.")
ttk.Label(mainframe, textvariable=gridxALERT).grid(row=3,
 ↪ column=2, sticky=W)
gridyALERT = StringVar()
gridyALERT.set("Not Opened.")
ttk.Label(mainframe, textvariable=gridyALERT).grid(row=3,
 ↪ column=3, sticky=W)
ttk.Button(mainframe, text="Open 'Trajx' and 'Trajy' files",
 ↪ command=Trajfileopen).grid(row=4, column=0,
 ↪ columnspan=2, sticky=(W,E))
TrajxALERT = StringVar()
TrajxALERT.set("Not Opened.")
ttk.Label(mainframe, textvariable=TrajxALERT).grid(row=4,
 ↪ column=2, sticky=W)
TrajyALERT = StringVar()
TrajyALERT.set("Not Opened.")
ttk.Label(mainframe, textvariable=TrajyALERT).grid(row=4,
 ↪ column=3, sticky=W)
ttk.Button(mainframe, text="Open 'StrainVimno' file",
 ↪ command=Strainfileopen).grid(row=5, column=0,
 ↪ columnspan=2, sticky=(W,E))
StrainALERT = StringVar()
StrainALERT.set("Not Opened.")
ttk.Label(mainframe, textvariable=StrainALERT).grid(row=5,
 ↪ column=2, columnspan=3, sticky=W)

#row 6-11: Enter Specimen Information
ttk.Label(mainframe, text='2. Enter Specimen Location',
 ↪ background='orange').grid(row=6, column=0, columnspan=6,
 ↪ sticky=W+E)
ttk.Label(mainframe, text=' *  In this setup, specimen is
 ↪ placed vertically and pulled upward').grid(row=7,
 ↪ column=0, columnspan=6, sticky='EW')
ttk.Button(mainframe, text="Update Specimen Location",
 ↪ command=specimenlocation).grid(row=11,
 ↪ column=0,columnspan=2, sticky=(W,E))
leftedgeENTRY = StringVar()
rightedgeENTRY = StringVar()
bottomedgeENTRY = StringVar()
leftedgeALERT = StringVar()
rightedgeALERT = StringVar()
```

```
bottomedgeALERT = StringVar()
ttk.Entry(mainframe, width = 10, textvariable =
 ↪ leftedgeENTRY).grid(row=8, column=0,
 ↪ columnspan=2,sticky=W+E)
ttk.Entry(mainframe, width = 10, textvariable =
 ↪ rightedgeENTRY).grid(row=9, column=0,
 ↪ columnspan=2,sticky=W+E)
ttk.Entry(mainframe, width = 10, textvariable =
 ↪ bottomedgeENTRY).grid(row=10, column=0,
 ↪ columnspan=2,sticky=W+E)
leftedgeALERT.set("<-input location of left edge of
 ↪ specimen")
rightedgeALERT.set("<-input location of right edge of
 ↪ specimen")
bottomedgeALERT.set("<-input location of bottom edge of
 ↪ specimen")
ttk.Label(mainframe, textvariable=leftedgeALERT).grid(row=8,
 ↪ column=2, columnspan=2, sticky=W)
ttk.Label(mainframe,
 ↪ textvariable=rightedgeALERT).grid(row=9, column=2,
 ↪ columnspan=2, sticky=W)
ttk.Label(mainframe,
 ↪ textvariable=bottomedgeALERT).grid(row=10, column=2,
 ↪ columnspan=2, sticky=W)

#row 12-14: Calculate
ttk.Label(mainframe, text='3. Calculate Nonaffinity',
 ↪ background='orange').grid(row=12, column=0,
 ↪ columnspan=6, sticky=W+E)
specENTRY = StringVar()
specALERT = StringVar()
ttk.Entry(mainframe, width = 10, textvariable =
 ↪ specENTRY).grid(row=13, column=0, columnspan=2,
 ↪ sticky=W+E)
specALERT.set("<-input specimen name")
ttk.Label(mainframe, textvariable=specALERT).grid(row=13,
 ↪ column=2, columnspan=2, sticky=W)
ttk.Button(mainframe, text="Calculate Nonaffinity!",
 ↪ command=calculateNA).grid(row=14, column=0,columnspan=2,
 ↪ sticky=(W,E))

#row 15-16 :Plot/save Displacement fields
ttk.Label(mainframe, text='4. Plot Displacement Fields',
 ↪ background='orange').grid(row=15, column=0,
 ↪ columnspan=6, sticky=W+E)
```

```
# Drop-down menu
figoption = [".png",".eps",".jpg"]
FIG_OPTION = StringVar()
ttk.OptionMenu(mainframe, FIG_OPTION, figoption[0],
 ↪ *tuple(figoption)).grid(row=16, column=2, sticky=(W, E))
ttk.Button(mainframe, text="Plot & Save All Displacement
 ↪ Fields", command=displacementplot).grid(row=16,
 ↪ column=0,columnspan=2, sticky=(W,E))
ttk.Button(mainframe, text="Show Specific Displacement
 ↪ Fields", command=specdisplacementplot).grid(row=17,
 ↪ column=0,columnspan=2, sticky=(W,E))
imgENTRY = StringVar()
imgALERT = StringVar()
ttk.Entry(mainframe, width = 10, textvariable =
 ↪ imgENTRY).grid(row=17, column=2, columnspan=1,
 ↪ sticky=W+E)
imgALERT.set("<-input img number")
ttk.Label(mainframe, textvariable=imgALERT).grid(row=17,
 ↪ column=3, columnspan=2, sticky=W)
ttk.Button(mainframe, text="Plot & Save Every x Displacement
 ↪ Fields", command=stepdisplacementplot).grid(row=18,
 ↪ column=0,columnspan=2, sticky=(W,E))
stepENTRY = StringVar()
stepALERT = StringVar()
ttk.Entry(mainframe, width = 10, textvariable =
 ↪ stepENTRY).grid(row=18, column=2, columnspan=1,
 ↪ sticky=W+E)
stepALERT.set("<-input step size")
ttk.Label(mainframe, textvariable=stepALERT).grid(row=18,
 ↪ column=3, columnspan=2, sticky=W)

#row 19-21 :For developer
ttk.Label(mainframe, text=' ' ).grid(row=19, column=0,
 ↪ columnspan=6, sticky=W+E)
ttk.Label(mainframe, text='Program Development Option',
 ↪ background='orange').grid(row=20, column=0,
 ↪ columnspan=6, sticky=W+E)
ttk.Button(mainframe, text="Load Files for Debugging",
 ↪ command=loadfiles).grid(row=21, column=0,columnspan=2,
 ↪ sticky=(W,E))
for child in mainframe.winfo_children():
 ↪ child.grid_configure(padx=1, pady=2)

root.mainloop()
```

REFERENCES

[1] W. W. Sampson, "Materials properties of paper as influenced by its fibrous architecture," *International Materials Reviews*, vol. 54, no. 3, pp. 134–156, 2009.

[2] M. Alava and K. Niskanen, "The physics of paper," *Reports on Progress in Physics*, vol. 69, no. 3, pp. 669–723, 2006.

[3] R. Brown, "Forest products industry technology roadmap," Tech. Rep., 2010.

[4] H. W. Haslach, "The moisture and rate-dependent mechanical properties of paper: A review," *Mechanics of Time-Dependent Materials*, vol. 4, no. 3, pp. 169–210, 2000.

[5] K. Niskanen, *Mechanics of paper products*. Berlin: De Gruyter, 2012.

[6] G. A. Baum, "The elastic properties of paper: A review," in *IPC Technical Paper Series; no.145*, Institute of Paper Chemistry, 1984, pp. 1–21.

[7] P. Makela and S. Ostlund, "Orthotropic elastic-plastic material model for paper materials," *International Journal of Solids and Structures*, vol. 40, no. 21, pp. 5599–5620, 2003.

[8] P. Vannucci, "On special orthotropy of paper," *Journal of Elasticity*, vol. 99, no. 1, pp. 75–83, 2010.

[9] *Paper physics*, 2nd ed., ser. Papermaking Science and Technology. Finland: Paperi ja Puu Oy, 2008.

[10] R. C. Picu, "Mechanics of random fiber networks-a review," *Soft Matter*, vol. 7, no. 15, pp. 6768–6785, 2011.

[11] M. Rigdahl, H. Andersson, B. Westerlind, and H. Hollmark, "Elastic behavior of low-density paper described by network mechanics," *Fibre Science and Technology*, vol. 19, no. 2, pp. 127–144, 1983.

[12] H. L. Cox, "The elasticity and strength of paper and other fibrous materials," *British Journal of Applied Physics*, vol. 3, no. Mar, pp. 72–79, 1952.

[13] K. Schulgasser, "The inplane poisson ratio of paper," *Fibre Science and Technology*, vol. 19, no. 4, pp. 297–309, 1983.

[14] D. H. Page, R. S. Seth, and J. H. Degrace, "Elastic-modulus of paper .1. controlling mechanisms," *Tappi*, vol. 62, no. 9, pp. 99–102, 1979.

[15] D. H. Page and R. S. Seth, "The elastic-modulus of paper .2. the importance of fiber modulus, bonding, and fiber length," *Tappi*, vol. 63, no. 6, pp. 113–116, 1980.

[16] J. Wilhelm and E. Frey, "Elasticity of stiff polymer networks," *Physical Review Letters*, vol. 91, no. 10, 2003.

[17] Q. S. Xia, M. C. Boyce, and D. M. Parks, "A constitutive model for the anisotropic elastic-plastic deformation of paper and paperboard," *International Journal of Solids and Structures*, vol. 39, no. 15, pp. 4053–4071, 2002.

[18] C. A. Bronkhorst, "Modelling paper as a two-dimensional elastic-plastic stochastic network," *International Journal of Solids and Structures*, vol. 40, no. 20, pp. 5441–5454, 2003.

[19] H. Kallmes O.; Corte, "The structure of paper i. the statistical geometry of an ideal two dimensional fiber network," *Tappi*, vol. 43, no. 9, 1960.

[20] M. Ostoja-Starzewski and D. C. Stahl, "Random fiber networks and special elastic orthotropy of paper," *Journal of Elasticity*, vol. 60, no. 2, pp. 131–149, 2000.

[21] C. Antoine, P. Nygard, O. W. Gregersen, R. Holmstad, T. Weitkamp, and C. Rau, "3d images of paper obtained by phase-contrast x-ray micro tomography: Image quality and binarisation," *Nuclear Instruments and Methods in Physics Research Section a-Accelerators Spectrometers Detectors and Associated Equipment*, vol. 490, no. 1-2, pp. 392–402, 2002.

[22] Y. Sharma, A. B. Phillion, and D. M. Martinez, "Automated segmentation of wood fibres in micro-ct images of paper," *Journal of Microscopy*, vol. 260, no. 3, pp. 400–410, 2015.

[23] M. Hasuike, T. Kawasaki, and K. Murakami, "Evaluation method of 3-d geometric structure of paper sheet," *Journal of Pulp and Paper Science*, vol. 18, no. 3, J114–J120, 1992.

[24] M. Aronsson, O. Henningsson, and O. Savborg, "Slice-based digital volume assembly of a small paper sample," *Nordic Pulp and Paper Research Journal*, vol. 17, no. 1, pp. 29–33, 2002.

[25] M. Wiltsche, M. Donoser, W. Bauer, and H. Bischof, "A new slice-based concept for 3d paper structure analysis applied to spatial coating layer formation," *Advances in Paper Science and Technology: Transactions of the 13th Fundamental Research Symposium, Vols 1-3*, pp. 853–899, 2005.

[26] G. J. Williams and J. G. Drummond, "Preparation of large sections for the microscopical study of paper structure," *Journal of Pulp and Paper Science*, vol. 26, no. 5, pp. 188–193, 2000.

[27] A. R. Dickson, "Quantitative analysis of paper cross-sections," *Appita Journal*, vol. 53, no. 4, pp. 292–295, 2000.

[28] A. Goel, M. Tzanakakis, S. Y. Huang, S. Ramaswamy, D. Choi, and B. V. Ramarao, "Characterization of three-dimensional structure of paper using x-ray microtomography," *Tappi Journal*, vol. 84, no. 5, pp. 72–72, 2001.

[29] J. H. He, W. J. Batchelor, R. Markowski, and R. E. Johnston, "A new approach for quantitative analysis of paper structure at the fibre level," *Appita Journal*, vol. 56, no. 5, pp. 366–370, 2003.

[30] Y. Ozaki, D. W. Bousfield, and S. M. Shaler, "Three-dimensional observation of coated paper by confocal laser scanning microscope," *Tappi Journal*, vol. 5, no. 2, pp. 3–8, 2006.

[31] Y. Defrenne, V. Zhdankin, S. Ramanna, S. Ramaswamy, and B. V. Ramarao, "Three-dimensional pore structure visualization and characterization of paper using x-ray computed tomography," *Tappi Journal*, vol. 16, no. 9, pp. 519–530, 2017.

[32] M. Axelsson and S. Svensson, "3d pore structure characterisation of paper," *Pattern Analysis and Applications*, vol. 13, no. 2, pp. 159–172, 2010.

[33] G. J. Williams, J. G. Drummond, and H. A. Cisneros, "A microscopic approach for examining fiber and paper structures," *Journal of Pulp and Paper Science*, vol. 20, no. 4, J110–J114, 1994.

[34] A. R. Dickson, "The quantitative microscopic analysis of paper cross-sections: Sample preparation effects," *Appita Journal*, vol. 53, no. 5, pp. 362–366, 2000.

[35] E. J. Samuelsen, O. W. Gregersen, P. J. Houen, T. Helle, C. Raven, and A. Snigirev, "Three-dimensional imaging of paper by use of synchrotron x-ray microtomography," *Journal of Pulp and Paper Science*, vol. 27, no. 2, pp. 50–53, 2001.

[36] L. Wong, M. T. Kortschot, and C. T. J. Dodson, "Effect of formation on local strain fields and fracture of paper," *Journal of Pulp and Paper Science*, vol. 22, no. 6, J213–J219, 1996.

[37] M. B. Lyne and R. Hazell, "Formation testing as a means of monitoring strength uniformity," in *The Fundamental Properties of Paper Related to its Uses*, C. Dodson and F. Bolam, Eds., Technical Division Br paper Board Industry Federation, 1976, pp. 74–100.

[38] Y. J. Chao and M. A. Sutton, "Measurement of strains in a paper tensile specimen using computer vision and digital image correlation. part 2: Tensile specimen test," *Tappi Journal*, vol. 71, no. 4, pp. 153–156, 1988.

[39] M. A. Sutton and Y. J. Chao, "Measurement of strains in a paper tensile specimen using computer vision and digital image correlation. part 1: Data acquisition and image-analysis system," *Tappi Journal*, vol. 71, no. 3, pp. 173–175, 1988.

[40] T. H. D. Ting, R. E. Johnston, and W. K. Chiu, "Confocal laser scanning microscope imaging of network changes in unbeaten handsheets under in-plane tensile elongation," *Appita Journal*, vol. 51, no. 4, pp. 281–286, 1998.

[41] J. M. Considine, C. T. Scott, R. Gleisner, and J. Y. Zhu, "Use of digital image correlation to study the local deformation field of paper and paperboard," in *Advances in Paper Science and Technology: 13th Fundamental Research Symposium*, The Pulp and Paper Fundamental Research Society, 2005, pp. 613–630.

[42] S. Borodulina, A. Kulachenko, S. Galland, and M. Nygards, "Stress-strain curve of paper revisited," *Nordic Pulp and Paper Research Journal*, vol. 27, no. 2, pp. 318–328, 2012.

[43] H. Tomimasu, D. Kim, M. Suk, and P. Luner, "Comparison of 4 paper imaging techniques - beta-radiography, electrography, light transmission, and soft x-radiography," *Tappi Journal*, vol. 74, no. 7, pp. 165–176, 1991.

[44] TAPPI, *Fiber analysis of paper and paperboard, tappi/ansi test method t 401 om-15*, 2015.

[45] TAPPI, *T494 tensile properties of paper and paperboard (using constant rate of elongation apparatus)*, 2006.

[46] TAPPI, *T402 standard conditioning and testing atmospheres for paper, board, pulp handsheets, and related products*, 2013.

[47] M. A. Sutton, W. J. Wolters, W. H. Peters, W. F. Ranson, and S. R. McNeill, "Determination of displacements using an improved digital correlation method," *Image and Vision Computing*, vol. 1, no. 3, pp. 133–139, 1983.

[48] J. G. Collins, G. P. Dillon, E. C. Strauch, W. R. Lanning, and C. L. Muhlstein, "Correlating bonded joint deformation with failure using a free surface strain field mining methodology," *Fatigue and Fracture of Engineering Materials and Structure*, vol. 39, pp. 1124–1137, 2016.

[49] M. A. Sutton, M. Q. Cheng, W. H. Peters, Y. J. Chao, and S. R. Mcneill, "Application of an optimized digital correlation method to planar deformation analysis," *Image and Vision Computing*, vol. 4, no. 3, pp. 143–150, 1986.

[50] A. R. Spurr, "A low-viscosity epoxy resin embedding medium for electron microscopy," *Journal of Ultrastructure Research*, vol. 26, no. 1-2, pp. 31–43, 1969.

[51] ASTM, *E111 standard test method for young's modulus, tangent modulus, and chord modulus*, ser. Annual Book of ASTM Standards. West Conshohocken, PA: ASTM, 2010.

[52] ASTM, *C1557 standard test method fortensile strength and youngs modulus of fibers*, ser. Annual Book of ASTM Standards. West Conshohocken, PA: ASTM, 2011, single fiber tensile testing- modulus and strength.

[53] T. Munz D.; Fett, "Ceramics : Mechanical properties, failure behaviour, materials selection," in *Ceramics*. Springer, 1999, ch. 8, pp. 137–158.

[54] R. Danzer, P. Supancic, J. Pascual, and T. Lube, "Fracture statistics of ceramics - weibull statistics and deviations from weibull statistics," *Engineering Fracture Mechanics*, vol. 74, no. 18, pp. 2919–2932, 2007.

[55] H. Singh, A. M. Gokhale, S. I. Lieberman, and S. Tamirisakandala, "Image based computations of lineal path probability distributions for microstructure representation," *Materials Science and Engineering a-Structural Materials Properties Microstructure and Processing*, vol. 474, no. 1-2, pp. 104–111, 2008.

[56] A. Tewari, A. M. Gokhale, J. E. Spowart, and D. B. Miracle, "Quantitative characterization of spatial clustering in three-dimensional microstructures using two-point correlation functions," *Acta Materialia*, vol. 52, no. 2, pp. 307–319, 2004.

[57] W. R. Lanning, "The steady-statework density gradient: A new parameter and strategies for characterizing crack propagation in thin ductile sheets," PhD thesis, 2018.

[58] ASTM, *E 647 standard test method for measurement of fatigue crack growth rates*, ser. Annual Book of ASTM Standards. West Conshohocken, PA: ASTM, 2001, vol. 03.01, pp. 557–593.

[59] J. P. Bernie and W. J. M. Douglas, "Local grammage distribution and formation of paper by light transmission image analysis," *Tappi Journal*, vol. 79, no. 1, pp. 193–202, 1996.

[60] M. Bouydain, J. F. Colom, R. Navarro, and J. Pladellorens, "Determination of paper formation by fourier analysis of light transmission images," *Appita Journal*, vol. 54, no. 2, pp. 103–105, 2001.

[61] A. Hladnik, T. Muck, M. Stanic, and M. Cernic, "Fast fourier transform in papermaking and printing: Two application examples," *Acta Polytechnica Hungarica*, vol. 9, no. 5, pp. 155–166, 2012.

[62] C. A. Schneider, W. S. Rasband, and K. W. Eliceiri, "Nih image to imagej: 25 years of image analysis," *Nature Methods*, vol. 9, no. 7, pp. 671–675, 2012.

[63] A. R. Spurr and W. M. Harris, "Ultrastructure of chloroplasts and chromoplasts in capsicum annuum .i. thylakoid membrane changes during fruit ripening," *American Journal of Botany*, vol. 55, no. 10, pp. 1210–1224, 1968.

[64] R. E. Mark, M. B. Lyne, J. Borch, and C. Habeger, *Handbook of physical testing of paper*, 2nd ed. Taylor and Francis, Inc., 2001, vol. 1, p. 1040.

[65] Y. Na and C. Muhlstein, "Relating nonuniform deformations to fracture in uniaxially loaded non-woven fiber networks," *Experimental Mechanics*, 2019.

[66] G. A. Baum, D. C. Brennan, and C. C. Habeger, "Orthotropic elastic-constants of paper," *Tappi Journal*, vol. 64, no. 8, pp. 97–101, 1981.

[67] W. Weibull, "A statistical distribution function of wide applicability," *Journal of Applied Mechanics-Transactions of the Asme*, vol. 18, no. 3, pp. 293–297, 1951.

[68] P. Zinck, M. F. Pays, R. Rezakhanlou, and J. F. Gerard, "Mechanical characterisation of glass fibres as an indirect analysis of the effect of surface treatment," *Journal of Materials Science*, vol. 34, no. 9, pp. 2121–2133, 1999.

[69] M. Korteoja, L. I. Salminen, K. J. Niskanen, and M. J. Alava, "Strength distribution in paper," *Materials Science and Engineering a-Structural Materials Properties Microstructure and Processing*, vol. 248, no. 1-2, pp. 173–180, 1998.

[70] D. T. Hristopulos and T. Uesaka, "Structural disorder effects on the tensile strength distribution of heterogeneous brittle materials with emphasis on fiber networks," *Physical Review B*, vol. 70, no. 6, 2004.

[71] M. J. Korteoja, A. Lukkarinen, K. Kaski, D. E. Gunderson, J. L. Dahlke, and K. J. Niskanen, "Local strain fields in paper," *Tappi Journal*, vol. 79, no. 4, pp. 217–223, 1996.

[72] T. Uesaka, K. Murakami, and R. Imamura, "Biaxial tensile behavior of paper," *Tappi Journal*, vol. 62, no. 8, pp. 111–114, 1979.

[73] G. N. Greaves, A. L. Greer, R. S. Lakes, and T. Rouxel, "Poisson's ratio and modern materials," *Nature Materials*, vol. 10, no. 11, pp. 823–837, 2011.

[74] P. H. Mott and C. M. Roland, "Limits to poisson's ratio in isotropic materials," *Physical Review B*, vol. 80, no. 13, p. 132 104, 2009.

[75] P. Boulanger and M. Hayes, "Poisson's ratio for orthorhombic materials," *Journal of Elasticity*, vol. 50, no. 1, pp. 87–89, 1998.

[76] T. C. T. Ting and T. Chen, "Poisson's ratio for anisotropic elastic materials can have no bounds," *The Quarterly Journal of Mechanics and Applied Mathematics*, vol. 58, no. 1, pp. 73–82, 2005.

[77] W. Szewczyk, "Determination of poisson's ratio in the plane of the paper," *Fibres and Textiles in Eastern Europe*, vol. 16, no. 4, pp. 117–120, 2008.

[78] C. W. Smith, R. J. Wootton, and K. E. Evans, "Interpretation of experimental data for poisson's ratio of highly nonlinear materials," *Experimental Mechanics*, vol. 39, no. 4, pp. 356–362, 1999.

[79] R. Hill, "The elastic behaviour of a crystalline aggregate," *Proceedings of the Physical Society of London Section A*, vol. 65, no. 389, pp. 349–355, 1952.

[80] R. Hill, "Elastic properties of reinforced solids - some theoretical principles," *Journal of the Mechanics and Physics of Solids*, vol. 11, no. 5, pp. 357–372, 1963.

[81] C. Huet, "Application of variational concepts to size effects in elastic heterogeneous bodies," *Journal of the Mechanics and Physics of Solids*, vol. 38, no. 6, pp. 813–841, 1990.

[82] S. Hazanov and C. Huet, "Order relationships for boundary-conditions effect in heterogeneous bodies smaller than the representative volume," *Journal of the Mechanics and Physics of Solids*, vol. 42, no. 12, pp. 1995–2011, 1994.

[83] S. Hazanov, "On micromechanics of imperfect interfaces in heterogeneous bodies smaller than the representative volume," *International Journal of Engineering Science*, vol. 37, no. 7, pp. 847–861, 1999.

[84] D. A. Head, A. J. Levine, and F. C. MacKintosh, "Distinct regimes of elastic response and deformation modes of cross-linked cytoskeletal and semiflexible polymer networks," *Physical Review E*, vol. 68, no. 6, p. 061 907, 2003.

[85] P. R. Onck, T. Koeman, T. van Dillen, and E. van der Giessen, "Alternative explanation of stiffening in cross-linked semiflexible networks," *Physical Review Letters*, vol. 95, no. 17, 2005.

[86] H. Hatami-Marbini and R. C. Picu, "Scaling of nonaffine deformation in random semiflexible fiber networks," *Physical Review E*, vol. 77, no. 6, p. 062 103, 2008.

[87] J. A. Bristow and P. Kolseth, *Paper structure and properties*. New York: M Dekker, 1986, x, 390 p.

[88] R. Hagglund and P. Isaksson, "Mechanical analysis of folding induced failure in corrugated board: A theoretical and experimental comparison," *Journal of Composite Materials*, vol. 42, no. 9, pp. 889–908, 2008.

[89] D. W. Coffin, "The creep response of paper," *Advances in Paper Science and Technology: Transactions of the 13th Fundamental Research Symposium, Vols 1-3*, pp. 651–747, 2005.

[90] D. W. Coffin, "Use of the efficiency factor to account for previous straining on the tensile behavior of paper," *Nordic Pulp and Paper Research Journal*, vol. 27, no. 2, pp. 305–312, 2012.

[91] N. Ohno, "Recent topics in constitutive modeling of cyclic plasticity and viscoplasticity," *Applied Mechanics Reviews*, vol. 43, no. 11, pp. 283–295, 1990.

[92] G. Kang, "Ratchetting: Recent progresses in phenomenon observation, constitutive modeling and application," *International Journal of Fatigue*, vol. 30, no. 8, pp. 1448–1472, 2008.

[93] A. Miksic, J. Koivisto, E. Mykkanen, J. Saarenpaa, M. Alava, K. Mustonen, P. Karppinen, T. Karppinen, and E. Haeggstrom, "Deformation, acoustic emission and ultrasound velocity during fatigue tests on paper," *Icem 14: 14th International Conference on Experimental Mechanics, Vol 6*, vol. 6, 2010.

[94] A. Miksic, J. Koivisto, and M. Alava, "Statistical properties of low cycle fatigue in paper," *Journal of Statistical Mechanics-Theory and Experiment*, 2011.

[95] A. Miksic, J. Koivisto, J. Rosti, and M. Alava, "Strain fluctuations from dic technique applied on paper under fatigue or creep," *11th International Conference on the Mechanical Behavior of Materials*, vol. 10, 2011.

[96] L. Viitanen, M. Ovaska, S. K. Ram, M. J. Alava, and P. Karppinen, "Predicting creep failure from cracks in a heterogeneous material using acoustic emission and speckle imaging," *Physical Review Applied*, vol. 11, no. 2, p. 024 014, 2019.

[97] S. Suresh, *Fatigue of materials*, 2nd. Cambridge, England: Cambridge University Press, 2003.

[98] W. R. Lanning, S. S. Javaid, and C. L. Muhlstein, "Reconciling fracture toughness parameter contradictions in thin ductile metal sheets," *Fatigue and Fracture of Engineering Materials and Structures*, vol. 40, no. 11, pp. 1809–1824, 2017.

[99] P. Makela and C. Fellers, "An analytic procedure for determination of fracture toughness of paper materials," *Nordic Pulp and Paper Research Journal*, vol. 27, no. 2, pp. 352–360, 2012.

[100] D. Swinehart and D. Broek, "Tenacity and fracture-toughness of paper and board," *Journal of Pulp and Paper Science*, vol. 21, no. 11, J389–J397, 1995.

[101] P. Wellmar, C. Fellers, F. Nilsson, and L. Delhage, "Crack-tip characterization in paper," *Journal of Pulp and Paper Science*, vol. 23, no. 6, J269–J276, 1997.

[102] P. Wellmar, O. W. Gregersen, and C. Fellers, "Prediction of crack growth initiation in paper structures using a j-integral criterion," *Nordic Pulp and Paper Research Journal*, vol. 15, no. 1, pp. 4–11, 2000.

[103] R. S. Seth, A. G. Robertson, Y. W. Mai, and J. D. Hoffmann, "Plane-stress fracture-toughness of paper," *Tappi Journal*, vol. 76, no. 2, pp. 109–116, 1993.

[104] T. Yuhara and M. T. Kortschot, "A simplified determination of the j-integral for paper," *Journal of Materials Science*, vol. 28, no. 13, pp. 3571–3580, 1993.

[105] R. S. Seth, "Measurement of inplane fracture-toughness of paper," *Tappi Journal*, vol. 78, no. 10, pp. 177–183, 1995.

[106] A. Tanaka and T. Yamauchi, "Deformation and fracture of paper during the in-plane fracture toughness testing - examination of the essential work of fracture method," *Journal of Materials Science*, vol. 35, no. 7, pp. 1827–1833, 2000.

[107] P. Makela, "Engineering fracture mechanics analysis of paper materials," *Nordic Pulp and Paper Research Journal*, vol. 27, no. 2, pp. 361–369, 2012.

[108] J. Zechner, M. Janko, and O. Kolednik, "Determining the fracture resistance of thin sheet fiber composites - paper as a model material," *Composites Science and Technology*, vol. 74, pp. 43–51, 2013.

[109] T. Yamauchi and H. Hirano, "Examination of the onset of stable crack growth under fracture toughness testing of paper," *Journal of Wood Science*, vol. 46, no. 1, pp. 79–84, 2000.

[110] D. M. S. Wanigaratne, W. J. Batchelor, A. B. Conn, and I. H. Parker, "Image analysis of plastic deformation in the fracture of paper," *Appita Journal*, vol. 53, no. 6, pp. 471–475, 2000.

[111] D. W. Coffin, "A fracture-based description for the development of tensile and tear strength in paper," *J-for-Journal of Science and Technology for Forest Products and Processes*, vol. 6, no. 6, pp. 29–38, 2018.

[112] W. R. Lanning, C. E. Johnson, S. S. Javaid, and C. L. Muhlstein, "Mode i steady-state crack propagation through a fully-yielded ligament in thin ductile metal foils," *Theoretical and Applied Fracture Mechanics*, vol. 101, pp. 141–151, 2019.

[113] S. S. Javaid, W. R. Lanning, and C. Muhlstein, "The development of zones of active plasticity (zaps) during mode i steady-state crack growth in thin, ductile aluminum sheets," *Experimental Mechanics*, in press, 2019.

[114] J. Hutchinson, "On steady quasi-static crack growth," Harvard Univeristy, Tech. Rep. AFOSR-TR-74-1042, 1974.

[115] J. C. Amazigo and J. W. Hutchinson, "Crack-tip fields in steady crack-growth with linear strain-hardening," *Journal of the Mechanics and Physics of Solids*, vol. 25, no. 2, pp. 81–97, 1977.

[116] P. Castaneda, "Plastic stress intensity factors in steady crack growth," Harvard University, Tech. Rep. AD-A172 146, 1986.

[117] P. P. Castaneda, "Plastic stress intensity factors in steady crack-growth," *Journal of Applied Mechanics-Transactions of the Asme*, vol. 54, no. 2, pp. 379–387, 1987.

VITA

Yoon Joo Na was born and raised in Seoul, South Korea. Yoon Joo came to the United States in 2004 to study abroad and attended secondary schools in Ohio. She graduated *cum laude* from Northwestern University in December 2012 with B.S. in Materials Science and Engineering. Yoon Joo joined the PhD program at Georgia Institute of Technology in 2014 and researched on the mechanical properties of nonwoven fiber network materials. She received her doctoral degree in Materials Science and Engineering in 2019.